

博士學位論文

Development of Base Catalytic Reactions Driven by
Mixed Metal Oxide Clusters

複合金属酸化物クラスターによる
塩基触媒反応系の開発 (英文)

指導教員 山添 誠司 教授

令和5年8月22日提出

東京都立大学大学院

理学研究科 無機化学専攻

学修番号 20945454

氏名 ジュタテミ ヴォラキト

Doctoral Dissertation

Development of Base Catalytic Reactions Driven by
Mixed Metal Oxide Clusters

複合金属酸化物クラスターによる
塩基触媒反応系の開発 (英文)

Supervisor: Prof. Seiji Yamazoe

Date of submission: August 22, 2023

Graduate School of Science, Tokyo Metropolitan University
Inorganic Chemistry Laboratory, Department of Chemistry

Student ID: 20945454

Student name: Vorakit Chudatemiya

Table of Contents

Chapter 1. General introduction	1
1.1. Base catalysis.....	1
1.2 Solid base catalysts.....	1
1.3 Metal oxide clusters.....	2
1.4 Composite material applications	9
1.5 Catalytic applications	12
1.5.1 Knoevenagel and aldol condensation reactions.....	12
1.5.2 CO ₂ fixation reaction.....	13
1.5.3 <i>N</i> -formylation of amine	14
1.6 Purpose of this dissertation.....	16
1.7 References	17
Chapter 2. Superbase catalysis of metal oxide clusters.....	19
2.1. Introduction	19
2.2 Experimental.....	24
2.2.1 Synthesis of NaNbO ₃	24
2.2.2 Synthesis of Na ₃ NbO ₄	24
2.2.3 Synthesis of Nb ₂ O ₅ · <i>n</i> H ₂ O	25
2.2.4 Synthesis of TBA ₆ H ₂ [Nb ₆ O ₁₉] (TBA-Nb ₆)	25
2.2.5 General procedure for Knoevenagel condensation.....	25
2.2.6 General procedure for aldol condensation.....	26
2.2.7 Calculation of product yield	26
2.2.8 Illustration of catalysts	27
2.3 Results and discussion.....	28
2.3.1 Synthesis of NaNbO ₃	28
2.3.2 Synthesis of Na ₃ NbO ₄	28
2.3.3 Synthesis of TBA ₆ H ₂ [Nb ₆ O ₁₉] (TBA-Nb ₆)	29
2.4 Conclusions	37
2.5 References	38
2.6 Appendix.....	39
Chapter 3. Lewis basicity of metal oxide clusters.....	40
3.1. Introduction	40

3.2 Experimental.....	44
3.2.1 Synthesis of $\text{NaTa}_{x/6}\text{Nb}_{(6-x)/6}\text{O}_3$	44
3.2.2 Synthesis of $\text{Na}_3\text{Ta}_{x/6}\text{Nb}_{(6-x)/6}\text{O}_4$	44
3.2.3 Synthesis of $(\text{Ta}_x\text{Nb}_{6-x})_2\text{O}_5 \cdot n\text{H}_2\text{O}$	44
3.2.4 Synthesis of $\text{TBA}_6\text{H}_2[\text{Ta}_x\text{Nb}_{6-x}\text{O}_{19}]$ (TBA- $\text{Ta}_x\text{Nb}_{6-x}$).....	45
3.2.2 General procedure for CO_2 fixation reaction.....	45
3.2.3 Calculation of product yield.....	45
3.2.4 Illustration of catalysts.....	46
3.3 Results and discussion.....	47
3.3.1 Synthesis of $\text{NaTa}_{x/6}\text{Nb}_{(6-x)/6}\text{O}_3$	47
3.3.2 Synthesis of $\text{Na}_3\text{Ta}_{x/6}\text{Nb}_{(6-x)/6}\text{O}_4$	47
3.3.3 Synthesis of $\text{TBA}_6\text{H}_2[\text{Ta}_x\text{Nb}_{6-x}\text{O}_{19}]$ (TBA- $\text{Ta}_x\text{Nb}_{6-x}$).....	48
3.4 Conclusions.....	63
3.5 References.....	64
3.6 Appendix.....	65
Chapter 4. Bifunctional catalysis of composite clusters.....	67
4.1. Introduction.....	67
4.2 Experimental.....	71
4.2.1 Synthesis of $[\text{Pt}(\text{Nb}_6\text{O}_{19})_2]^{12-}$ ($\text{Pt}(\text{Nb}_6)_2$).....	71
4.2.2 General procedure for <i>N</i> -formylation reaction.....	71
4.2.3 Procedure for time course reaction.....	71
4.2.4 Procedure for reusability test.....	72
4.2.5 Calculation of product yield.....	72
4.2.6 Illustration of catalysts.....	72
4.3 Results and discussion.....	73
4.3.1 Synthesis of $[\text{Pt}(\text{Nb}_6\text{O}_{19})_2]^{12-}$ ($\text{Pt}(\text{Nb}_6)_2$).....	73
4.4 Conclusions.....	91
4.5 References.....	92
4.6 Appendix.....	93
Chapter 5: Concluding remarks.....	98
References.....	102
Chapter 6: Future prospects.....	103

References	107
List of achievements	108
Publications	108
Conference presentations.....	108
Acknowledgment	110

Chapter 1. General introduction

1.1. Base catalysis

Catalysis technology has been greatly developed over the years in order to improve efficiency and effectiveness to reaction performance. Base catalysts have been employed to promote numerous organic reactions such as transesterification, Michael addition, and isomerization of unsaturated carbons.¹ Basicity could be classified into Brønsted basicity and Lewis basicity based on the mechanism where the reaction is driven, which are proton abstraction and electron donation, respectively. One of the useful and common reactions to evaluate Brønsted basicity of a catalyst is Knoevenagel condensation. The condensation occurs after proton abstraction from substrate and form C–C bond with subsequent condensation to provide product. In the case of Lewis basicity, electronic donation is the key factor, CO₂ fixation reaction is one of the examples, where activation of CO₂ would result in nucleophilic species and react with substrate to form a corresponding carbonylated product.

1.2 Solid base catalysts

Among base catalysts, solid base catalysts such as MgO and CaO are one of the well-known solid base catalysts. These materials contain porous surface, which contain high specific surface area, acting as active sites. However, the surface could easily be deactivated by the presence of water, CO₂, and dissolution in a polar solvent.^{2,3} For instance, CO₂ adsorbed on the surface of MgO would form MgCO₃ as illustrated in Figure 1-1 or hydroxide species as a result of water adsorption. Therefore, it is necessary to activate solid base catalysts at high temperature under vacuum to remove adsorbed substrates prior to each use. The modification by coating the CaO with Al₂O₃ was reportedly improved stability and water tolerance comparing to bare CaO.³ Despite activation processes, solid base catalysts have been employed to promote various organic reactions, such as isomerization of alkenes, aldol condensation reaction, Michael addition and esterification.⁴

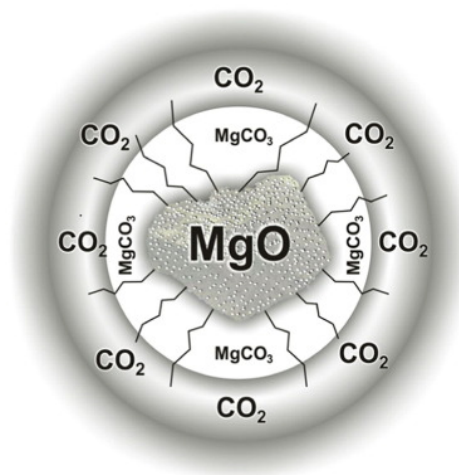


Figure 1-1. Illustration of MgO and MgCO₃ formed as a result of CO₂ adsorption on the surface.⁵

Moreover, other types of solid base catalysts have also been reported including hydrotalcite, zeolites, metal phosphates, metal oxynitrides, and anion exchange resins. Hydrotalcite or often referred as layered double hydroxide (LDH), with general formula of Mg₆Al₂(OH)₁₆CO₃·4H₂O, could be modified by replacing Mg with Zn, Fe, Co, Ni, or Cu and Al can be replaced by Cr, Fe, or In. Generally, the as-synthesized LDH was reported to not be catalytically active because of the existence of pores and interlayer water. After treatment at high temperature (>423 K) under inert atmosphere, the activities were significantly improved.⁶ Zeolites modified with excess alkali cations, such as Cs⁺ and Rb⁺ provided high basicity and promoted side-chain alkylation of toluene with methanol to produce styrene or with formaldehyde to yield ethylbenzene.^{7,8}

1.3 Metal oxide clusters

One of the ubiquitous subsets of metal oxide clusters (MOCs) is polyoxometalate (POM) clusters, which contain metals of groups 5 and 6 (V, Nb, Ta, W, and Mo). POM composed of MO₆ units sharing corner and edge O atoms that result in several geometries depending on their compositions and types of metals. POMs with single type of metals are classified as isopolyoxometalates (isoPOM), whereas POMs which contain multiple types of metals are called heteropolyoxometalates (heteroPOM) (Figure 1-2). IsoPOMs are formed based on Lindqvist-type structure and heteroPOMs have the general formula of X_aM_n, where Keggin (XM₁₂) and Wells-Dawson (X₂M₁₈) types could form lacunary structures where they become unsaturated by losing metal atoms.⁹

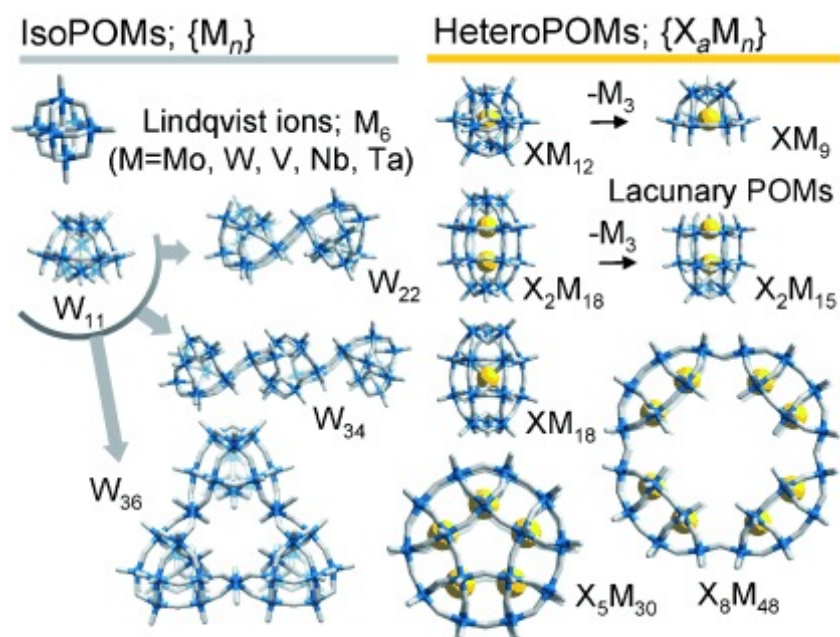


Figure 1-2. General structures of various isoPOMs based on Lindqvist-type structure and heteroPOMs based on lacunary POMs reported.¹⁰

Structural diversity of POMs or MOCs comes from factors taken place during the synthesis, which usually starting with mononuclear complex of $[MO_x]_n$ as building block or bulk metal oxide reacting in acidic or basic condition at high temperature. Various factors including concentration and type of metal oxide and heteroatom, types of cations, pH of the solution, ionic strength, presence ligands, reducing agent, and temperature of reaction and processing techniques affect the product formation.^{10,11}

One of the important factors that affect the formation of the clusters by stabilizing the structure as well as determining the solubility of the MOCs is counter cation. Several works including $Bi_6[FeO_4Fe_{12}O_{12}(OH)_{12}(O_2CCCl_3)_{12}]^+$ ($\{Bi_6Fe_{13}\}$),¹² $H_3[\{Bi(DMSO)_3\}_4V_{13}O_{40}]$ ($\{Bi_4V_{13}\}$),¹³ $[(Ce(DMSO)_3)_2V^{IV}V^V_{11}O_{33}Cl]^{2-}$ ($\{Ce_2V_{12}\}$),^{14,15} and $[La(H_2O)_4]PMo^V_8Mo^{VI}_4O_{36}(OH)_4]^{5+}$ ($\{La_4Mo_{12}\}$),¹⁶ which showed the importance of cation in addition to ligand to stabilizing the structure (Figure 1-3).

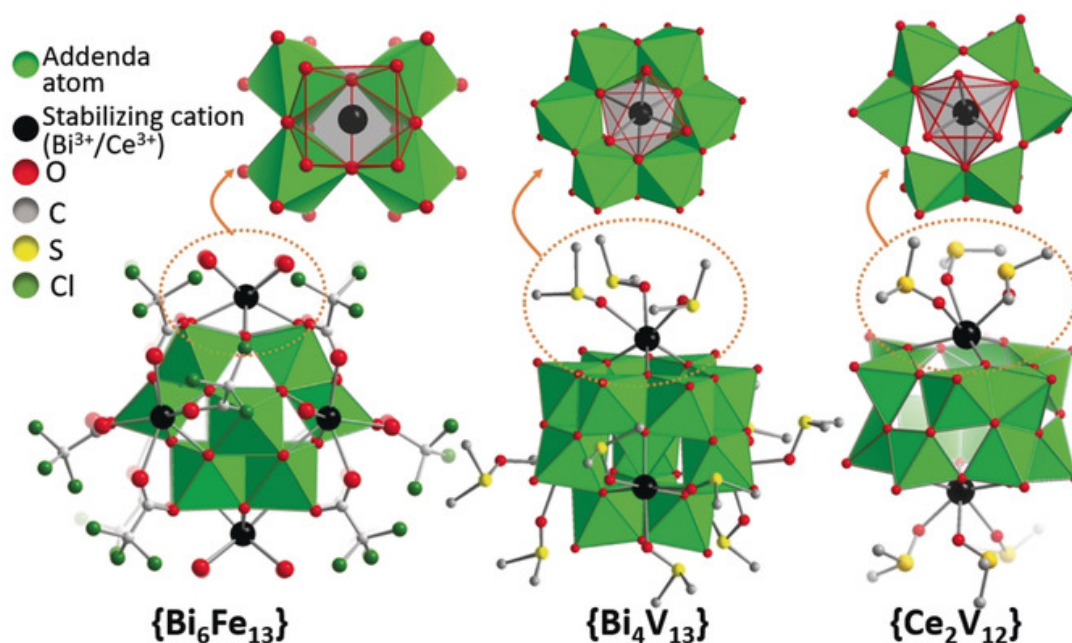


Figure 1-3. MOCs and the role of cations required for stabilization.

The solubility of MOCs is unique and opposite of the normal solubility trend as depicted in Figure 1-4.¹⁷ The normal trend of solubility corresponded to Cs^+ providing the lowest solubility while Li^+ would provide the highest solubility. In the case of MOCs, the opposite trend was observed.

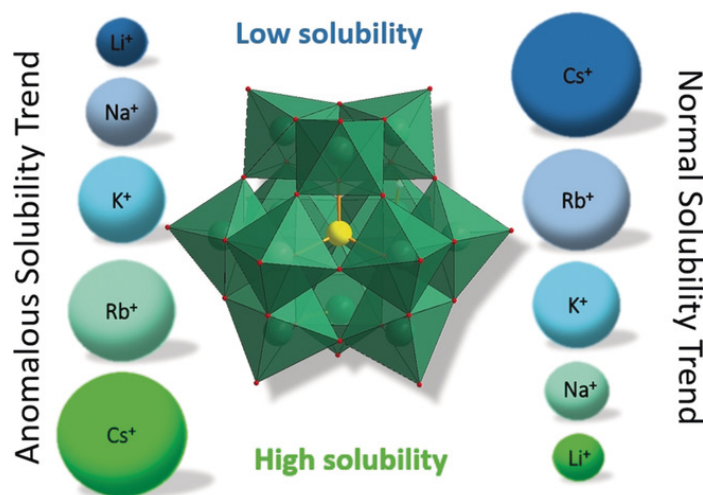


Figure 1-4. The unique solubility of cation when incorporated with MOCs.¹⁷

Another factor that influence the formation of structures is pH value of the solution. Generally, MOCs were known as materials with high acidity and the study of polyoxovanadates, polyoxotungstates, and polyoxomolybdates have been widely explored. For isopolyoxovanadates, one of the stable clusters, $[\text{V}_{10}\text{O}_{28}]^{6-}$, which is most stable in acidic condition, could maintain its structure in an aqueous solution at neutral pH for days. However, when dissolved in basic solution, the $[\text{V}_{10}\text{O}_{28}]^{6-}$ structure would turn into smaller

isopolyoxovanadates.¹⁸ The stability of each isopolyoxovanadate in aqueous media is summarized in Figure 1-5.

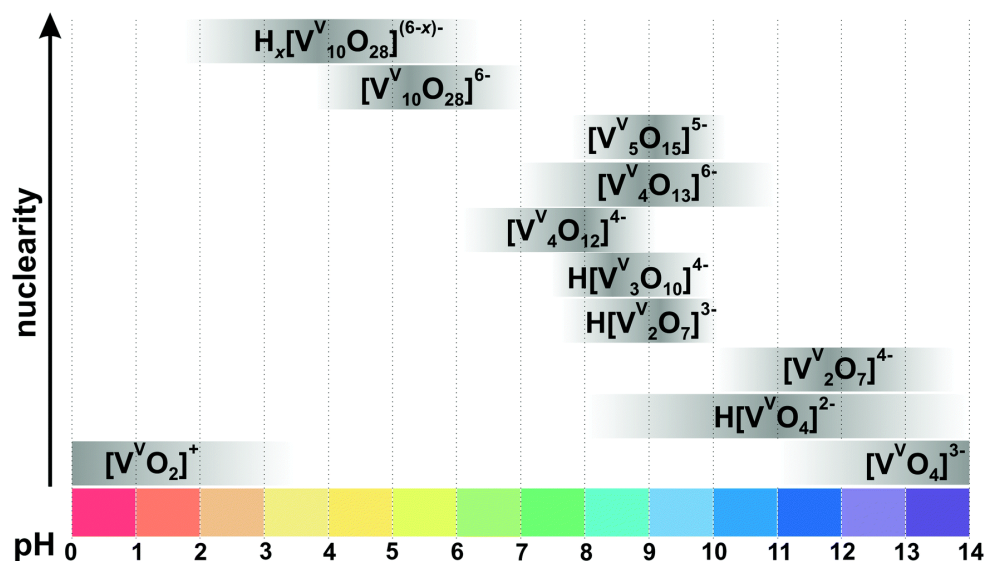


Figure 1-5. Speciation of polyoxovanadates in aqueous media at various pH range.¹¹

In the case of polyoxomolybdates, the monomeric $[\text{Mo}^{\text{VI}}\text{O}_4]^{2-}$ was found to be stable in the neutral to basic condition, while in an acidic condition, structures with higher nucleicity could be observed, including $[\text{Mo}^{\text{VI}}_7\text{O}_{24}]^{6-}$, isomers of $[\text{Mo}^{\text{VI}}_8\text{O}_{26}]^{4-}$, $[\text{H}_3\text{Mo}^{\text{VI}}_8\text{O}_{28}]^{5-}$, and $[\text{Mo}^{\text{VI}}_{36}\text{O}_{112}(\text{OH}_2)_{16}]^{8-}$ as illustrated in Figure 1-6.^{11,18-23} The stability of polyoxomolybdates at low pH suggested their high acidity and application as acid catalyst.²⁴

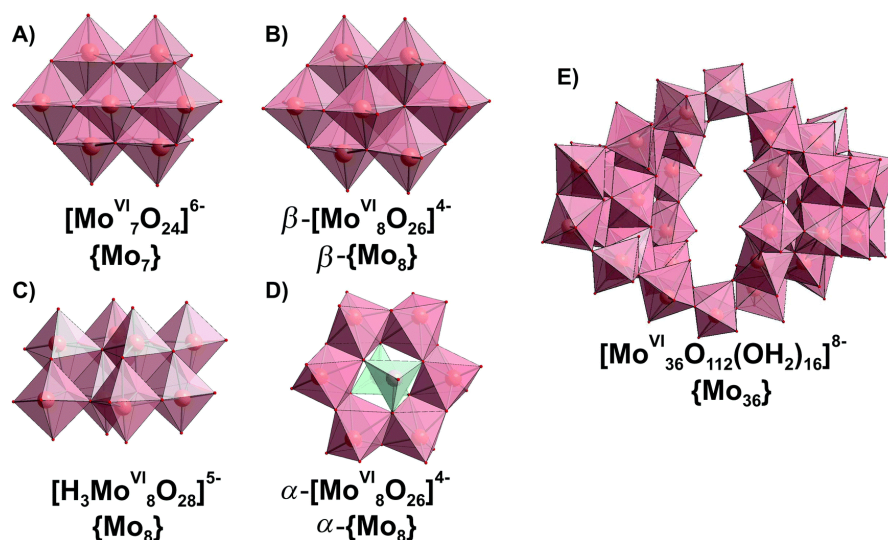


Figure 1-6. Various structures of polyoxomolybdates which are stable in acidic aqueous condition.¹¹

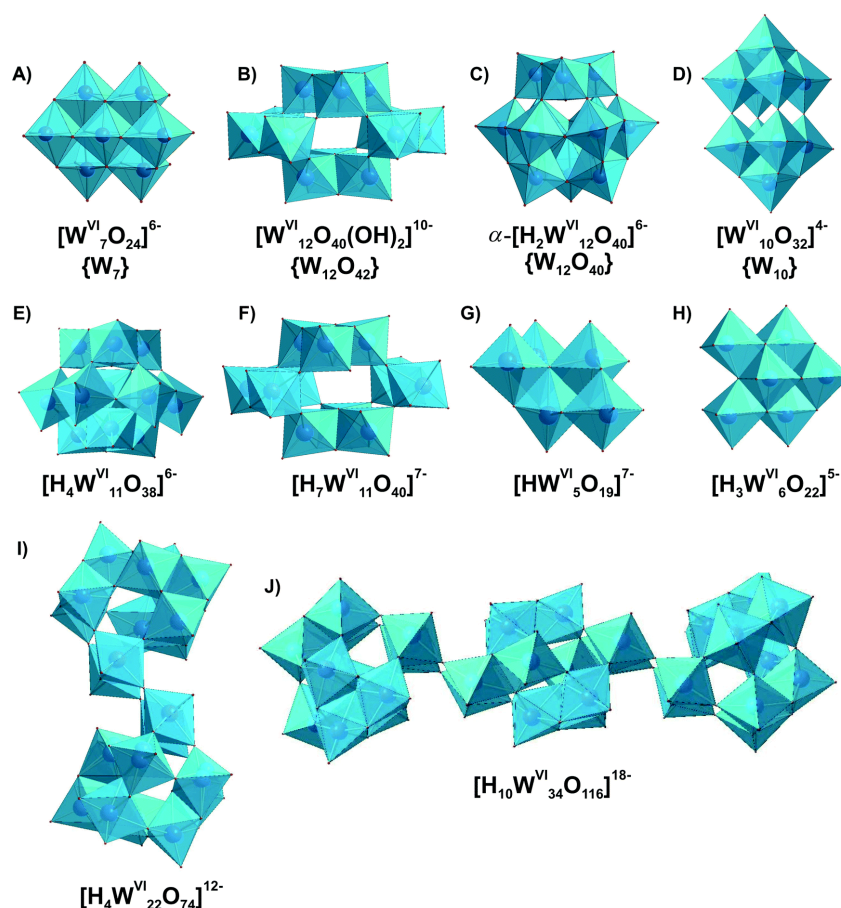


Figure 1-7. Reported structures of isopolyoxotungstates stable in aqueous media or isolated as solid.¹¹

Various structures of isopolyoxotungstates have been reported (Figure 1-7).^{11,25–32} Additionally, relatively high stability of lacunary structures could be formed which allowed incorporation of other metal ions to the structure, for instance, $[KFe_{12}(OH)_{18}(\alpha-P_2W_{15}O_{56})_4]^{29-}$, where $[Fe_{12}]$ core linked four Wells-Dawson units of $[P_2W_{15}]$ (Figure 1-8) that could form by self-assembly with high stability.^{10,33} In addition to the new structure obtained, the cluster also exhibited strong antiferromagnetic property as a result of incorporation of Fe(III) centers.³³

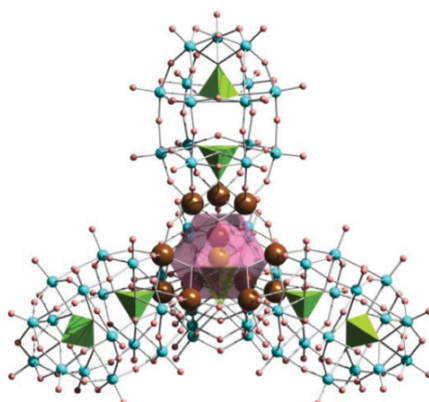


Figure 1-8. Crystallographic structure of $[KFe_{12}(OH)_{18}(\alpha-P_2W_{15}O_{56})_4]^{29-}$ reported by C. P. Pradeep, *et al.*³³ Color scheme: O = pink, W = cyan, Fe = brown, PO_4 = green polyhedra, K = orange, KO_{12} = purple polyhedra.

Numerous types of polyoxotungstates and polyoxomolybdates have been reported, unlike the progress on polyoxoniobates and polyoxotantalates, due to the low solubility and reactivity during the synthesis.⁹ Figure 1-9 summarized the species of polyoxoniobates and polyoxotantalates in basic aqueous solution.^{9,34-39} In addition, $[\text{Ta}_{10}\text{O}_{28}]^{6-}$ was also reported to be obtained by prolonged heating of $[\text{Ta}_6\text{O}_{19}]^{8-}$ in toluene.⁴⁰

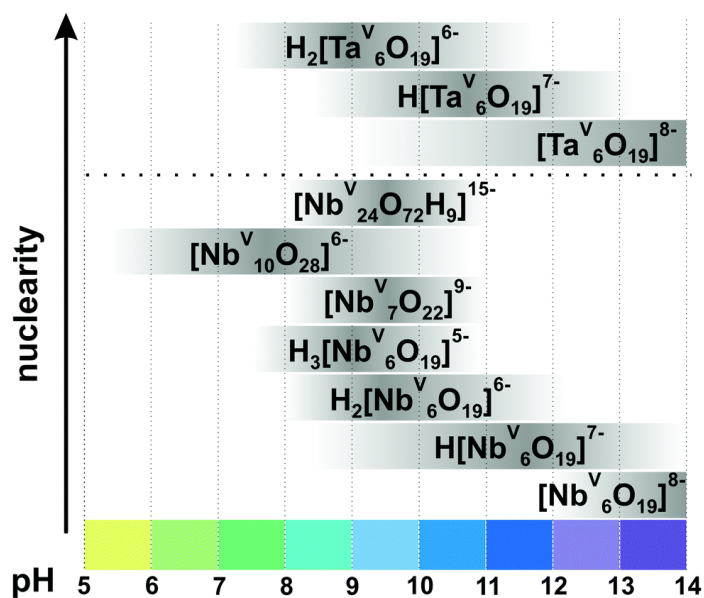


Figure 1-9. Polyoxotantalates and polyoxoniobates exhibited in aqueous solutions stabilized under different pH.¹¹

Furthermore, incorporation of metal ions was also taken place for polyoxotantalates to functionalize or stabilize the clusters. The criteria for doping transition metal into POMs or MOCs would be the compatibility of the transition metal with the MOCs, for example pH value that MOCs with group 5 metals tend to possess high pH and are stable in alkaline media. The dopant has to be either rare alkaline-soluble (amphoteric metal), such as Ti^{4+} , or a complex with a protective ligand, such as Cu(II) amine complexes.⁹ A series of Ti-incorporated MOCs have been reported including $[\text{Ti}_2\text{Nb}_8\text{O}_{28}]^{8-}$, $[\text{TiNb}_9\text{O}_{28}]^{7-}$, $[\text{Ti}_{12}\text{Nb}_6\text{O}_{44}]^{10-}$, $[\text{Ti}_2\text{Ta}_8\text{O}_{28}]^{8-}$, and $[\text{Ti}_{12}\text{Ta}_6\text{O}_{44}]^{10-}$, which were stabilized by their molecular charge (Figure 1-10).⁴¹

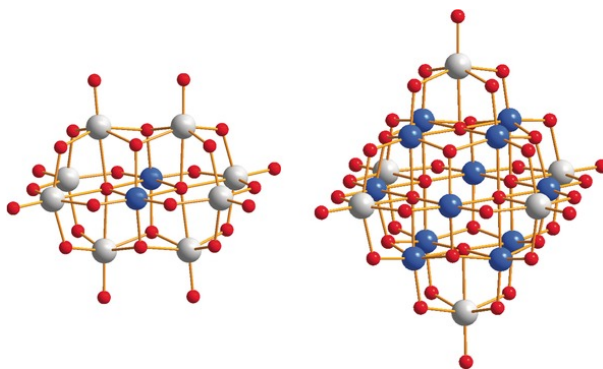


Figure 1-10. Illustration of $[\text{Ti}_2\text{Ta}_8\text{O}_{28}]^{8-}$, and $[\text{Ti}_{12}\text{Ta}_6\text{O}_{44}]^{10-}$.⁴¹

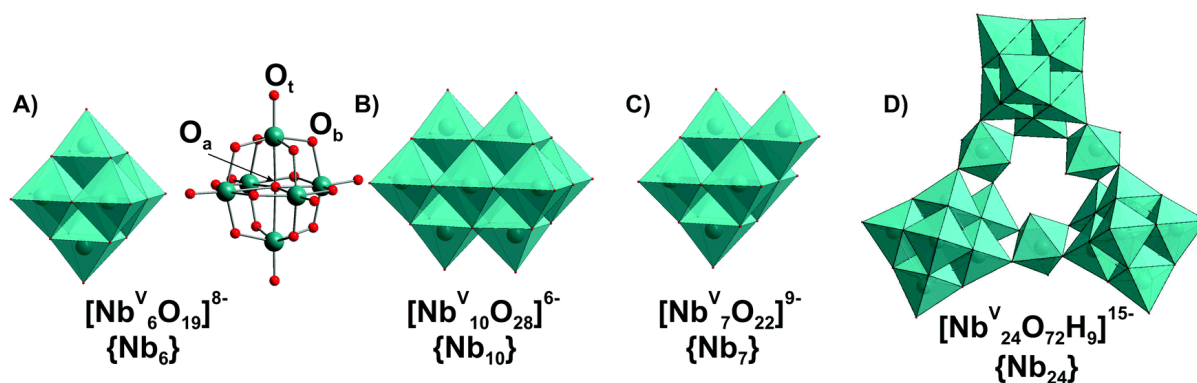


Figure 1-9. Reported polyoxoniobates based on the Lindqvist geometry.¹¹

The four main types of polyoxoniobates were reported as stable species in aqueous media (Figure 1-9). The basicity of polyoxoniobates is greatly different from its bulk phase which acts as an acid catalyst, along with several MOCs discovered, such as, Keggin-type $[\text{PW}_{12}\text{O}_{40}]^{3-}$ that is known as acid catalyst having $\text{p}K_{\text{a}}$ value of -13 ,⁴² while the Vanadium-doped polyoxomolybdate with the same structure, $[\text{PMo}_{10}\text{V}_2\text{O}_{40}]^{5-}$,⁴³ exhibited less acidity with $\text{p}K_{\text{a}}$ value of 0 (Figure 1-10). Since Sugahara *et al.* discovered the high basicity of $[\gamma\text{-HGeW}_{10}\text{O}_{36}]^{7-}$ through Knoevenagel condensation of benzaldehyde with phenylacetonitrile ($\text{p}K_{\text{a}} = 21.9$),⁴⁴ the study of basicity in MOCs has gained tremendous attention, especially Lindqvist-type MOCs (M_6O_{19}) with group 5 metals which are emerging materials to study and utilize as base catalysts due to high $\text{p}K_{\text{a}}$ values (Figure 1-10).

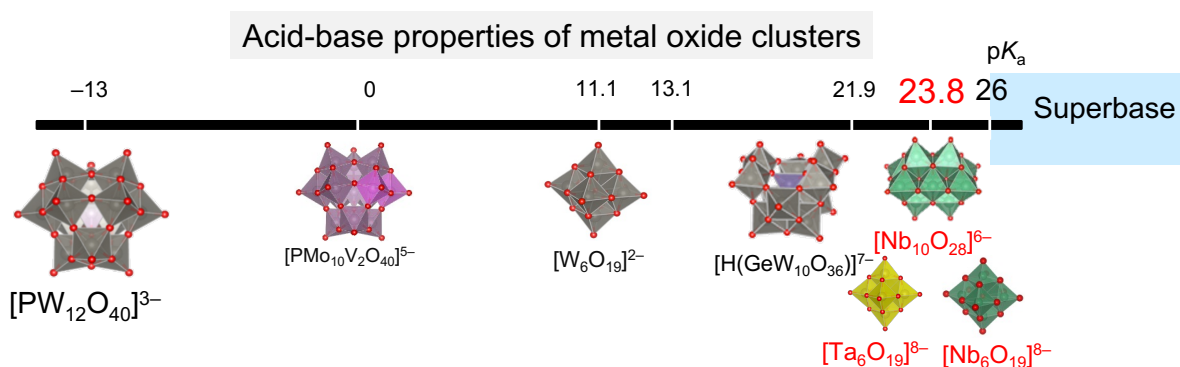


Figure 1-10. Acid-base properties of metal oxide clusters on a scale of $\text{p}K_{\text{a}}$.

The basicity of the MOCs are related to natural bonding orbital (NBO) charges of O atoms calculated by density functional theory (DFT). The higher negative charge correlates to higher base strength of the cluster. Among the Lindqvist-type MOCs, the base strength according to NBO charge are in the order of $[\text{Ta}_6\text{O}_{19}]^{8-} > [\text{Nb}_6\text{O}_{19}]^{8-} > [\text{W}_6\text{O}_{19}]^{2-} > [\text{Mo}_6\text{O}_{19}]^{2-}$ (Figure 1-11).⁴⁵ Moreover, different site of O exhibited various basicity, in which depending on metals. In the case of group 5 metals, terminal O coordinated to Ta or Nb showed higher basicity than bridging O atoms, while bridging O atoms of MOCs with group 6 metals have

higher base strength than terminal O atoms. Knoevenagel condensation reactions were carried out to evaluate Brønsted basicity through the ability to abstract proton from nitrile. Lewis basicity of the MOCs have also been elucidated by conducting CO₂ fixation to epoxide to form carbonate derivative. Due to high basicity of MOCs with group 5 metals and their potential to be considered as superbases catalyst inspired further investigation on the development of MOCs and exploration of their catalytic applications.

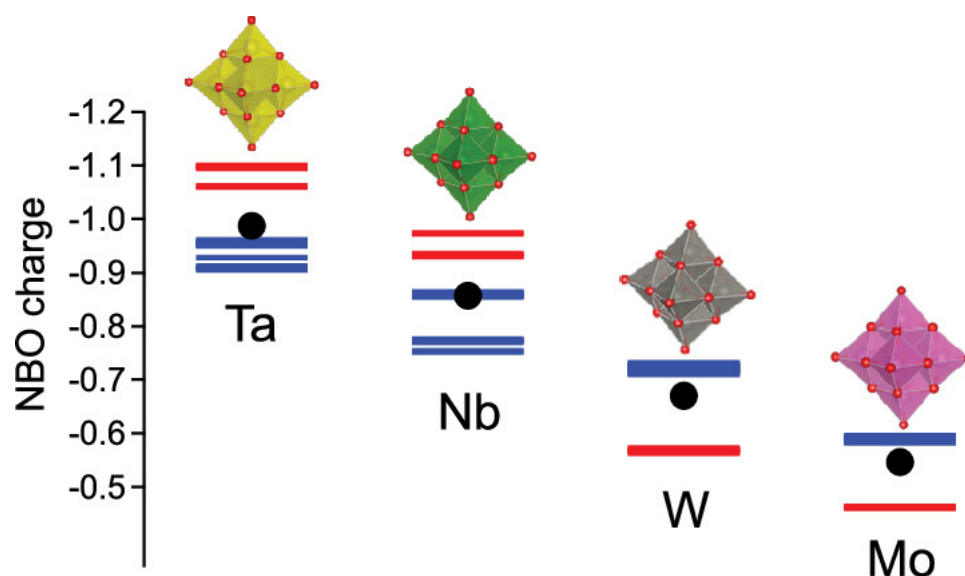


Figure 1-11. NBO charge of each type of hexametalates.⁴⁵

1.4 Composite material applications

In addition to doping metal ions to the existing MOCs to obtain new type of clusters, utilization of MOCs as composite materials have also been researched with a goal to enhance functionality or even achieve dual functionalities of the resultant materials. Our group has reported the formation of [Nb₆O₁₉]⁸⁻-modified Au nanoparticles supported on Al₂O₃ that formed by adsorption on surface through electron donation of MOCs to the nanoparticles (Figure 1-12). The resultant composite catalyst exhibited bifunctional catalysis as a result of combination of base catalysis provided by [Nb₆O₁₉]⁸⁻ and reduction ability of Au nanoparticles. The resultant composite catalyst showed a significant improvement in the catalytic reduction of *p*-nitrophenol to *p*-aminophenol using H₂ as a reductant because the heterolytically cleaved H₂ would react with nitrophenolate ions generated by base catalysis of [Nb₆O₁₉]⁸⁻.⁴⁶ The interface of this composite catalyst served as a bifunctional active site.

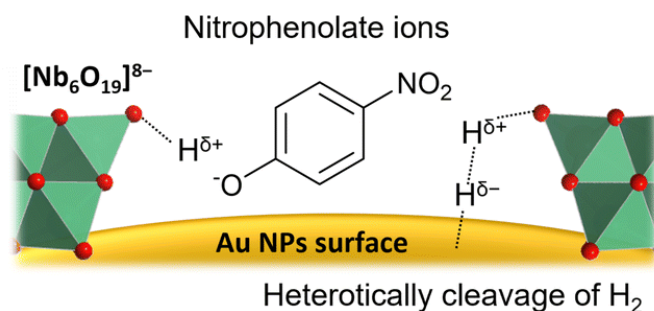


Figure 1-12. Proposed mechanism of $[\text{Nb}_6\text{O}_{19}]^{8-}$ -modified Au/ Al_2O_3 for reduction of *p*-nitrophenol.⁴⁶

Moreover, due to the multiple redox states and ability to delocalize electrons while maintaining the structure of MOCs, they have been researched as materials for memory devices. For instance, Si/30 nm SiO_2 /MOC/Pt have been applied as flash memory, Si/3.1 nm SiO_2 /MOC/25 nm Ta_2O_5 /Al for capacitive memory, and indium tin oxide/MOC/Pt for resistive memory.⁴⁷⁻⁴⁹ $[\text{PW}_{12}\text{O}_{40}]^{3-}$ (PW_{12}) has been developed as hybrid metal-insulator/MOC-semiconductor capacitors.^{47,48} The incorporation of MOCs reduced the electron-hole pair generation that usually inhibited high speed of electron transfer. Therefore, MOCs introduction improved the speed of the switching and writing processes, which is beneficial for the development and application of memory device.⁴⁹ When applying PW_{12} into the nonvolatile capacitive memory cells, PW_{12} served as a charge storage medium that resulted in a larger memory window.⁴⁹

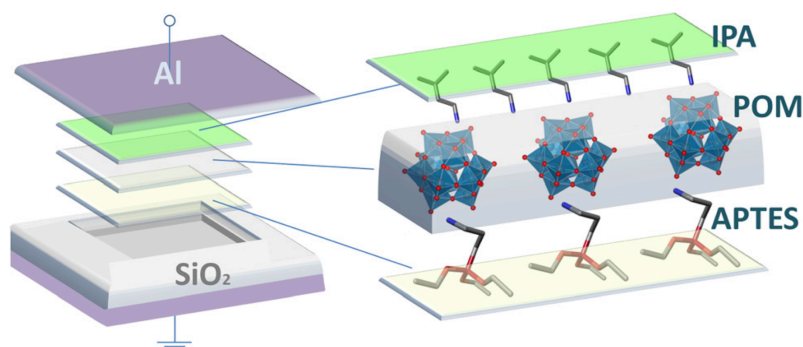
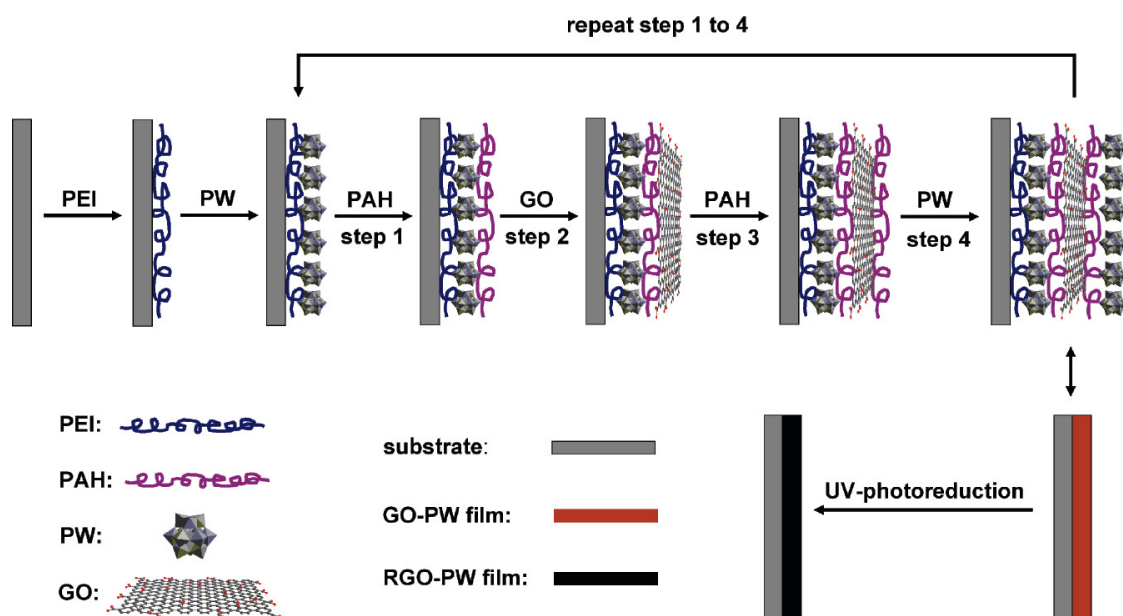


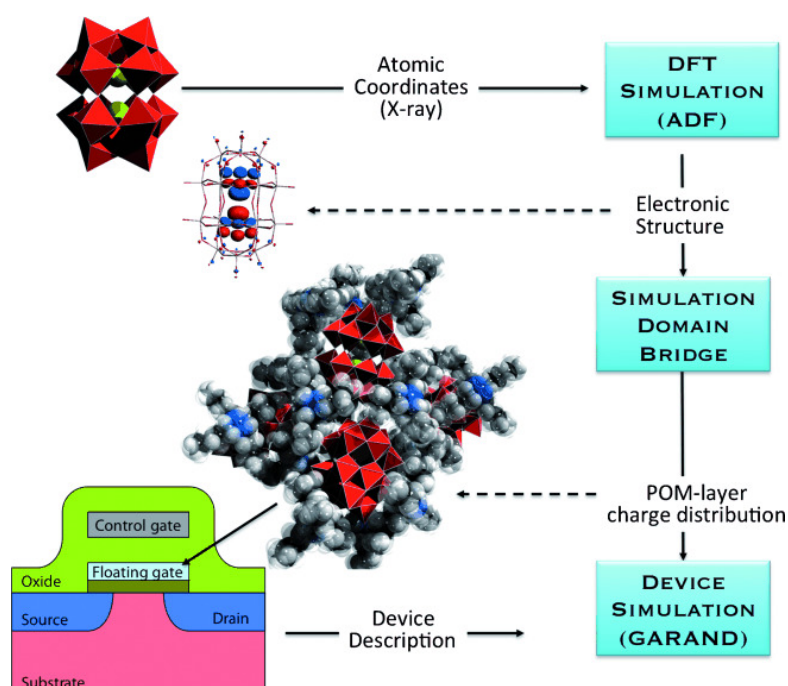
Figure 1-13. The illustration of metal-insulator/MOC molecules-semiconductor capacitors.

In a fabrication of composite film using graphene oxide as a precursor, reduction of graphene oxide is required to establish high conductivity. Recently, photoreduction has gained attention as an alternative method instead of using chemical or thermal treatment. By incorporating PW_{12} to reduced graphene oxide composite film, PW_{12} acted as a photocatalyst aiding the reduction of graphene oxide upon UV irradiation. A fabrication of the composite film through a layer-by-layer assembly resulted in precisely controlled thickness of the film with high uniformity where the process is illustrated in Scheme 1-1.⁵⁰



Scheme 1-1. The illustration of layer-by-layer assembly of reduced graphene oxide-PW₁₂ multilayer films.

The concept of incorporation of MOC as a component in non-volatile molecular memory has been proposed (Scheme 1-2).⁵¹ This concept was driven by the higher electronic complementarity of MOC with SiO₂ in addition to high redox potentials and multiple redox states of MOC. Wells-Dawson-type clusters, [X₂M₁₈O₅₄]⁴⁻, were chosen because of the wide availability and of data on their electronic structure and reduction potentials for calculation. The simulation led to a finding that MOCs could be viable for material as a floating gate, where its main function is to hold electrical charge.



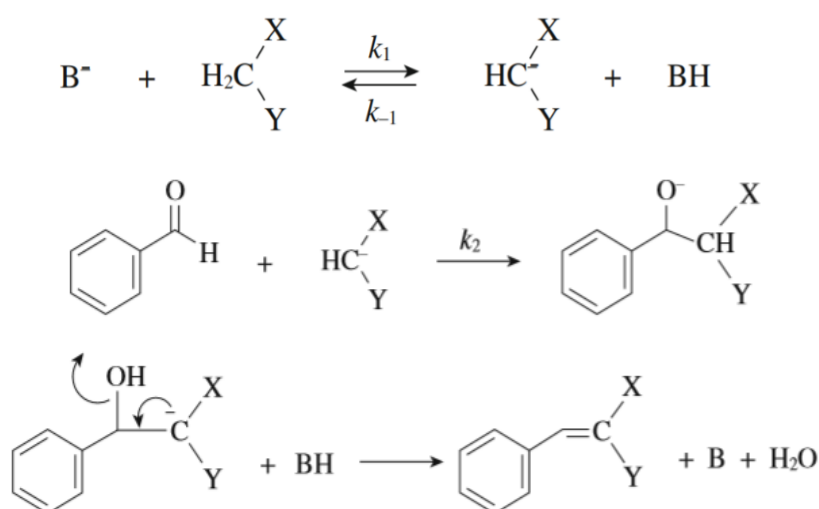
Scheme 1-2. Block diagram of the simulation methodology incorporating Wells-Dawson clusters as floating gate in non-volatile molecular memory material.⁵¹

These researches suggest high potential of application of MOCs by integrating with other metal oxides or other support materials to improve functionality. However, little is known about basicity of MOCs as well as their catalytic application, in which some of the base catalytic reactions would be introduced in the next section.

1.5 Catalytic applications

1.5.1 Knoevenagel and aldol condensation reactions

Knoevenagel condensation is one of the well-known reactions to evaluate the basicity of catalysts. The reaction is driven by proton abstraction of methylene compounds that would result in active species to react with carbonyl compounds. Consequently, this reaction provides a carbon-carbon bond formation as a condensate product and water as byproduct. General reaction mechanism is represented in Scheme 1-3.⁴

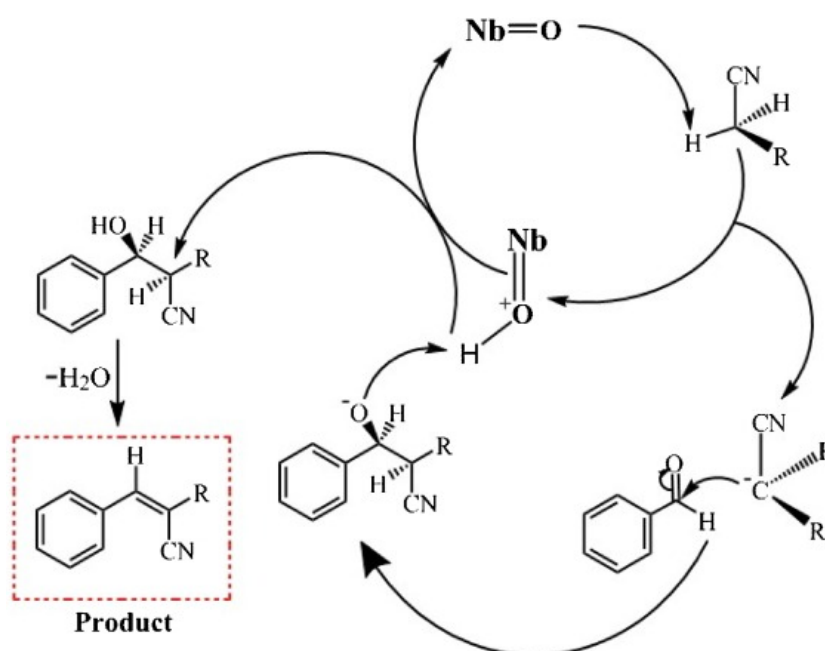


Scheme 1-3. Reaction mechanism of Knoevenagel condensation on basic sites.⁴

The rate law is considered as $r = k_1[\text{CH}_2\text{XY}]$, which depends on the proton abstraction by base from methylene group as the rate-determining step. The proton abstraction is therefore depending on $\text{p}K_a$ value of the substrate. Base strength ($\text{p}K_a$) of the catalyst has to be higher than $\text{p}K_a$ of the substrate in order to drive the reaction.

A detailed mechanism of Knoevenagel condensation using $\text{K}_7\text{Nb}_6\text{O}_{19} \cdot 13\text{H}_2\text{O}$ as a catalyst using malononitrile and ethyl cyanoacetate as substrates was proposed (Scheme 1-4).⁵² First, the terminal O atoms of the catalyst with high basicity would abstract proton of the methylene compound to produce carbanion. The carbanion would react at the carbon atom of the aldehyde group to generate C–C bond forming alkoxide ion. The alkoxide ion would

abstract proton of protonated catalyst, resulting in β -hydroxyl compound and regenerated catalyst. After dehydration of β -hydroxyl compound, the product could be obtained.

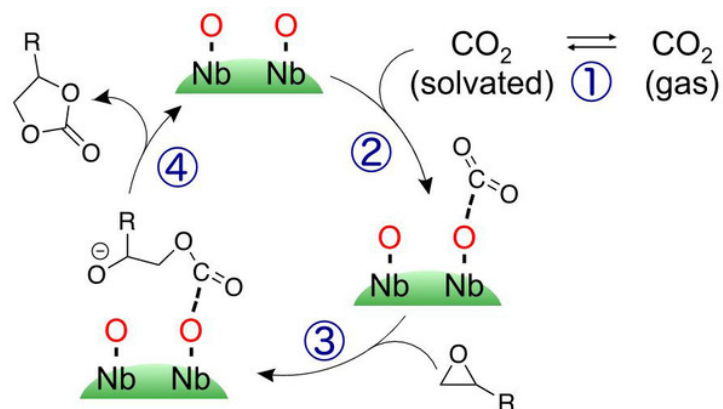


Scheme 1-4. Knoevenagel condensation reaction of aldehydes proposed by Q. Xu, *et al.*⁵²

In this study, the condensation between benzaldehyde and nitriles with known pK_a values were used to estimate the base strength of the MOCs. The active sites suggested by theoretical calculation were terminal O atoms coordinated to Nb or Ta, which exhibited the highest negative charge.

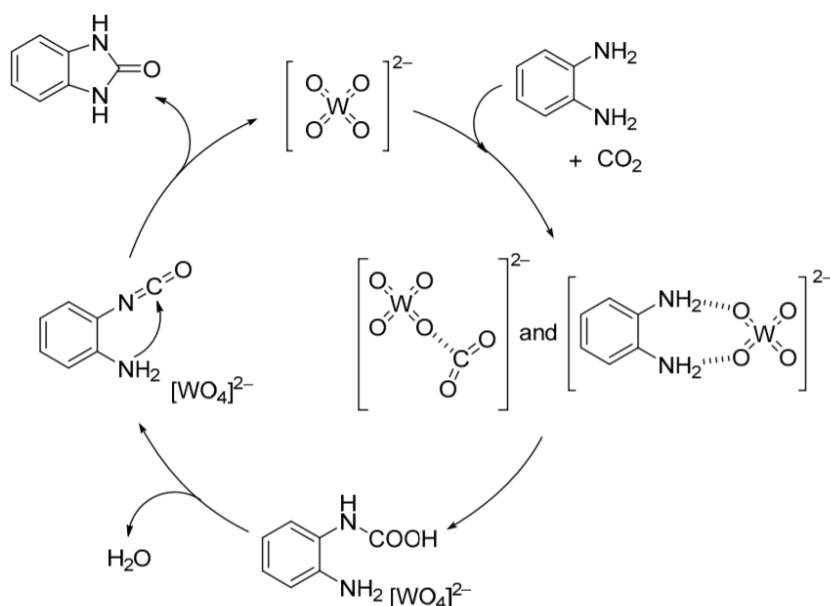
1.5.2 CO₂ fixation reaction

In addition to Brønsted basicity, MOCs exhibited Lewis basicity which can be applied for activation of CO₂ to react with substrate and produce value-added chemicals using CO₂ as a C1 source. The challenge of CO₂ utilization is its high stability, where appropriate catalyst such as base catalyst is required to activate and generate nucleophilic CO₂ after activation. One of the useful reactions would be CO₂ fixation reaction to epoxide to form cyclic carbonates as shown in Scheme 1-5,⁵³ which are utilized as materials for solvents, monomers, electrolytes, and pharmaceuticals.



Scheme 1-5. Proposed CO₂ fixation to epoxide using TBA-Nb₁₀O₂₈ as the catalyst.⁵³

Moreover, CO₂ conversion reaction using diamine as a substrate to form urea as a product was reported. In the proposed mechanism by Sugahara *et al.* using WO₄ as a catalyst, WO₄ formed adduct with both CO₂ and 1,2-phenylenediamine (Scheme 1-6).⁵⁴ Subsequent dehydration and nucleophilic attack of the NH₂ and OH groups occurred to yield the final product.



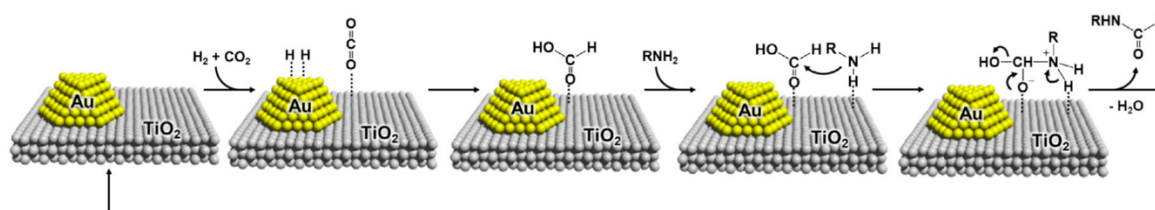
Scheme 1-6. CO₂ fixation promoted by WO₄ as a catalyst.⁵⁴

1.5.3 N-formylation of amine

This reaction requires a combination of carbonyl source and reducing agent to generate formamide from amine. Formamides are used as key intermediates in organic syntheses in pharmaceuticals and fine chemicals. Conventional production of formamides involves CO and phosgene as carbonyl source and reducing agent, respectively. The utilization of CO₂ and H₂ as a carbonyl source and a reducing agent would be a better alternative combination due to less

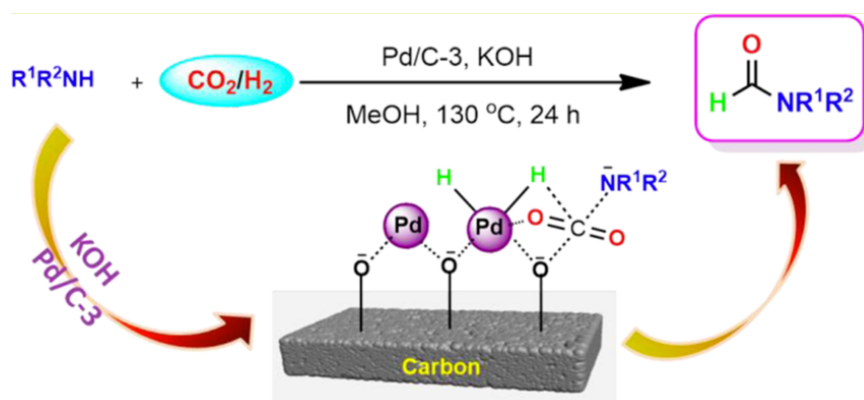
toxicity and higher atom efficiency. The catalysts which have been employed were Au nanoparticles on TiO₂ support and Pd(NH₃)_xCl_y/C.⁵⁵

The proposed reaction mechanism in the first case suggested that the reaction proceeded with formic acid generated in-situ from hydrogenated CO₂ by Au nanoparticles, in which the Lewis acid sites of TiO₂ activated formic acid to form a complex (Scheme 1-7).⁵⁶ Then, the lone pair of amine would react with carbonyl carbon of formic acid by nucleophilic attack. Subsequent dehydration yielded corresponding formamide as the product while maintaining the reducible groups such as olefins, halogens, carbonyls, carbamates, and cyano groups.⁵⁶



Scheme 1-7. The proposed mechanism of *N*-formylation of amine promoted by Au nanoparticles/TiO₂.⁵⁶

In the latter case, Pd(NH₃)_xCl_y/C with the presence of KOH was reported as another catalytic system to promote *N*-formylation of amines to formamides (Scheme 1-8). KOH was used to functionalize the carbon support and to provide basic site for CO₂ adsorption. CO₂ would be activated by the in-situ reduced Pd species, which would then react with amine to generate carbamates and subsequently hydrogenated to produce formylated products.⁵⁵



Scheme 1-8. Illustration of *N*-formylation of amine promoted by Pd(NH₃)_xCl_y/C under CO₂ and H₂ atmosphere.⁵⁵

1.6 Purpose of this dissertation

This dissertation covers development of base catalysts to improve the catalytic activity, selectivity, and applications. Some examples of base catalytic applications focused in this dissertation include Knoevenagel and aldol condensation reaction, CO₂ fixation to styrene oxide, and *N*-formylation of amine.

Knoevenagel condensation and aldol condensation reactions involved the proton abstraction of substrate followed by a subsequent dehydration that resulted in a condensate product. These two reactions could be used to determine the base strength of the catalysts due to the known pK_a value of the substrates. MOCs with different types of metals and structures result in different acid-base properties. Up to now, Lindqvist-type MOCs with group 5 metals have been discovered as base catalyst with pK_a value over 26 that could be considered as superbase catalyst. Another feature of MOCs is water tolerance where the reaction could be proceeded even in the presence of water in the system that is beneficial for condensation reaction because MOCs would not be deactivated as easily as solid base catalysts.

It is well known that CO₂ is one of the greenhouse gases contributed to global warming. As a result, researchers have been experimenting methods to reduce emitted CO₂ in the environment. This includes CO₂ capture and storage (CCS) and CO₂ capture and utilization (CCU). However, the challenge of utilizing CO₂ as a C1 source prevents practical use in current industries. Appropriate base catalysts are required to activate CO₂ to react with substrate, forming value added products efficiently without using harsh conditions. The reactions which conducted in this dissertation included CO₂ fixation to styrene oxide to form styrene carbonate and *N*-formylation of amine in the presence of CO₂ and H₂ to produce formamides. The production of these products using catalysts reported in this dissertation would provide highly selective results under mild conditions. The products of these reactions are intermediates in organic syntheses applicable in production of solvents and pharmaceuticals.

In conclusion, the study covered in this dissertation would contribute to the development of new functional catalysts that could be used to promote reactions effectively and efficiently. Although the reactions were carried out in a laboratory-scale, it is expected that these reported results would undergo modification for scalability toward industrial application for mass production.

1.7 References

- (1) Tanabe, K.; Yoshii, N.; Hattori, H. *J. Chem. Soc. Chem. Commun.* **1971**, No. 9, 464.
- (2) Matsushashi, H. *Top. Catal.* **2009**, *52* (6–7), 828–833
- (3) Matsushashi, H.; Fujita, T. *Catal. Today* **2011**, *164* (1), 131–134
- (4) Ono, Y.; Hattori, H. *Solid Base Catalysis*; Castleman, A. W., Toennies, J. P., Yamanouchi, K., Zinth, W., Springer Berlin Heidelberg: Berlin, Heidelberg, 2011; Vol. 101.
- (5) Elvira, G.-B.; Francisco, G.-C.; Víctor, S.-M.; Alberto, M.-L. R. *J. Environ. Sci.* **2017**, *57*, 418–428.
- (6) Constantino, V. R. L.; Pinnavaia, T. J. *Catal. Lett.* **1994**, *23* (3–4), 361–367.
- (7) Yashima, T. *J. Catal.* **1972**, *26* (3), 303–312.
- (8) Wang, Y.; Zhu, M.; Kang, L.; Dai, B. *Microporous Mesoporous Mater.* **2014**, *196*, 129–135.
- (9) Nyman, M. *Dalton Trans.* **2011**, *40* (32), 8049.
- (10) Long, D.-L.; Tsunashima, R.; Cronin, L. *Angew. Chem. Int. Ed.* **2010**, *49* (10), 1736–1758.
- (11) Gumerova, N. I.; Rompel, A. *Chem. Soc. Rev.* **2020**, *49* (21), 7568–7601.
- (12) Sadeghi, O.; Zakharov, L. N.; Nyman, M. *Science* **2015**, *347* (6228), 1359–
- (13) Tucher, J.; Nye, L. C.; Ivanovic-Burmazovic, I.; Notarnicola, A.; Streb, C. *Chem. - Eur. J.* **2012**, *18* (35), 10949–10953.
- (14) Seliverstov, A.; Streb, C. *Chem. Commun.* **2014**, *50* (15), 1827.
- (15) Seliverstov, A.; Streb, C. *Chem. - Eur. J.* **2014**, *20* (31), 9733–9738.
- (16) Mialane, P.; Dolbecq, A.; Lisnard, L.; Mallard, A.; Marrot, J.; Sécheresse, F. *Angew. Chem. Int. Ed.* **2002**, *41* (13), 2398.
- (17) Misra, A.; Kozma, K.; Streb, C.; Nyman, M. *Angew. Chem. Int. Ed.* **2020**, *59* (2), 596–612.
- (18) Howarth, O. W.; Jarrold, M. *J. Chem. Soc. Dalton Trans* **1978**, No. 5, 503–506.
- (19) Maksimovskaya, R. I.; Maksimov, G. M. *Inorg. Chem.* **2007**, *46* (9), 3688–3695.
- (20) Isobe, M.; Marumo, F.; Yamase, T.; Ikawa, T. *Acta Crystallogr. B* **1978**, *34* (9), 2728–2731.
- (21) Himeno, S.; Niiya, H.; Ueda, T. *Bull. Chem. Soc. Jpn.* **1997**, *70* (3), 631–637.
- (22) Lindqvist, I. *Acta Crystallogr.* **1950**, *3* (2), 159–160.
- (23) Fuchs, J.; Knöpnadel, I. *Cryst. Mater.* **1982**, *158* (1–2), 165–180.
- (24) Amini, M.; Naslhajian, H.; Farnia, S. M. F.; Hołyńska, M. *Eur. J. Inorg. Chem.* **2015**, *2015* (23), 3873–3878.
- (25) Cruywagen, J. J.; Van Der Merwe, I. F. J. *J. Chem. Soc. Dalton Trans.* **1987**, No. 7, 1701.
- (26) Hastings, J. J.; Howarth, O. W. *J. Chem. Soc. Dalton Trans.* **1992**, No. 2, 209.
- (27) Maksimovskaya, R. I.; Burtseva, K. G. *Polyhedron* **1985**, *4* (9), 1559–1562.
- (28) Wang, X.; Cao, J.; Huang, K.; Xu, Y.; Chi, Y.; Hu, C. *Eur. J. Inorg. Chem.* **2013**, *2013* (10–11), 1788–1792.
- (29) Lindqvist, I. *Acta Crystallogr.* **1952**, *5* (5), 667–670.
- (30) Nolan, A. L.; Wilkes, E. N.; Hambley, T. W.; Allen, C. C.; Burns, R. C.; Lawrance, G. A. *Aust. J. Chem.* **1999**, *52* (10), 955.
- (31) Asami, M.; Ichida, H.; Sasaki, z. *Acta Crystallogr. C* **1984**, *40* (1), 35–37
- (32) Fuchs, J.; Hartl, H.; Schiller, W. *Angew. Chem. Int. Ed. Engl.* **1973**, *12* (5), 420–420.
- (33) Pradeep, C. P.; Long, D.-L.; Kögerler, P.; Cronin, L. *Chem. Commun.* **2007**, No. 41, 4254.

- (34) Nyman, M.; Alam, T. M.; Bonhomme, F.; Rodriguez, M. A.; Frazer, C. S.; Welk, M. E. *J. Clust. Sci.* **2006**, *17* (2), 197–219.
- (35) Martin, N. P.; Petrus, E.; Segado, M.; Arteaga, A.; Zakharov, L. N.; Bo, C.; Nyman, M. *Chem. – Eur. J.* **2019**, *25* (45), 10580–10584.
- (36) Müscher-Polzin, P.; Näther, C.; Bensch, W. *Z. Für Anorg. Allg. Chem.* **2020**, *646* (3), 193–198.
- (37) Bontchev, R. P.; Nyman, M. *Angew. Chem. Int. Ed.* **2006**, *45* (40), 6670–6672.
- (38) Huang, P.; Qin, C.; Su, Z.-M.; Xing, Y.; Wang, X.-L.; Shao, K.-Z.; Lan, Y.-Q.; Wang, E.-B. *J. Am. Chem. Soc.* **2012**, *134* (34), 14004–14010.
- (39) Maekawa, M.; Ozawa, Y.; Yagasaki, A. *Inorg. Chem.* **2006**, *45* (24), 9608–9609
- (40) Matsumoto, M.; Ozawa, Y.; Yagasaki, A.; Zhe, Y. *Inorg. Chem.* **2013**, *52* (14), 7825–7827.
- (41) Son, J.; Casey, W. H. *Chem. – Eur. J.* **2016**, *22* (40), 14155–14157.
- (42) Olah, G. A.; Surya Prakash, G. K.; Molnr, R.; Sommer, J. *Superacid Chemistry*; John Wiley & Sons, Inc.: Hoboken, NJ, USA, 2009.
- (43) Hashimoto, M.; Selling, A.; Håkansson, M.; Pettersson, L.; Ahlgrén, M.; Pursiainen, J.; Wang, H.-G.; Yao, X.-K.; Wang, H.-G.; Tuchagues, J.-P.; Ögren, M. *Acta Chem. Scand.* **1999**, *53*, 305–313.
- (44) Sugahara, K.; Kimura, T.; Kamata, K.; Yamaguchi, K.; Mizuno, N. *Chem. Commun.* **2012**, *48* (67), 8422.
- (45) Hayashi, S.; Sasaki, N.; Yamazoe, S.; Tsukuda, T. *J. Phys. Chem. C* **2018**, *122* (51), 29398–29404.
- (46) Kikkawa, S.; Fukuda, S.; Hirayama, J.; Shirai, N.; Takahata, R.; Suzuki, K.; Yamaguchi, K.; Teranishi, T.; Yamazoe, S. *Chem. Commun.* **2022**, *58* (64), 9018–9021.
- (47) Chen, X.; Zhou, Y.; Roy, V. A. L.; Han, S. *Adv. Mater.* **2018**, *30* (3), 1703950.
- (48) Balliou, A.; Papadimitropoulos, G.; Skoulatakis, G.; Kennou, S.; Davazoglou, D.; Gardelis, S.; Glezos, N. *ACS Appl. Mater. Interfaces* **2016**, *8* (11), 7212–7220.
- (49) Balliou, A.; Douvas, A. M.; Normand, P.; Tsikritzis, D.; Kennou, S.; Argitis, P.; Glezos, N. *J. Appl. Phys.* **2014**, *116* (14), 143703.
- (50) Li, H.; Pang, S.; Wu, S.; Feng, X.; Müllen, K.; Bubeck, C. *J. Am. Chem. Soc.* **2011**, *133* (24), 9423–9429.
- (51) Vilà-Nadal, L.; Mitchell, S. G.; Markov, S.; Busche, C.; Georgiev, V.; Asenov, A.; Cronin, L. *Chem. – Eur. J.* **2013**, *19* (49), 16502–16511.
- (52) Xu, Q.; Niu, Y.; Wang, G.; Li, Y.; Zhao, Y.; Singh, V.; Niu, J.; Wang, J. *Mol. Catal.* **2018**, *453*, 93–99.
- (53) Hayashi, S.; Yamazoe, S.; Koyasu, K.; Tsukuda, T. *Chem. – Asian J.* **2017**, *12* (13), 1635–1640.
- (54) Kamata, K.; Sugahara, K. *Catalysts* **2017**, *7* (11), 345.
- (55) Zhang, Y.; Wang, H.; Yuan, H.; Shi, F. *ACS Sustain. Chem. Eng.* **2017**, *5* (7), 5758–5765.
- (56) Mitsudome, T.; Urayama, T.; Fujita, S.; Maeno, Z.; Mizugaki, T.; Jitsukawa, K.; Kaneda, K. *ChemCatChem* **2017**, *9* (19), 3632–3636.

Chapter 2. Superbase catalysis of metal oxide clusters

2.1. Introduction

Acid-base catalysis is one of the fundamental and important reactions employed in organic reactions to produce useful and value-added chemicals. In addition to base catalyst, superbase is defined by the pK_a value of 26 or higher. Organic lithium is widely used as superbase reagent; however the disadvantage is its high reactivity when exposed to oxygen or water in the atmosphere. Alternatively, phosphazene superbases,¹⁻³ chiral amine compounds,^{4,5} and other basic amino compounds,⁶ which are utilized in the production of pharmaceuticals, fragrances, and cosmetics, and other value-added chemicals due to their ability to provide high precision in the control of stereochemistry. The complicated preparation of these catalysts accompanied with high cost. As a result, a development of catalyst with ease of preparation while maintaining high activity is desired.

Solid base catalyst such as magnesium oxide, calcium oxide, or rare-earth metal oxides also have been employed for industrial processes. O atoms of the metal oxides are the basic sites of these catalysts. The basicity of MgO was proposed to be enhanced by doping alkali metals to generate superbase sites. Superbase sites were reported to be O_2^- ions on three-coordinated sites on the corners or the (111) microplanes (Figure 2-1).⁷

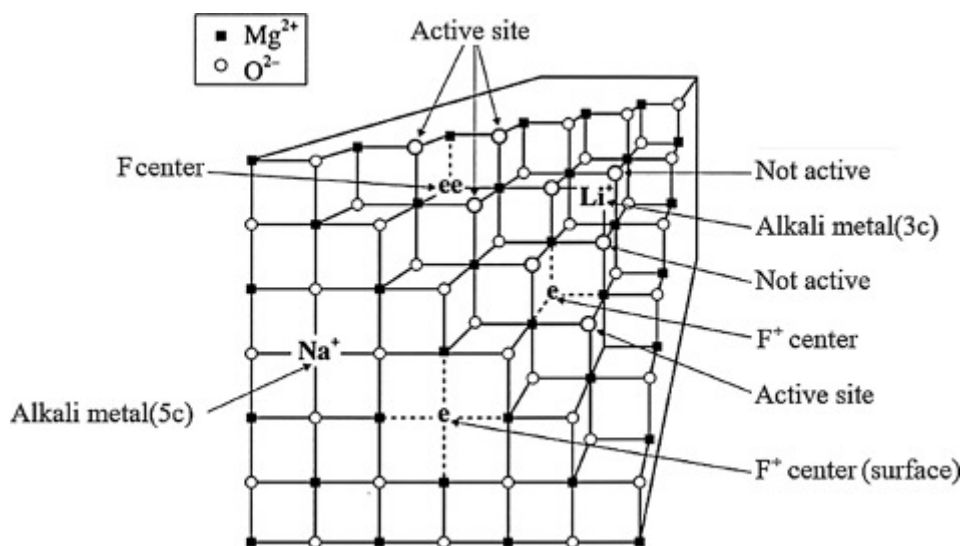


Figure 2-1. Alkali metals-doped MgO to generate superbase sites.⁷

Besides doping metal ions to generate superbase site, Sun *et al.* reported the preparation of mesoporous superbase catalyst by using KNO_3 and $Al(NO_3)_3$ as the precursors (Figure 2-2).⁸ The pH of the solution was controlled by K_2CO_3 . The hydrolysis of $Al(NO_3)_3$

with KNO_3 afforded K_2O which is a superbase on $\gamma\text{-Al}_2\text{O}_3$ support. The superbase catalysis was elucidated by conducting isomerization of 1-hexene.⁸

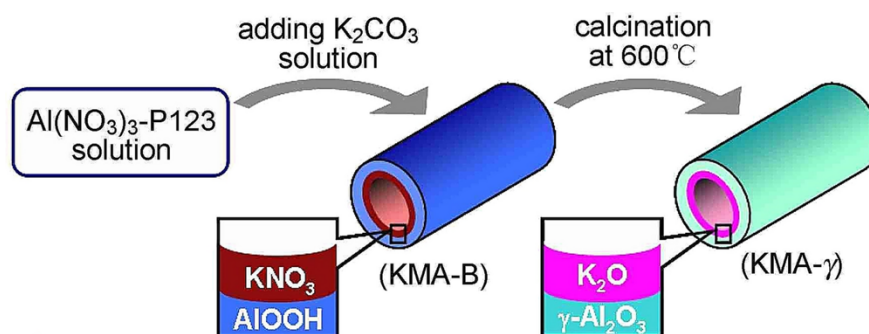


Figure 2-2. Preparation of potassium-functionalized mesoporous γ -alumina by one-pot synthesis.⁸

A modification of CaO by covering with Al_2O_3 to improve water tolerance was reported.⁹ The model reaction used to evaluate basicity of the catalyst was retro-aldol reaction of diacetone to acetone. Figure 2-3 demonstrated the reaction result in two states of the catalyst, the 10wt% of Al^{3+} on CaO ($\text{Al}_2\text{O}_3/\text{CaO-10}$) in the presence of 5wt% of water afforded conversion in circular marks, in which the same catalyst was recovered and washed with acetone. After drying, it was subsequently employed in the reaction with the results shown in square marks.⁹ These results indicated the preferential adsorption of water on the surface of the catalyst over diacetone and therefore significantly reduced the catalytic performance, however, this catalyst could be recovered and active after drying the surface from water suggesting stability after exposing to water.

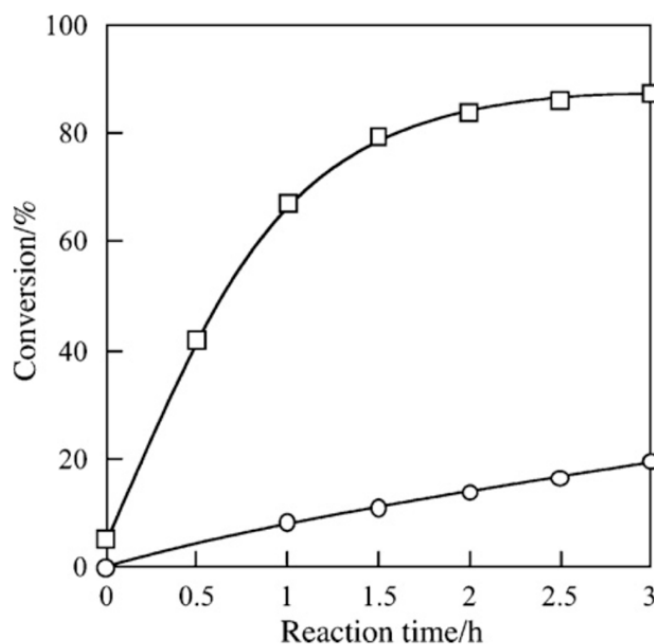
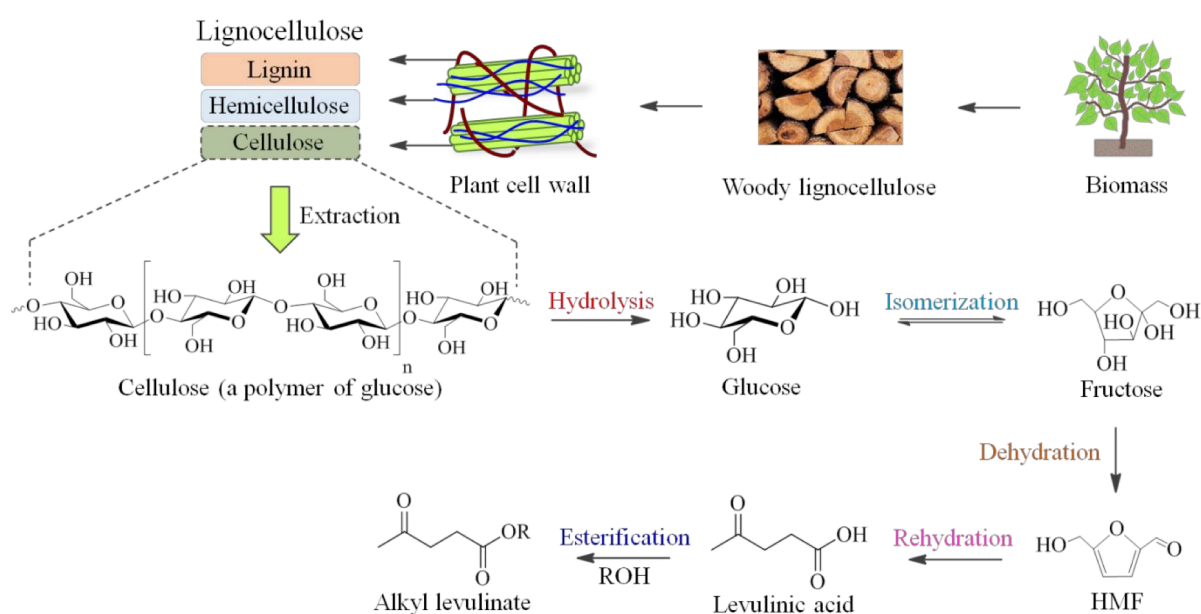


Figure 2-3. Results of retro-aldol reaction of diacetone promoted by $\text{Al}_2\text{O}_3/\text{CaO-10}$ in the presence of 5wt% of water (circular marks) and the dried $\text{Al}_2\text{O}_3/\text{CaO-10}$ in an absence of water (square marks).⁹

Although some developments have been implemented to improve the stability against the water exposure, solid base catalysts would nevertheless be deactivated in the presence of water or CO₂ in the atmosphere that would form inactive phase on the surface of the catalyst. Therefore, the utilization of solid base catalyst is limited to certain reactions or dry processes. The importance of water tolerance of acid-base catalyst has risen due to the potential in application of biomass conversion to produce value-added chemicals (Scheme 2-1).¹⁰⁻¹² Such reactions would result in aqueous solution of aldehydes or ketones,¹³⁻¹⁵ thus it is necessary to develop base catalyst with high water tolerance.



Scheme 2-1. General reaction scheme for biomass conversion reactions.¹⁰

Alternatively, water tolerant base catalysts that have been reported thus far include mixed metal layered double hydroxides with general structure of $[M^{II}_{1-x}M^{III}_x(OH)_2]^{x+}[A^{n-x/n}]^{x-} \cdot yH_2O$ (M: metal, A: anion) (Figure 2-3). These materials could maintain their structure and basicity in the presence of water. However, their basicity remained low and therefore limited the application in base catalysis.^{16,17}

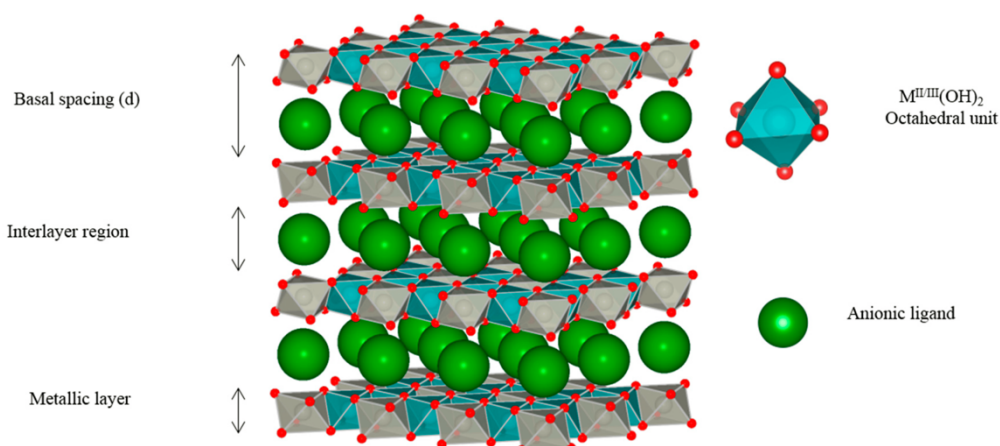


Figure 2-3. General structure of layered double hydroxides.¹⁸

In the past decade, catalysis driven by metal oxide clusters or polyoxometalates have been investigated. Metal oxide clusters have been known as acid and redox catalysts. Until 2012, when Sugahara *et al.* reported the first discovery of basicity in polyoxometalates with Ge-doped polyoxotungstates, $[\gamma\text{-H}_2\text{GeW}_{10}\text{O}_{36}]^{6-}$, with high $\text{p}K_{\text{a}}$ value of 21.9 elucidated by Knoevenagel condensation reaction by employing the cluster as the homogeneous catalyst.¹⁹ The key for metal oxide clusters to act as base catalyst was related to the negative charge of the clusters. The higher negatively charged the clusters led to the stronger basicity of the constituent O atoms. This relationship was further proven by an increase of negative charge from -6 to -7 in the deprotonated $[\gamma\text{-HGeW}_{10}\text{O}_{36}]^{7-}$.²⁰ The catalytic performance was drastically improved from the -6 moiety. Since then, basicity in metal oxide clusters have been studied and reported, including Keggin-type $[\text{P}_2\text{W}_{17}\text{NbO}_{62}]^{7-}$ and $[\text{SiNb}_{12}\text{O}_{40}]^{16-}$ with $\text{p}K_{\text{a}}$ value of 13.1,²¹⁻²³ decaniobate, $[\text{Nb}_{10}\text{O}_{28}]^{6-}$, along with Lindqvist-type hexametalates, $[\text{Ta}_6\text{O}_{19}]^{8-}$ and $[\text{Nb}_6\text{O}_{19}]^{8-}$, which have been reported with $\text{p}K_{\text{a}}$ value up to 23.8 according to result of Knoevenagel condensation reaction (Figure 2-4).²⁴⁻²⁶

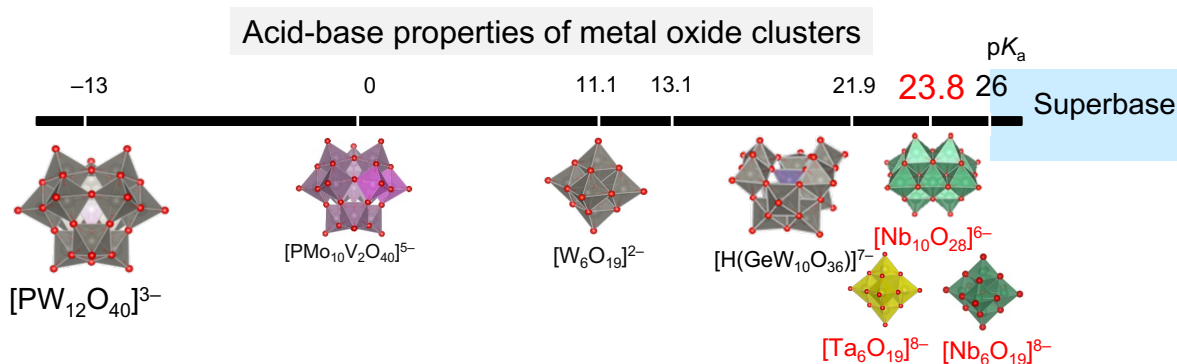


Figure 2-4. The acid-base properties of metal oxide clusters reported.

From the abovementioned reasons and the increasing in development of biomass conversion, the development of water-tolerant superbase catalyst that possess equivalent base

Chapter 2

strength to that of organic lithium should be implemented. Since the Lindqvist-type metal oxide clusters have high activity for Knoevenagel condensation of nitrile with pK_a of 23.8, while the limit has not yet been defined. In this study, the potential of metal oxide clusters, focusing on $[\text{Nb}_6\text{O}_{19}]^{8-}$, as superbases catalyst would be investigated. Moreover, the high activity of $[\text{Nb}_6\text{O}_{19}]^{8-}$ for Knoevenagel condensation reactions implied that the catalyst may tolerate the presence of water and thus would also be elucidated in this chapter.

2.2 Experimental

Nb_2O_5 was purchased from Kojundo Chemical Laboratory Co., Ltd., $\text{K}_8[\text{Nb}_6\text{O}_{19}] \cdot n\text{H}_2\text{O}$ was purchased from Mitsuwa Chemicals Co., Ltd., benzaldehyde (BA), dimethyl sulfoxide (DMSO, super dehydrated), acetone (super dehydrated), hydrochloric acid (HCl), and $\text{Na}_2\text{C}_2\text{O}_4$ were purchased from Fujifilm Wako Pure Chemical Corp. Ltd.. Tetrabutylammonium hydroxide (TBAOH) aqueous solution (40%), pinacolone, norcamphor, cycloheptanone, 3-pentanone, cyclohexanone, phenylacetonitrile, (4-methoxyphenyl)acetonitrile, (4-cyanophenyl)acetonitrile, propionitrile, bromothymol blue, phenolphthalein, 2,4-dinitroaniline, 4-chloroaniline, 2,2-dimethylcyclopentanone, (+)-camphor were purchased from Tokyo Chemical Industry Co., Ltd. Hexane, biphenyl, and $(\text{NH}_2)_2\text{CO}$ were purchased from Kanto Chemical Co., Inc. MgO (JRC-MgO-500A) was supplied from Catalysis Society of Japan. All reagents were used as received.

Density functional theory (DFT) calculations, intrinsic reaction coordinate (IRC) calculation, and natural bonding orbital (NBO) analysis of $[\text{Nb}_6\text{O}_{19}]^{8-}$ were performed by using the Gaussian 16 program, in accordance with the literature.²⁴ The optimized structures of the $[\text{Nb}_6\text{O}_{19}]^{8-}$ were calculated by B3LYP incorporating the solvation effect of DMSO using PCM (dielectric constant = 46.826) using LANL2DZ basis sets for Nb atoms, and 6-31++G(d,p) basis sets for O, C and H atoms.

2.2.1 Synthesis of NaNbO_3

NaNbO_3 was prepared by modified solid-state method by grinding the mixture of Nb_2O_5 with $\text{Na}_2\text{C}_2\text{O}_4$ and $(\text{NH}_2)_2\text{CO}$ with molar ratio of 1:1:4 for 10 minutes using alumina agate and mortar.²⁷ The mixture was calcined in alumina crucible at 600°C for 4 h at the heating rate of 2.5°C/min. After the first calcination, the mixture was ground with additional $(\text{NH}_2)_2\text{CO}$ with the same amount used in the first mixture prior to calcination again at 600°C for 4 h to remove impurities.

2.2.2 Synthesis of Na_3NbO_4

The prepared NaNbO_3 was ground with $\text{Na}_2\text{C}_2\text{O}_4$ and $(\text{NH}_2)_2\text{CO}$ with molar ratio of 1:1:3 for 10 minutes using alumina agate and mortar. The ground powder was calcined at 900°C for 4 h with the same heating rate of 2.5°C/min to obtain Na_3NbO_4 .

2.2.3 Synthesis of $\text{Nb}_2\text{O}_5 \cdot n\text{H}_2\text{O}$

Two methods could be employed to obtain $\text{Nb}_2\text{O}_5 \cdot n\text{H}_2\text{O}$, the first one is to use Na_3NbO_4 as the precursor by washing it with water (15 mL) twice and followed by extraction with water (45 mL) to obtain aqueous solution of $\text{Na}_8[\text{Nb}_6\text{O}_{19}]$. The acidification of $\text{Na}_8[\text{Nb}_6\text{O}_{19}]$ by 1 M HCl would result in $\text{Nb}_2\text{O}_5 \cdot n\text{H}_2\text{O}$. Alternatively, $\text{Nb}_2\text{O}_5 \cdot n\text{H}_2\text{O}$ could be prepared from acidifying $\text{K}_8[\text{Nb}_6\text{O}_{19}] \cdot n\text{H}_2\text{O}$ with 1 M HCl followed by collection of white solid precipitate by centrifugation. The precipitate from either method was washed with pure water until the pH of the supernatant became neutral. After washing, it was dried under vacuum for 2 h prior to drying in oven at 60°C overnight.

2.2.4 Synthesis of $\text{TBA}_6\text{H}_2[\text{Nb}_6\text{O}_{19}]$ (TBA-Nb₆)

$\text{Nb}_2\text{O}_5 \cdot n\text{H}_2\text{O}$ was reacted with tetrabutylammonium hydroxide (TBAOH) aqueous solution (10%) using microwave-assisted hydrothermal reactor (Initiator+ Biotage, Ltd.) at 180°C for 5 minutes.²⁸ The obtained clear, colorless solution was filtered using syringe filter (polyethersulfone, PES, 0.22 μm) to remove unreacted precursors. The filtrate was lyophilized and washed with hexane, this step was repeated for three times to remove tributylamine that came from decomposition of TBAOH during lyophilization. The obtained $\text{TBA}_6\text{H}_2[\text{Nb}_6\text{O}_{19}]$ (TBA-Nb₆) was characterized by Fourier-transform infrared spectrometer (JASCO, FT/IR-4600) equipped with attenuated total reflection accessory (JASCO, ATR PRO ONE), electrospray ionization-mass spectrometry (ESI-MS) in negative ion mode with 1 M aqueous solution (micrOTOF-II, Bruker), CHN elemental analysis (UNICUBE, Elementar Japan Co., Ltd.), and X-ray absorption fine structure (XAFS, BL01B1, SPring-8). The amount of TBA cation was determined by:

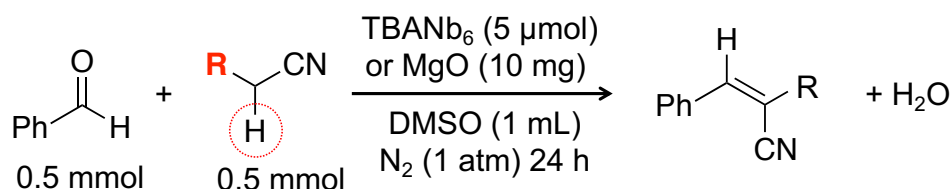
$$TBA \text{ unit} = \frac{Mass_{CHN}}{Mass_{TBA}}$$

where $Mass_{CHN}$ refers to the total content of C, H, and N determined by elemental analysis and $Mass_{TBA}$ is molecular weight of TBA ($\text{C}_{16}\text{H}_{36}\text{N} = 242.78 \text{ g mol}^{-1}$). The excess H units would be determined as counter cation.

2.2.5 General procedure for Knoevenagel condensation

Knoevenagel condensation reaction was conducted in a batch-type reactor, prepared under N_2 atmosphere in glovebox. The reactor attached to gas balloon (1 L) was degassed and purged three times with N_2 (1 atm) prior to the reaction. General reaction scheme is depicted in Scheme 2-2, using 0.5 mmol of benzaldehyde (BA) and 0.5 mmol of nitrile as substrates in

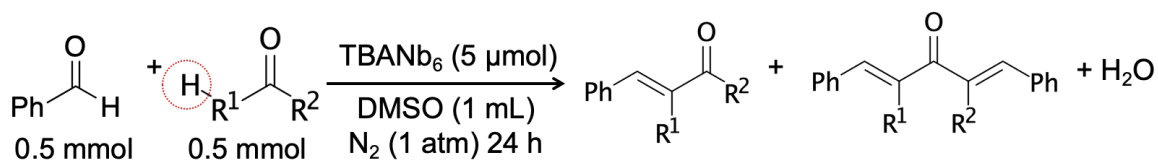
the presence of 0.1 mmol of biphenyl as an internal standard. The catalyst loading was 5 μmol for TBA-Nb₆ or 10 mg for MgO which was activated at 600°C for 2 h under vacuum. Super dehydrated DMSO (1 mL) was used as a solvent. The reaction solution was analyzed using gas chromatography equipped with flame ionization detector (GC-FID, Shimadzu, GC-2014 with column Restex, Rtx-1) and gas chromatography-mass spectrometry (GC-MS, Shimadzu, GCMS-QP2010 SE with column Agilent, DB-1MS).



Scheme 2-2. Reaction scheme for Knoevenagel condensation reaction.

2.2.6 General procedure for aldol condensation

Aldol condensation reaction was conducted in a batch-type reactor, prepared under N₂ atmosphere in glovebox. The reactor attached to gas balloon (1 L) was degassed and purged three times with N₂ (1 atm) prior to the reaction. General reaction scheme is depicted in Scheme 2-3, using 0.5 mmol of benzaldehyde (BA) and 0.5 mmol of ketone as substrates in the presence of 0.1 mmol of biphenyl as an internal standard. The catalyst loading was 5 μmol for TBA-Nb₆. Super dehydrated DMSO was used as a solvent. The reaction solution was analyzed using GC-FID and GC-MS.



Scheme 2-3. Reaction scheme for aldol condensation reaction.

2.2.7 Calculation of product yield

$$\text{Conversion}(\%) = \left(1 - \frac{\text{Area}_{\text{Sub.}}}{\text{Area}_{\text{IS}}} \times \frac{\text{Area}_{\text{IS},0}}{\text{Area}_{\text{Sub},0}} \right) \times 100$$

$$\text{Yield}(\%) = \frac{\text{Area}_{\text{Pro.}}}{\text{Area}_{\text{IS}}} \times \frac{\text{ECN}_{\text{Sub.}}}{\text{ECN}_{\text{Pro.}}} \times \frac{\text{Area}_{\text{IS},0}}{\text{Area}_{\text{Sub},0}} \times 100$$

where, *Sub.*, substrate (BA); *IS*, internal standard (biphenyl); *Pro.*, product; *ECN* = effective carbon number. subscripted 0 means the peak area reaction solution without catalyst.

Calculation of turn over number (TON) and turn over frequency (TOF):

$$\text{TON} = \frac{\text{Moles of product}}{\text{Moles of catalyst}}$$

$$\text{TOF} = \frac{\text{TON}}{\text{Time}}$$

2.2.8 Illustration of catalysts

The obtained crystallographic data were used to visualize the structure of catalysts using VESTA program.²⁹

2.3 Results and discussion

2.3.1 Synthesis of NaNbO_3

NaNbO_3 and Na_3NbO_4 were prepared by modified solid-state reaction using Nb_2O_5 , $\text{Na}_2\text{C}_2\text{O}_4$, and $(\text{NH}_2)_2\text{CO}$ as the precursors. After calcination, the obtained product was characterized by XRD (Figure 2-5).

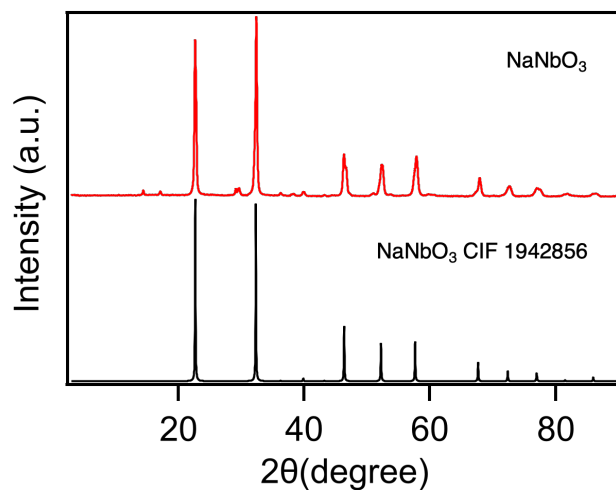


Figure 2-5. XRD pattern of NaNbO_3 (red) compared to the reference (CIF number 1942856, black).

2.3.2 Synthesis of Na_3NbO_4

A mixture of NaNbO_3 , $\text{Na}_2\text{C}_2\text{O}_4$, and $(\text{NH}_2)_2\text{CO}$ in a molar ratio of 1:1:3 was calcined to obtain Na_3NbO_4 . The structure was confirmed using XRD (Figure 2-6).

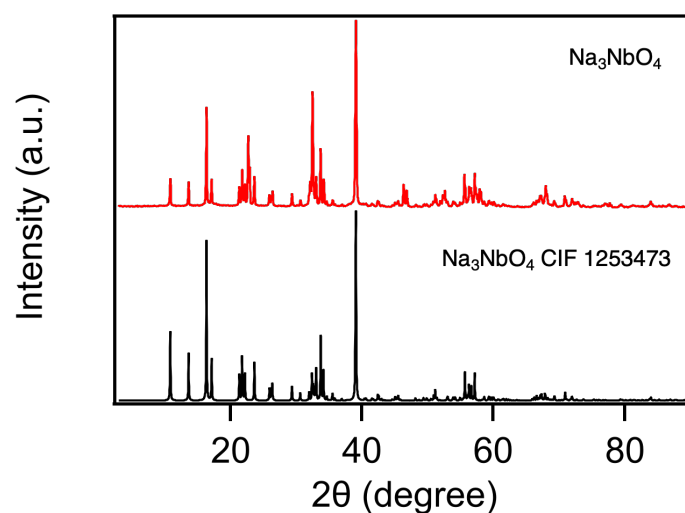


Figure 2-6. XRD pattern of Na_3NbO_4 (red) along with the reference (CIF number 1253473, black).

2.3.3 Synthesis of $\text{TBA}_6\text{H}_2[\text{Nb}_6\text{O}_{19}]$ (TBA-Nb₆)

$\text{Nb}_2\text{O}_5 \cdot n\text{H}_2\text{O}$ was used as a precursor for synthesis of TBA-Nb₆ using microwave-assisted hydrothermal reactor. The utilization of microwave-assisted hydrothermal reactor provided higher efficiency by increasing product yield and shortening reaction time comparing to the conventional reflux reaction. In addition, the prolonged reflux over 24 h could result in decomposition of TBA cation, where the product could be obtained as $\text{TBA}_4\text{H}_4[\text{Nb}_6\text{O}_{19}]$ rather than $\text{TBA}_6\text{H}_2[\text{Nb}_6\text{O}_{19}]$. Microwave-assisted hydrothermal method thus also improved the quality of the obtained product and reduced proton poisoning. The composition of synthesized TBA-Nb₆ was analyzed by ESI-MS where the results suggested the main composition corresponding to $\text{TBA}_n\text{H}_x[\text{Nb}_6\text{O}_{19}]^{8-x-n}$ with TBA units ranged from 2–4, as shown in Figure 2-7.

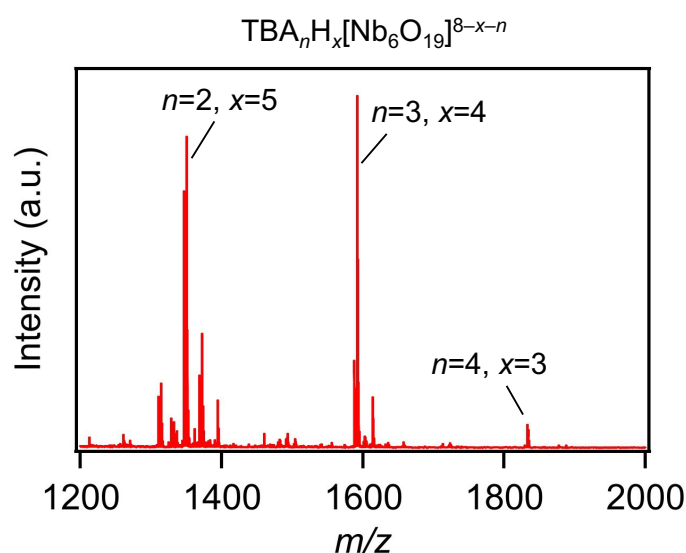


Figure 2-7. ESI-MS spectrum of the aqueous solution of $\text{TBA}_n\text{H}_x[\text{Nb}_6\text{O}_{19}]^{8-x-n}$ measured in negative ion mode.

The vibration corresponding to terminal $\text{Nb}=\text{O}_t$ bonding ($800\text{--}900\text{ cm}^{-1}$) and bridging $\text{Nb}-\text{O}_b-\text{Nb}$ ($480\text{--}600\text{ cm}^{-1}$ and $620\text{--}780\text{ cm}^{-1}$) were observed in the FT-IR spectrum (Figure 2-8). These vibrations correspond to the Lindqvist-type structure of $[\text{M}_6\text{O}_{19}]$.

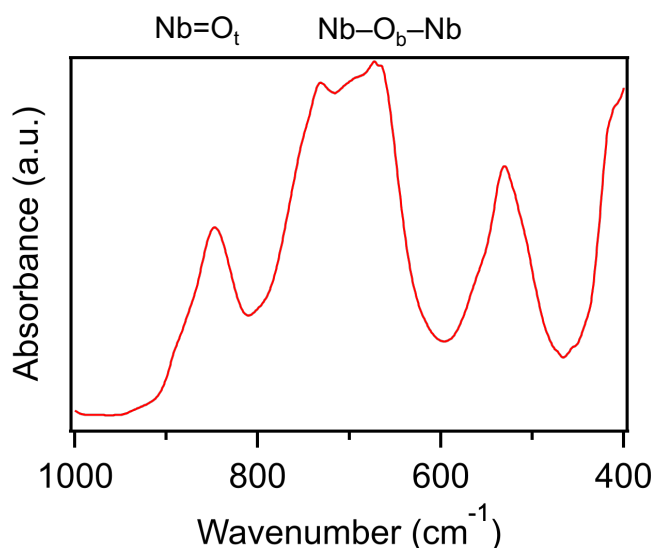


Figure 2-8. The FT-IR spectrum of TBA₆H₂[Nb₆O₁₉] measured in ATR mode.

Elemental analysis was used to analyze content of C, H, and N to calculate the amount of TBA unit and the amount of proton as counter cations of the cluster. The amount of Nb was estimated from X-ray absorption confirming the purity of the synthesized TBA-Nb₆ (Table 2-1). The characterization results confirmed a successful synthesis of TBA₆H₂[Nb₆O₁₉].

Table 2-1. Elemental analysis data of TBA₆H₂[Nb₆O₁₉]

	C ^a (%)	H ^a (%)	N ^a (%)	TBA amount	H amount	Nb ^b (%)
TBA-Nb ₆	45.29	9.42	3.43	6.0	2.0	27

^aDetermined by elemental analysis.

^bEstimated by Nb K-edge X-ray absorption.

After confirming the purity of the synthesized TBA-Nb₆, it was employed as the catalyst for the Knoevenagel condensation reaction (Scheme 2-2). First, the reaction was conducted at 70°C and compared the activity with MgO as one of the well-known solid base catalysts possessing high basicity. The result demonstrated higher base strength of TBA-Nb₆ than MgO which resulted in higher activity in condensation between benzaldehyde (BA) and both nitriles, such as phenylacetonitrile (pK_a = 21.9) and (4-methoxyphenyl)acetonitrile (pK_a = 23.8) (Figure 2-9). While MgO showed reduced activity when substrate with higher pK_a was used, such lower activity was not observed in the case of TBA-Nb₆.

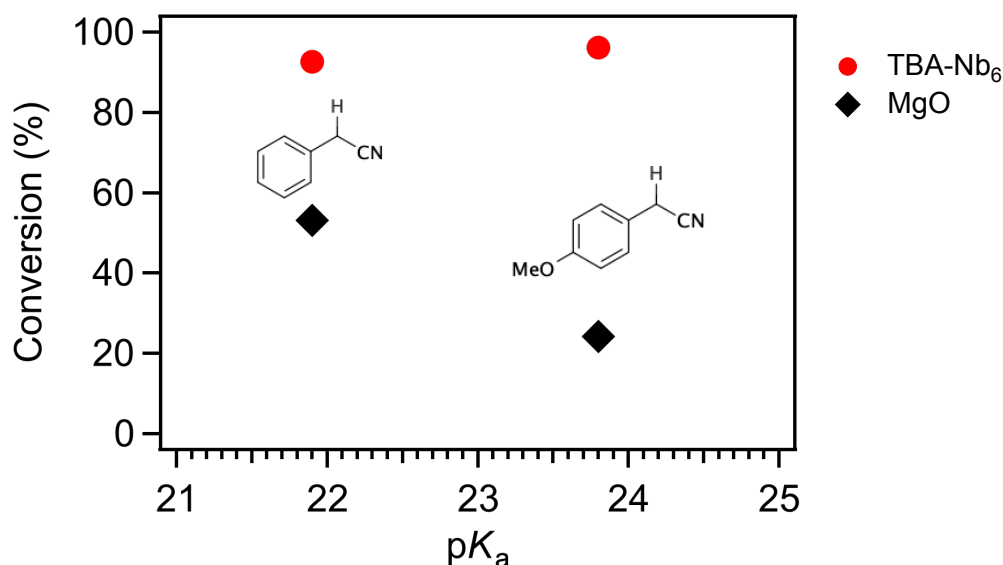


Figure 2-9. Catalytic activity (BA conversion) of Knoevenagel condensation using TBA-Nb₆ (5 μmol) as catalyst (red dot) and MgO (10 mg) as catalyst (black dot). Reaction condition: substrates: BA, 0.5 mmol; nitrile, 0.5 mmol; catalyst loading: TBA-Nb₆ (5 μmol) or MgO (10 mg) solvent: DMSO, 1 mL (super dehydrated); atmosphere: N₂ (1 atm); temperature: 70°C; reaction time: 24 h.

Furthermore, TBA-Nb₆ could even promoted Knoevenagel condensation at lower temperature (30°C) with slightly higher activity than 70°C in the case of phenylacetonitrile (pK_a = 21.9) and (4-methoxyphenyl)acetonitrile (pK_a = 23.8) as substrates (Figure 2-10). To evaluate the basicity of TBA-Nb₆, nitrile with significantly higher pK_a value such as propionitrile (pK_a = 32.0) was used as a substrate, where the catalytic activity was not observed. The gap between pK_a values of 23.8 and 32.0 was therefore evaluated by aldol condensation between benzaldehyde and ketones (Scheme 2-3), such as pinacolone (pK_a = 27.7) and norcamphor (pK_a = 29.0). The results surprisingly indicated that TBA-Nb₆ could be regarded as a superbases catalyst due to its high catalytic performance with substrate whose pK_a value is greater than 26. This finding is, to the best of knowing, the first report of superbases catalysis in the field of metal oxide clusters.

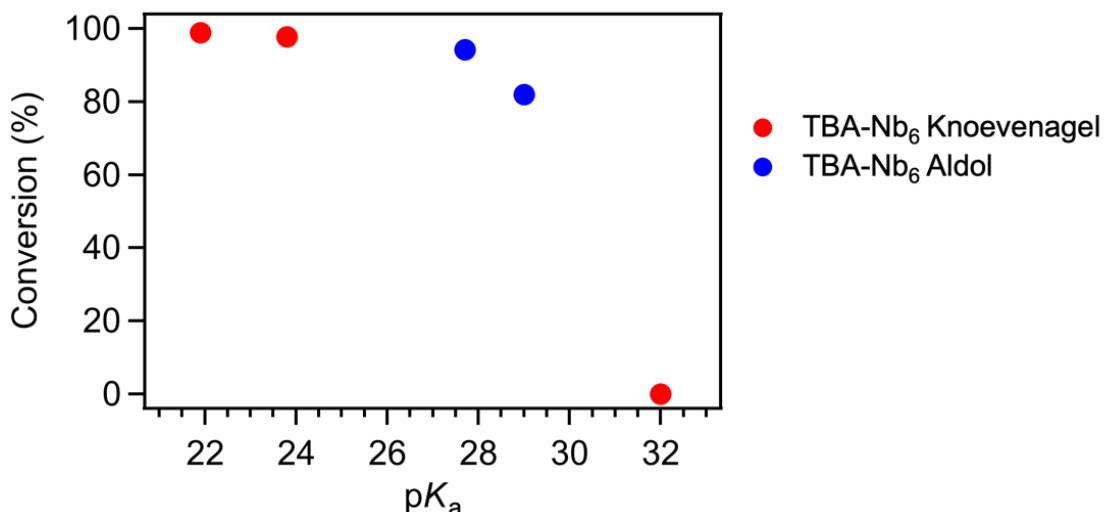


Figure 2-10. Catalytic activity (BA conversion) of Knoevenagel condensation (red dot) and aldol condensation (blue dot) using TBA-Nb₆ (5 μ mol) as the catalyst. Reaction condition: substrates: BA, 0.5 mmol; nitrile, 0.5 mmol; solvent: DMSO, 1 mL (super dehydrated); atmosphere: N₂ (1 atm); temperature: 30°C; reaction time: 24 h.

The yield of the condensate products was compared in Figure 2-11, in which two observations could be made. The first one being the trend of decreasing in product yield with higher base strength or pK_a value of the substrate that corresponding to the decreasing in conversion of BA shown in Figure 2-10. This trend is easily understandable as the base strength of the substrate increased and reaching the base strength of the TBA-Nb₆. The latter one is the lower yield of product when using cycloheptanone whose pK_a value is the same as pinacolone. It should be noted that lower ratio of substrate to catalyst was lower in the case of cycloheptanone than pinacolone. This result indicated another important factor that affect the condensation reaction, which is the steric hindrance of the substrate. For pinacolone, β -proton is located at the carbon of the methyl group of the substrate, while in the case of cycloheptanone, the β -proton is bound to cyclic carbon, which is more stable and attributed to lower abstraction.

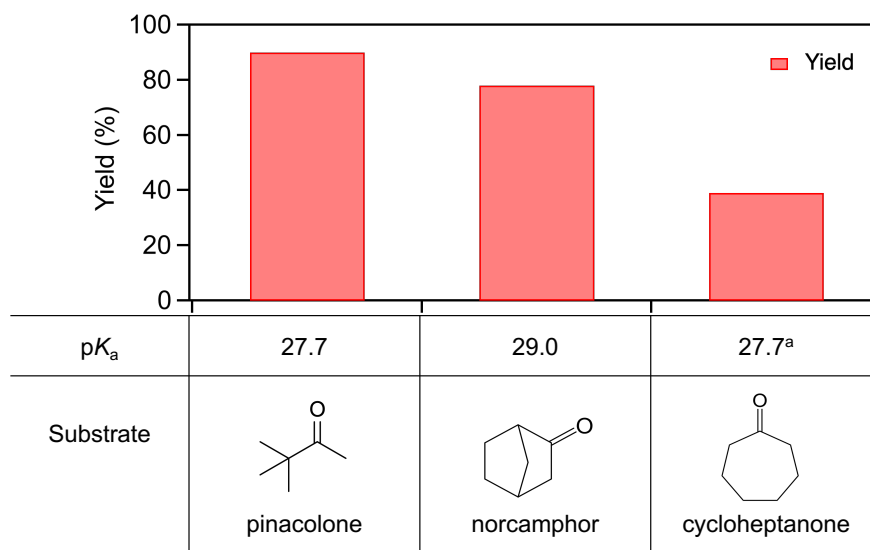


Figure 2-11. The aldol condensation reaction results between BA and ketones. Reaction condition: substrates: BA, 0.5 mmol; ketone, 0.5 mmol; solvent: DMSO, 1 mL (super dehydrated); atmosphere: N₂ (1 atm); temperature: 30°C; reaction time: 24 h.

^aSubstrates: BA, 0.1 mmol; ketone, 0.1 mmol; Solvent: DMSO, 2 mL (super dehydrated)

^bThe product yield was calculated as: $\text{Yield}(\%) = \frac{(\text{product 1})+(\text{product 2})\times 2}{(\text{substrate, BA})} \times 100$

Other ketones were also used as substrates in aldol condensation with BA. The low product formation could be attributed to the steric effect and the stability of β -proton on the substrate (Figure 2-12). However, these results assured the superb catalytic property of TBA-Nb₆ whose pK_a value was found to be 29.0 in this work.

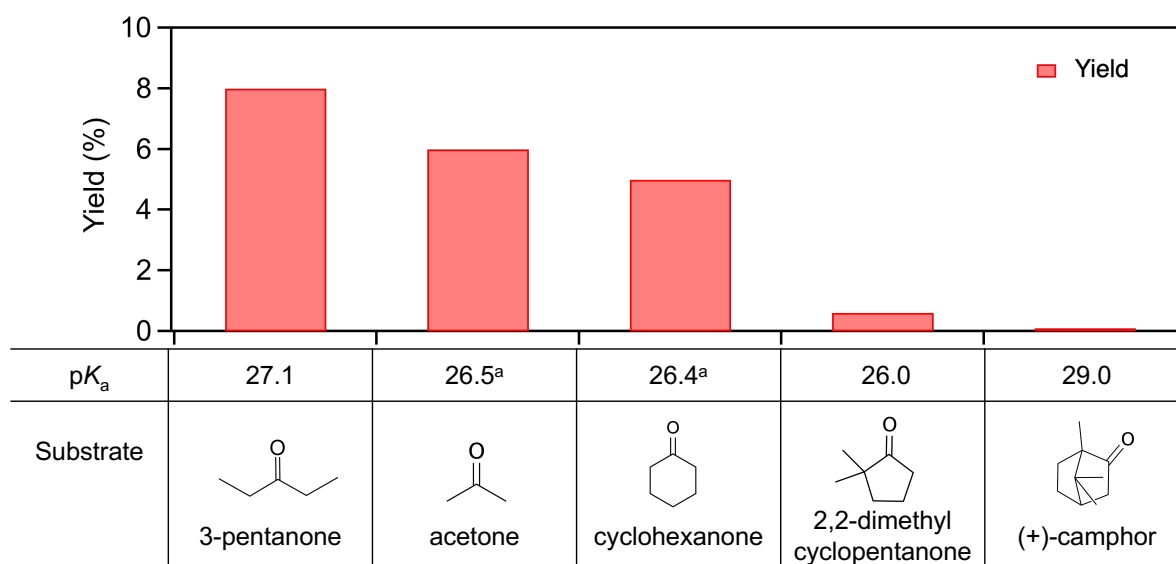


Figure 2-12. The aldol condensation result between BA and ketones with high basicity and steric hindrance. Reaction condition: substrates: BA, 0.5 mmol; ketone, 0.5 mmol; solvent: DMSO, 1 mL (super dehydrated); atmosphere: N₂ (1 atm); temperature: 30°C; reaction time: 24 h.

^aThe product yield was calculated as: $\text{Yield}(\%) = \frac{(\text{product 1})+(\text{product 2})\times 2}{(\text{substrate, BA})} \times 100$

Furthermore, the water tolerance property of TBA-Nb₆ was investigated which would be an advantage over solid base catalyst. Knoevenagel condensation reactions with an additional amount of water (45 μL, 500 molar equivalences to TBA-Nb₆) were conducted to observe the effect of the presence of water to the catalytic performance. From the results, the presence of water barely affected the catalytic activity of TBA-Nb₆ when conducting the condensation between benzaldehyde and phenylacetonitrile (pK_a = 21.9) or (4-methoxyphenyl)acetonitrile (pK_a = 23.8) (Figure 2-13). However, when conducting the reaction using MgO as the catalyst, a significant decrease in conversion was observed when water was added. This result suggested the ability to abstract proton from the substrate by TBA-Nb₆ even in the presence of excess proton from added water.

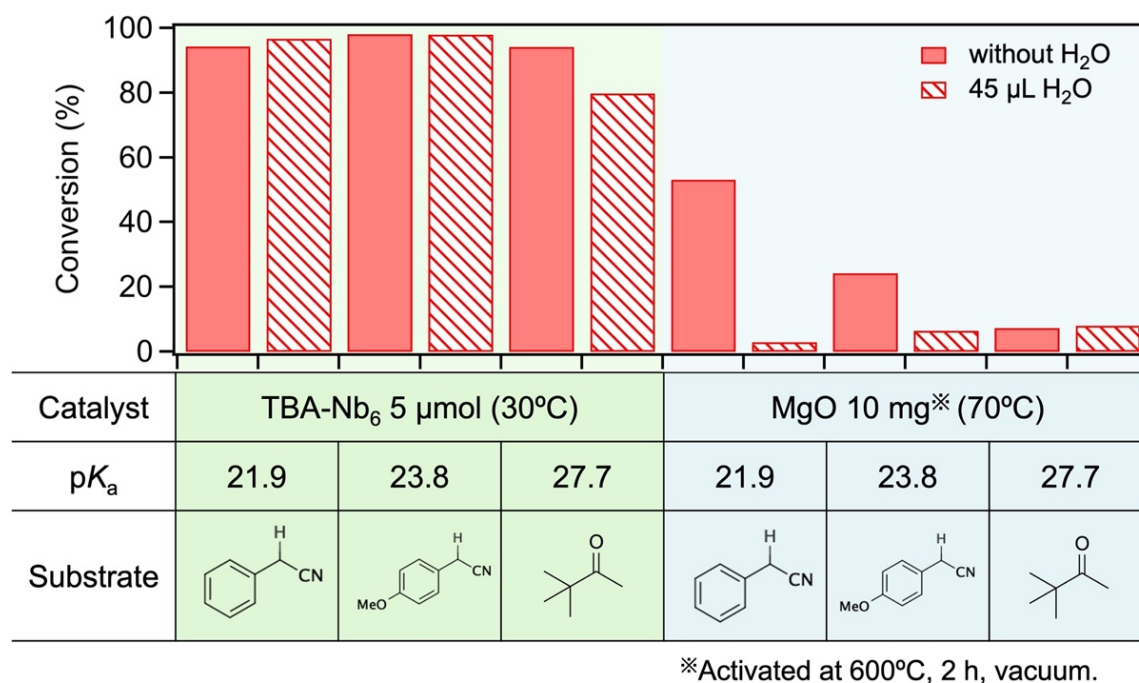
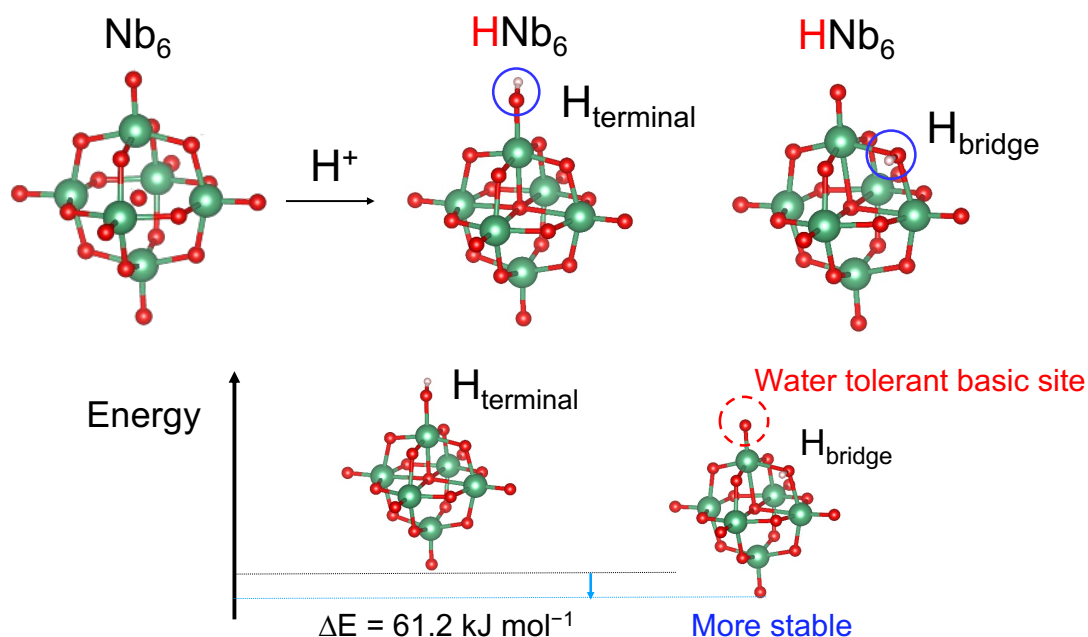


Figure 2-13. Catalytic activity (BA conversion) of Knoevenagel and aldol condensation in an absence of water (solid bar) and in the presence of 45 μL of water (patterned bar) using TBA-Nb₆ and MgO as the catalysts. Reaction condition: substrates: BA, 0.5 mmol; nitrile or ketone, 0.5 mmol; solvent: DMSO, 1 mL (super dehydrated); atmosphere: N₂ (1 atm); reaction time: 24 h.

To understand the ability for TBA-Nb₆ to withstand the presence of water without significantly affecting proton abstraction from the substrate in the condensation reaction, DFT calculation was carried out. From the calculation results, the proton abstraction by bridged O would be more stable than terminal O site, making the bridged O site being the primary site for proton abstraction. As a result, the terminal O site of [Nb₆O₁₉]⁸⁻ would be available for abstraction of proton, which would then be stabilized by transferring the proton to bridged O site,

thus making this terminal O site available and become as a so-called water tolerant basic site (Scheme 2-4).



Scheme 2-4. Illustration of the relative energy of $[\text{Nb}_6\text{O}_{19}]^{8-}$ with proton adsorption on the terminal O and on the bridged O.

The dependence of the reaction time was elucidated using optimized condition of aldol condensation of pinacolone (Figure 2-14a). The data indicated a fast kinetic with turn over frequency (TOF) of 47 h^{-1} calculated from result after 2 h of reaction, in which the plateau could be observed. Moreover, the desired product, 4,4-dimethyl-1-phenyl-pent-1-en-3-one, could also be obtained with over 93% of selectivity that maintained throughout the course of 24 h. In comparison of the catalytic performance upon an addition of water (Figure 2-14b), the final conversion of the substrate was lower than the condition in an absence of water as shown previously in Figure 2-13. However, the conversion did not immediately reached plateau from 2 h as in the case of without water addition, but rather a slight increase from 64% after 2 h to 74% after 10 h of reaction prior to reaching 80% after 24 h of reaction. This finding could be attributed to the proton abstraction of the substrate in the presence of water. The activation energy of pinacolone by $[\text{H}_2(\text{Nb}_6\text{O}_{19})]^{6-}$ from IRC calculation resulted in 76.4 kJ mol^{-1} for activation at terminal O site and a slight lower energy of 75.6 kJ mol^{-1} at bridged O site, hence any O site could activate pinacolone. The presence of excess protons from water caused a competition in the abstraction on the basic sites of TBA- Nb_6 and consequently led to lower conversion.

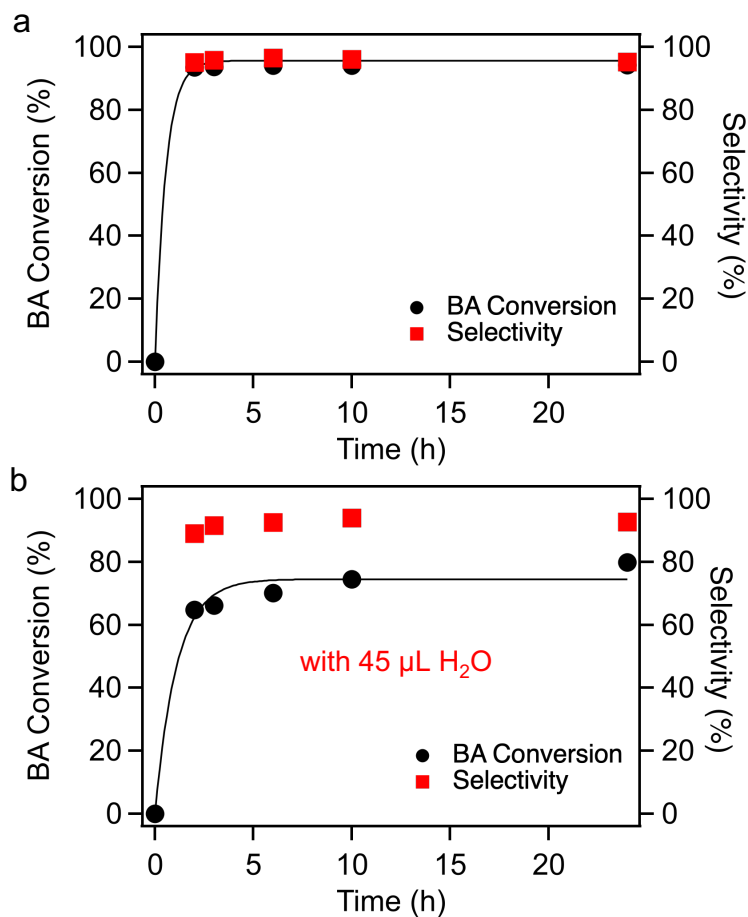


Figure 2-14. Time course reaction of aldol condensation of pinacolone promoted by TBA-Nb₆ (a) in an absence of water addition and (b) with 45 μL of water addition. Reaction condition: substrates: BA, 0.5 mmol; ketone, 0.5 mmol; solvent: DMSO, 1 mL (super dehydrated); atmosphere: N₂ (1 atm); temperature: 30°C; reaction time: 24 h.

Furthermore, the inhibition of proton abstraction ability of TBA-Nb₆ was investigated by conducting the reaction under the presence of indicators, including phenolphthalein and bromothymol blue in an excess amount. The reaction result confirmed that the catalytic activity was inhibited by the presence of indicators with less than 4% of BA conversion and less than 1% of product yield. These results were in good agreement with the decrease in catalytic performance in the presence of water, thus confirming the active sites of TBA-Nb₆ being the surface O atoms, both bridged O and terminal O sites.

2.4 Conclusions

In this chapter, the preparation of $\text{TBA}_6\text{H}_2[\text{Nb}_6\text{O}_{19}]$ (TBA-Nb₆) by microwave-assisted hydrothermal reactor provided higher yield and efficiency than conventional hydrothermal method that would result in $\text{TBA}_4\text{H}_4[\text{Nb}_6\text{O}_{19}]$ with lower basicity. The basicity of TBA-Nb₆ was elucidated by Knoevenagel and aldol condensation reactions. The results suggested not only higher catalytic activity could be achieved from TBA-Nb₆ than MgO, but the water tolerance property of TBA-Nb₆ was also revealed. The origin of water tolerance property was investigated by DFT calculation, proton adsorption on different O atoms, in other words, different basic sites of $[\text{Nb}_6\text{O}_{19}]^{8-}$ accompanied by different energy level, where adsorption at bridged O atoms would be more stable than terminal O atoms. In the case of proton abstraction by terminal O atoms, the intramolecular transfer could occur to transfer adsorbed proton to a more stable site, thus leaving a terminal O site available. This available site is therefore understood to be the water tolerant basic site that allow TBA-Nb₆ to perform proton abstraction from substrate even in the presence of excess amount of water in the system. Furthermore, the proton abstraction could be achieved for substrate with $\text{p}K_{\text{a}}$ value up to 29.0, suggesting that the ultra-high basicity of TBA-Nb₆ and could therefore be considered as superbase catalyst (Figure 2-15). This discovery was the first report on the superbase catalyst in the field of metal oxide clusters that led to an exploration of the potential catalytic application of TBA-Nb₆. TBA-Nb₆ could potentially be applied to conversion of biomass reactions to produce value-added chemicals where the important criteria for the catalyst would require high and controlled basicity with high water tolerance due to the presence of aqueous phase in the reactions.

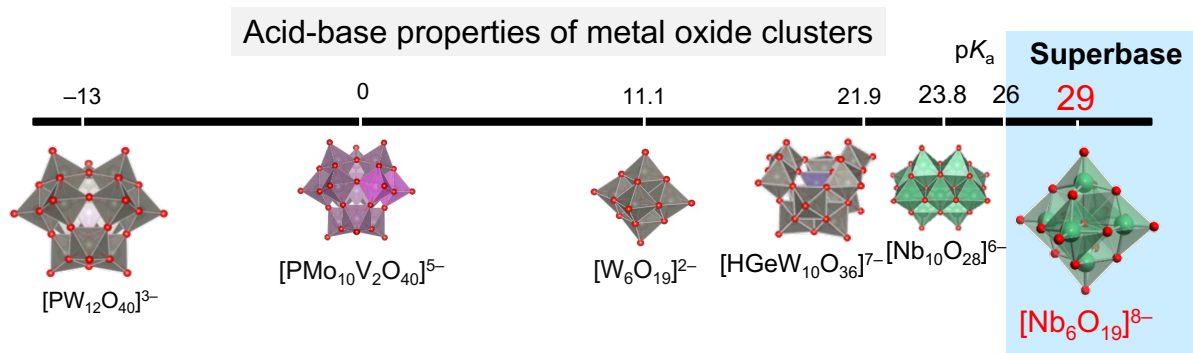


Figure 2-15. $[\text{Nb}_6\text{O}_{19}]^{8-}$ being classified as superbase catalyst with water tolerant property.

2.5 References

- (1) Schwesinger, R.; Schlemper, H. *Angew. Chem. Int. Ed. Engl.* **1987**, *26* (11), 1167–1169.
- (2) Schwesinger, R.; Hasenfratz, C.; Schlemper, H.; Walz, L.; Peters, E.-M.; Peters, K.; Von Schnering, H. G. *Angew. Chem. Int. Ed. Engl.* **1993**, *32* (9), 1361–1363.
- (3) Vazdar, K.; Margetić, D.; Kovačević, B.; Sundermeyer, J.; Leito, I.; Jahn, U. *Acc. Chem. Res.* **2021**, *54* (15), 3108–3123.
- (4) Kuwano, S.; Suzuki, T.; Hosaka, Y.; Arai, T. *Chem. Commun.* **2018**, *54* (31), 3847–3850.
- (5) Hashimoto, T.; Maruoka, K. *Chem. Rev.* **2007**, *107* (12), 5656–5682.
- (6) Cota, I.; Chimentao, R.; Sueiras, J.; Medina, F. *Catal. Commun.* **2008**, *9* (11–12), 2090–2094.
- (7) Matsuhashi, H.; Oikawa, M.; Arata, K. *Langmuir* **2000**, *16* (21), 8201–8205.
- (8) Sun, L. B.; Yang, J.; Kou, J. H.; Gu, F. N.; Chun, Y.; Wang, Y.; Zhu, J. H.; Zou, Z. G. *Angew. Chem. Int. Ed.* **2008**, *47* (18), 3418–3421.
- (9) Matsuhashi, H.; Fujita, T. *Catal. Today* **2011**, *164* (1), 131–134.
- (10) Sudarsanam, P.; Li, H.; Sagar, T. V. *ACS Catal.* **2020**, *10* (16), 9555–9584.
- (11) Shimizu, K.; Satsuma, A. *Energy Environ. Sci.* **2011**, *4* (9), 3140.
- (12) Mellmer, M. A.; Sener, C.; Gallo, J. M. R.; Luterbacher, J. S.; Alonso, D. M.; Dumesic, J. A. *Angew. Chem. Int. Ed.* **2014**, *53* (44), 11872–11875.
- (13) He, J.; Qiang, Q.; Liu, S.; Song, K.; Zhou, X.; Guo, J.; Zhang, B.; Li, C. *Fuel* **2021**, *306*, 121765.
- (14) Zang, H.; Wang, K.; Zhang, M.; Xie, R.; Wang, L.; Chen, E. Y.-X. *Catal. Sci. Technol.* **2018**, *8* (7), 1777–1798.
- (15) Rojas-Buzo, S.; García-García, P.; Corma, A. *Green Chem.* **2018**, *20* (13), 3081–3091.
- (16) Ebitani, K.; Motokura, K.; Mori, K.; Mizugaki, T.; Kaneda, K. *J. Org. Chem.* **2006**, *71* (15), 5440–5447.
- (17) Wang, Z.; Fongarland, P.; Lu, G.; Essayem, N. *J. Catal.* **2014**, *318*, 108–118.
- (18) Teixeira, A.; Morais, A.; Silva, I.; Breynaert, E.; Mustafa, D. *Crystals* **2019**, *9* (3), 153.
- (19) Sugahara, K.; Kimura, T.; Kamata, K.; Yamaguchi, K.; Mizuno, N. *Chem. Commun.* **2012**, *48* (67), 8422.
- (20) Sugahara, K.; Satake, N.; Kamata, K.; Nakajima, T.; Mizuno, N. *Angew. Chem. Int. Ed.* **2014**, *53* (48), 13248–13252.
- (21) Ge, W.; Wang, X.; Zhang, L.; Du, L.; Zhou, Y.; Wang, J. *Catal. Sci. Technol.* **2016**, *6* (2), 460–467.
- (22) Weng, Z.; Ogiwara, N.; Kitao, T.; Kikukawa, Y.; Gao, Y.; Yan, L.; Uchida, S. *Nanoscale* **2021**, *13* (44), 18451–18457.
- (23) Weng, Z.; Ogiwara, N.; Yokogawa, D.; Kitao, T.; Kikukawa, Y.; Uchida, S. *Dalton Trans.* **2022**, *51* (21), 8186–8191.
- (24) Hayashi, S.; Sasaki, N.; Yamazoe, S.; Tsukuda, T. *J. Phys. Chem. C* **2018**, *122* (51), 29398–29404.
- (25) Hayashi, S.; Yamazoe, S.; Koyasu, K.; Tsukuda, T. *Chem. – Asian J.* **2017**, *12* (13), 1635–1640.
- (26) Hayashi, S.; Yamazoe, S.; Tsukuda, T. *J. Phys. Chem. C* **2020**, *124* (20), 10975–10980.
- (27) Fukada, M.; Shibata, K.; Imai, T.; Yamazoe, S.; Hosokawa, S.; Wada, T. *J. Ceram. Soc. Jpn.* **2013**, *121* (1409), 116–119.
- (28) Rambaran, M. A.; Pascual-Borràs, M.; Ohlin, C. A. *Eur. J. Inorg. Chem.* **2019**, *2019* (35), 3913–3918.
- (29) Momma, K.; Izumi, F. *J. Appl. Crystallogr.* **2011**, *44* (6), 1272–1276.

2.6 Appendix

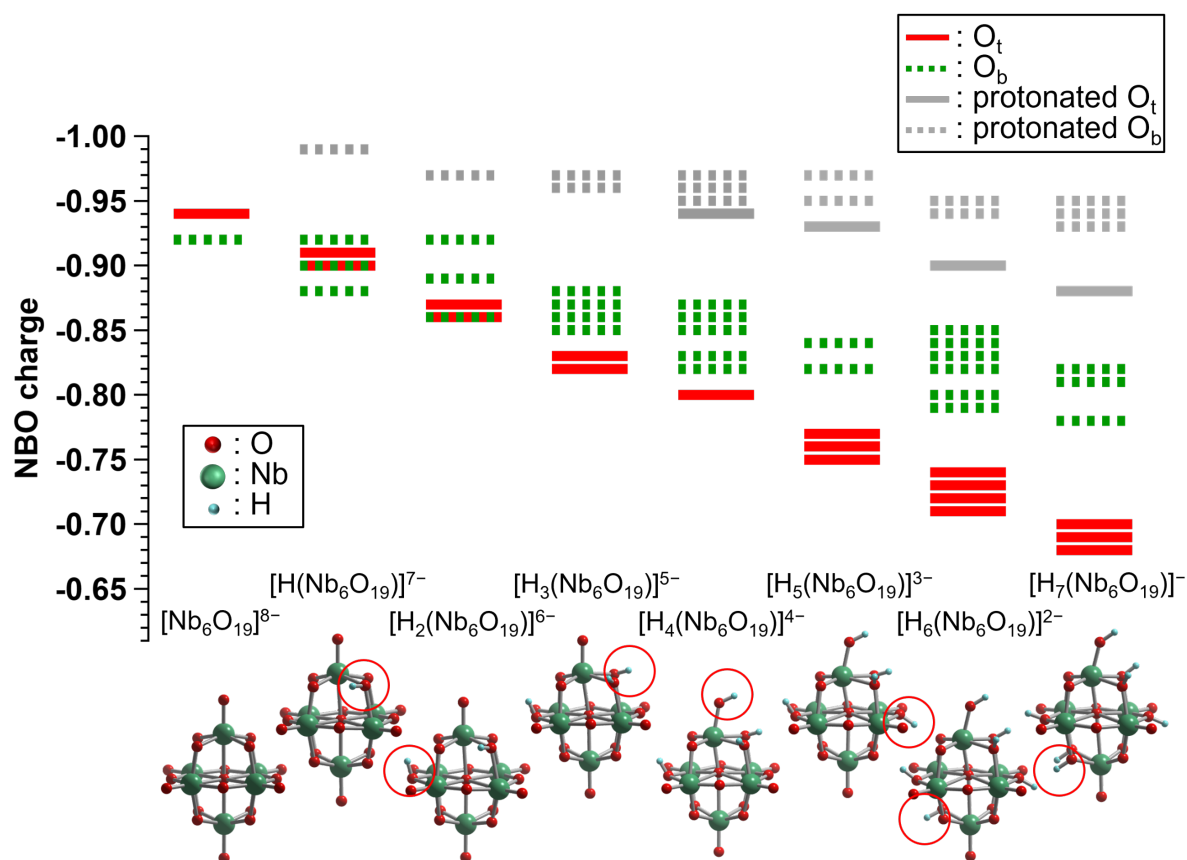


Figure S2-1. NBO charges of protonated $[\text{Nb}_6\text{O}_{19}]^{8-}$ as a function of number of protons, where O_t refers to terminal O atom and O_b refers to bridging O atoms.

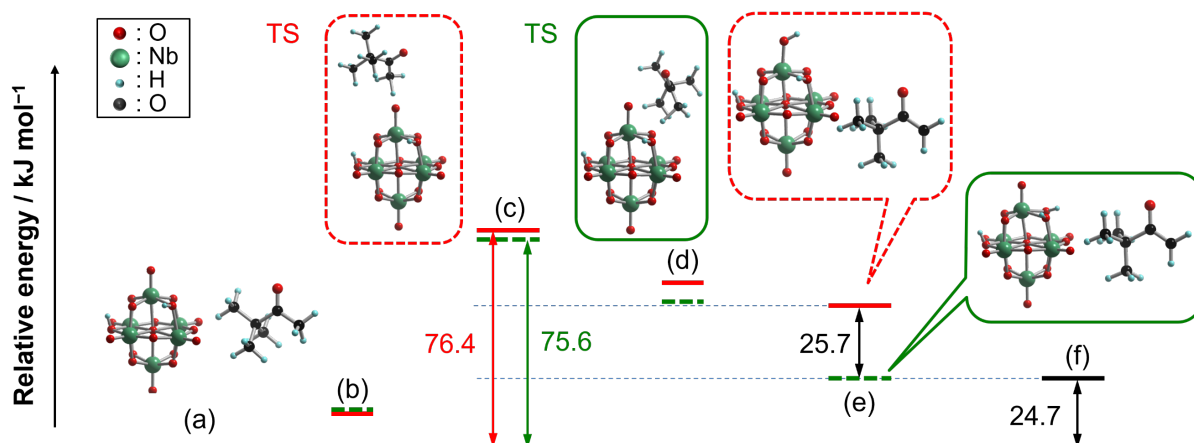


Figure S2-2. Reaction diagram for proton abstraction by $[\text{H}_2(\text{Nb}_6\text{O}_{19})]^{6-}$ from pinacolone. (a) $[\text{H}_2(\text{Nb}_6\text{O}_{19})]^{6-}$ and pinacolone as reactants, (b) back forward termination of IRC calculation, (c) optimized transition state, (d) forward termination of IRC calculation, (e) metastable state after proton abstraction, and (f) $[\text{H}_2\text{O}_b\text{H}_2(\text{Nb}_6\text{O}_{19})]^{5-}$ and β -proton-abstracted pinacolone as products. Color codes: red sphere, O; green sphere, Nb; gray sphere, C; light blue sphere, H.

Chapter 3. Lewis basicity of metal oxide clusters

3.1. Introduction

The impact of emitted CO₂ that contributed to accumulation of greenhouse gases and global warming effect led to research to reduce the amount of emitted CO₂.^{1,2} One of the useful ways to reduce CO₂ is employing it as a carbonyl source to the production of value-added chemicals. Several reactions have been discovered and summarized in Figure 3-1.³ The challenge of CO₂ utilization is the activation of CO₂, which is highly stable, to react with reactant as a nucleophilic species. The CO₂ utilization reactions also need to be conducted at mild conditions otherwise it would result in excessive consumption of energy and potentially high emission of CO₂ that contradict the purpose. Currently, only few reactions could be implemented and performed in an industrial scale, such as conversion of epoxides to polycarbonates or cyclic carbonates,⁴⁻⁶ which are useful in production of engineering plastics and numerous organic syntheses.⁷⁻²¹

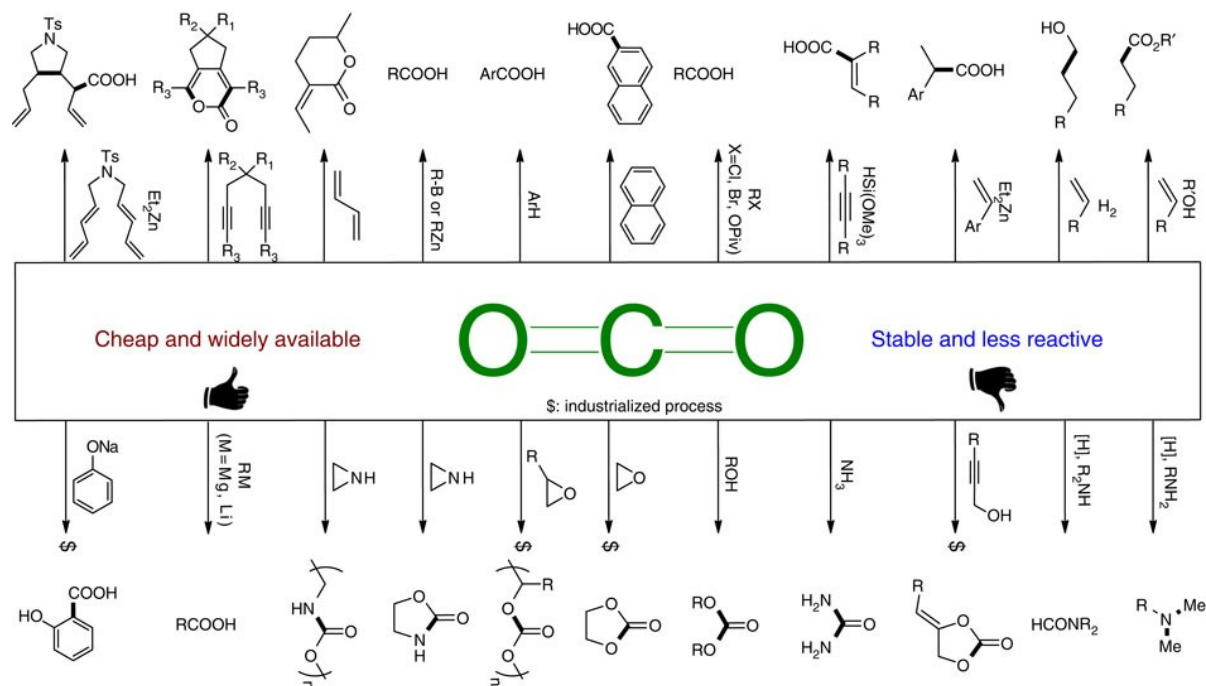


Figure 3-1. Discovered reactions using CO₂ as a carbonyl source.³

The basicity of Lindqvist-type metal oxide clusters with group 5 metals ($[\text{M}_6\text{O}_{19}]$, M = Ta, Nb) were found to be active for CO₂ activation and promoted the CO₂ fixation to epoxide to form carbonate derivative effectively. On the other hand, group 6 hexametalates, $[\text{W}_6\text{O}_{19}]^{2-}$ and $[\text{Mo}_6\text{O}_{19}]^{2-}$, do not possess sufficient basicity to activate CO₂ and therefore the catalytic activity could not be observed (Figure 3-2).²²

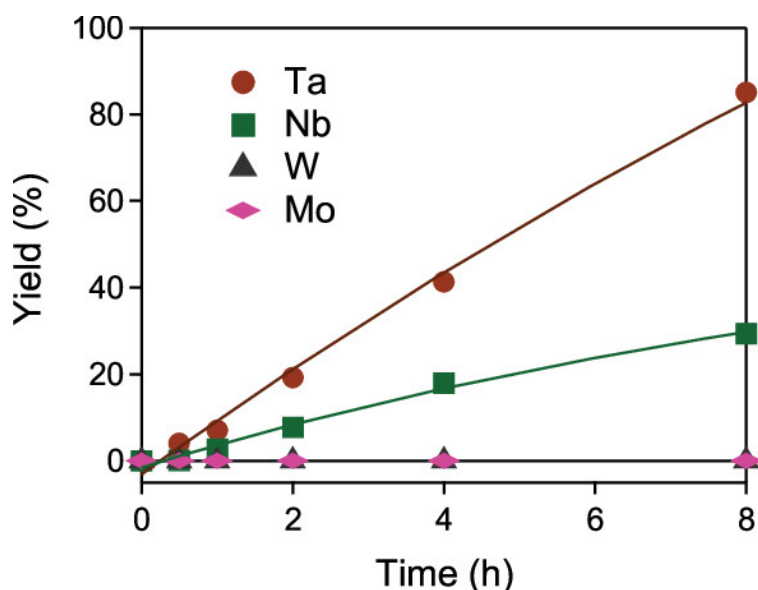


Figure 3-2. Results of CO₂ fixation to styrene oxide (SO) using tetrabutylammonium (TBA) salts of Lindqvist-type [M₆O₁₉] (M = Ta, Nb, W, Mo) as the catalysts. Reaction condition: substrate: SO, 2.2 mmol; catalyst, 5 μmol; solvent: DMSO, 0.25 mL; atmosphere: CO₂ (0.1 MPa); reaction temperature, 130°C.²²

The utilization of tetrabutylammonium (TBA) salt of [Ta₆O₁₉]⁸⁻ as the catalyst to promote CO₂ fixation to styrene oxide (SO) to give styrene carbonate (SC) as the product. The result after 24 h of reaction at 130°C using atmospheric pressure of 100% CO₂ provided 95% conversion of SO and 83% of selectivity to SC.²² These data showed high conversion of the substrate could be achieved, while the selectivity to the desired product was limited.

In our research group, CO₂ fixation reaction has been experimented with a slightly milder condition to compare the catalytic performance and product selectivity using TBA salt of [Nb₆O₁₉]⁸⁻ as the catalyst comparing to TBA salt of [Ta₆O₁₉]⁸⁻. When using TBA salt of [Nb₆O₁₉]⁸⁻ as the catalyst, low SO conversion was obtained, however, high selectivity to SC could be achieved. These results suggested that mechanism between the basic site of Ta and Nb toward CO₂ fixation could be different. If the activity provided by Ta and Nb is different, it is hypothesized that the mixture between Ta and Nb in the cluster could result in an improved catalytic performance and find the balance between substrate conversion and product selectivity. Moreover, our group reported the different local symmetry between NbO₆ and TaO₆ units in the sodium salts of [Ta_xNb_{6-x}O₁₉]⁸⁻ (x = 0, 2–4, 6) affected the Brønsted basicity of the clusters in Knoevenagel condensation reaction (Figure 3-3).⁴

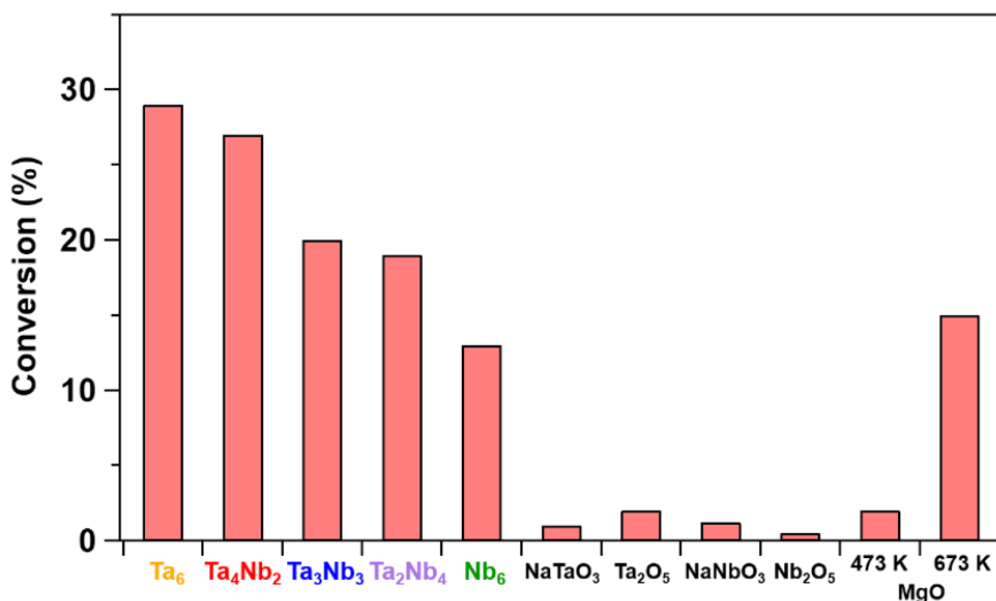


Figure 3-3. Results of Knoevenagel condensation by $\text{Na}[\text{Ta}_x\text{Nb}_{6-x}\text{O}_{19}]^{8-4}$. Reaction conditions: substrates: benzaldehyde, 1 mmol; phenylacetonitrile, 1 mmol; catalyst loading, 5 μmol for $\text{Na}[\text{Ta}_x\text{Nb}_{6-x}\text{O}_{19}]^{8-}$ or 5 mg for other metal oxides; solvent, dimethyl sulfoxide (2 mL); atmosphere, N_2 (0.1 MPa); reaction temperature, 30°C; reaction time, 24 h.

The difference in catalytic performance observed as a result of varying Ta and Nb composition in the clusters could be explained by theoretical calculation. Natural bond order (NBO) charges of O atoms of each type of cluster were investigated. The red marks in the charts represent average NBO charges of the clusters (Figure 3-4). The higher negativity the NBO charge means the higher basicity the clusters possess.^{22,23} As a result, higher Ta content in the mixed Ta-Nb clusters resulted in overall higher basicity of the clusters which consequently provided higher catalytic performance in Knoevenagel condensation reaction.

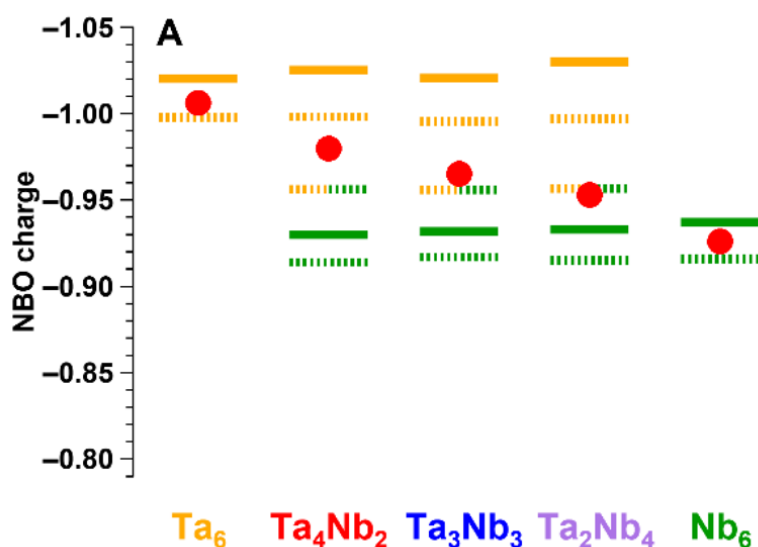


Figure 3-4. Average NBO charges on O atoms of free $[\text{Ta}_x\text{Nb}_{6-x}\text{O}_{19}]^{8-}$ ($x = 0, 2-4, 6$) indicated by red marks, solid lines refer to NBO charges on terminal O atoms and dashed lines refer to NBO charges on bridged O atoms. Orange lines correspond to the O atoms coordinated to Ta and green lines correspond to the O atoms coordinated to Nb.

Chapter 3

From these findings, CO₂ fixation using TBA salts of mixed [Ta_xNb_{6-x}O₁₉]⁸⁻ as catalysts could result in a similar trend in terms of Lewis basicity and conversion of the substrate. However, the effect of Ta and Nb composition to the selectivity of **SC** was not yet understood. The hypothesis was that the mixed Ta-Nb clusters would provide **SC** selectivity between TBA-Nb₆ and TBA-Ta₆. Therefore, in this chapter, a series of TBA salts of [Ta_xNb_{6-x}O₁₉]⁸⁻ ($x = 0-6$) was prepared and employed as the catalysts for CO₂ fixation to **SO** to elucidate the effect of Ta and Nb composition to the selectivity of **SC**.

3.2 Experimental

Ta₂O₅ and Nb₂O₅ were purchased from Kojundo Chemical Laboratory Co., Ltd., K₈Nb₆O₁₉·*n*H₂O was purchased from Mitsuwa Chemicals Co., Ltd., dimethyl sulfoxide (DMSO, super dehydrated), hydrochloric acid, and Na₂C₂O₄ were purchased from Fujifilm Wako Pure Chemical Corp. Ltd., was purchased from, 40% tetrabutylammonium hydroxide (TBAOH) aqueous solution, and styrene oxide were purchased from Tokyo Chemical Industry Co., Ltd. Hexane, biphenyl, deuterated DMSO (DMSO-d₆), and (NH₂)₂CO were purchased from Kanto Chemical Co., Inc. All reagents were used as received.

Density functional theory (DFT) calculations and natural bonding orbital (NBO) analysis of [Ta_{*x*}Nb_{6-*x*}O₁₉]⁸⁻ were performed by using the Gaussian 16 program, in accordance with the literature.²² The optimized structures of the [Nb₆O₁₉]⁸⁻ were calculated by B3LYP incorporating the solvation effect of DMSO using PCM (dielectric constant = 46.826) using LANL2DZ basis sets for Nb atoms, and 6-31++G(d,p) basis sets for O, C and H atoms.

3.2.1 Synthesis of NaTa_{*x*}/6Nb_{(6-*x*)/6O₃}

NaTa_{*x*}/6Nb_{(6-*x*)/6O₃ (*x* = 0–6) were prepared by modified solid-state method by grinding the mixture of Ta₂O₅ and Nb₂O₅ with Na₂C₂O₄ and (NH₂)₂CO with molar ratio of 1:1:4 for 10 minutes using alumina agate and mortar.^{24,25} The mixtures were calcined in alumina crucible at 600°C for 4 h at the heating rate of 2.5°C/min. After the first calcination, each mixture was ground with additional (NH₂)₂CO with the same amount used in the first calcination prior to calcination again at 600°C for 4 h to remove impurities. The structures and purity of the products were confirmed by X-ray diffraction (XRD).}

3.2.2 Synthesis of Na₃Ta_{*x*}/6Nb_{(6-*x*)/6O₄}

Each composition of NaTa_{*x*}/6Nb_{(6-*x*)/6O₃ was ground with Na₂C₂O₄ and (NH₂)₂CO with molar ratio of 1:1:3 followed by calcination at 900°C for 4 h with the same heating rate of 2.5°C/min to obtain Na₃Ta_{*x*}/6Nb_{(6-*x*)/6O₄. The structures and purity of the products were confirmed by XRD.}}

3.2.3 Synthesis of (Ta_{*x*}Nb_{6-*x*})₂O₅·*n*H₂O

The obtained Na₃Ta_{*x*}/6Nb_{(6-*x*)/6O₄ was washed with water (15 mL) twice and followed by extraction with water (45 mL) to obtain solution of Na₈[Ta_{*x*}Nb_{6-*x*}O₁₉]. The acidification of Na₈[Ta_{*x*}Nb_{6-*x*}O₁₉] by 1 M HCl would result in (Ta_{*x*}Nb_{6-*x*})₂O₅·*n*H₂O as precipitate. The}

precipitate was washed with pure water until the pH of the supernatant became neutral. After washing, it was dried under vacuum for 2 h prior to drying in oven at 60°C overnight.

3.2.4 Synthesis of $TBA_6H_2[Ta_xNb_{6-x}O_{19}]$ (TBA- Ta_xNb_{6-x})

The obtained $(Ta_xNb_{6-x})_2O_5 \cdot nH_2O$ was reacted with tetrabutylammonium hydroxide (TBAOH) aqueous solution (10%) using microwave-assisted hydrothermal reactor at 180°C for 15 minutes (Initiator+ Biotage, Ltd.).²⁶ The obtained clear, colorless solution was filtered using syringe filter (polyethersulfone, PES, 0.22 μm) to remove any unreacted precursors. The filtrate was lyophilized and washed with hexane, this step was repeated for three times to remove tributylamine that came from decomposition of TBAOH during lyophilization. The obtained $TBA_6H_2[Ta_xNb_{6-x}O_{19}]$ (TBA- Ta_xNb_{6-x}) was characterized by Fourier-transform infrared spectrometer (JASCO, FT/IR-4600) equipped with attenuated total reflection accessory (JASCO, ATR PRO ONE), electrospray ionization-mass spectrometry (ESI-MS) in negative ion mode with 1 M aqueous solution (microTOF-II, Bruker), CHN elemental analysis (UNICUBE, Elementar Japan Co., Ltd.), and X-ray absorption fine structure (XAFS, BL01B1, BL14B2, BL36XU SPring-8). The amount of TBA cation was determined by:

$$TBA \text{ unit} = \frac{Mass_{CHN}}{Mass_{TBA}}$$

where $Mass_{CHN}$ refers to the total content of C, H, and N determined by elemental analysis and $Mass_{TBA}$ is molecular weight of TBA ($C_{16}H_{36}N = 242.78 \text{ g mol}^{-1}$). The excess H units would be determined as counter cation.

3.2.2 General procedure for CO_2 fixation reaction

CO_2 fixation reaction to styrene oxide (**SO**) to form styrene carbonate (**SC**) was conducted in a batch-type reactor. In a typical reaction, 5 mmol of **SO** in the presence of 5 μmol of TBA- Ta_xNb_{6-x} in neat condition under 0.1 MPa of 100% CO_2 at 100°C for 6 h. The reaction solution was analyzed using gas chromatography equipped with flame ionization detector (GC-FID, Shimadzu, GC-2014 with column Restex, Rtx-1) and gas chromatography-mass spectrometry (GC-MS, Shimadzu, GCMS-QP2010 SE with column Agilent, DB-1MS) using biphenyl as an internal standard.

3.2.3 Calculation of product yield:

$$Conversion(\%) = \left(1 - \frac{Area_{Sub.}}{Area_{IS}} \times \frac{Area_{IS,0}}{Area_{Sub,0}} \right) \times 100$$

$$Yield(\%) = \frac{Area_{Pro.}}{Area_{IS}} \times \frac{ECN_{Sub.}}{ECN_{Pro.}} \times \frac{Area_{IS,0}}{Area_{Sub.,0}} \times 100$$

where, *Sub.*, substrate (**SO**); *IS*, internal standard (biphenyl); *Pro.*, product; *ECN* = effective carbon number. subscripted 0 means the peak area reaction solution without catalyst.

Calculation of turn over number (TON) and turn over frequency (TOF):

$$TON = \frac{Moles\ of\ product}{Moles\ of\ catalyst}$$

$$TOF = \frac{TON}{Time}$$

3.2.4 Illustration of catalysts

The obtained crystallographic data were used to visualize the structure of catalysts using VESTA program.²⁷

3.3 Results and discussion

3.3.1 Synthesis of $\text{NaTa}_x\text{Nb}_{(6-x)/6}\text{O}_3$

A series of $\text{NaTa}_x\text{Nb}_{(6-x)/6}\text{O}_3$ ($x = 0-6$) was prepared by modified solid-state reaction using Ta_2O_5 , Nb_2O_5 , $\text{Na}_2\text{C}_2\text{O}_4$, and $(\text{NH}_2)_2\text{CO}$ as the precursors. The obtained products were characterized by XRD (Figures 3-5).

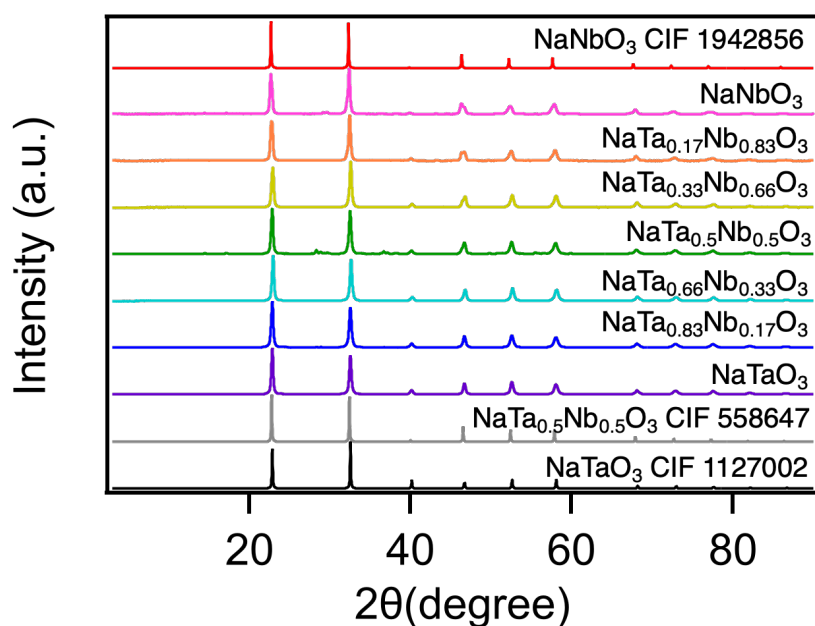


Figure 3-5. XRD patterns of $\text{NaTa}_x\text{Nb}_{(6-x)/6}\text{O}_3$ compared to the references (CIF numbers 1942856 and 1127002).

3.3.2 Synthesis of $\text{Na}_3\text{Ta}_x\text{Nb}_{(6-x)/6}\text{O}_4$

The prepared $\text{NaTa}_x\text{Nb}_{(6-x)/6}\text{O}_3$ samples were ground with $\text{Na}_2\text{C}_2\text{O}_4$ and $(\text{NH}_2)_2\text{CO}$ with molar ratio of 1:1:3 for 10 minutes using alumina agate and mortar. The ground mixtures were calcined at 900°C for 4 h with the same heating rate of $2.5^\circ\text{C}/\text{min}$ to obtain $\text{Na}_3\text{Ta}_x\text{Nb}_{(6-x)/6}\text{O}_4$. The obtained products were characterized by XRD (Figures 3-6).

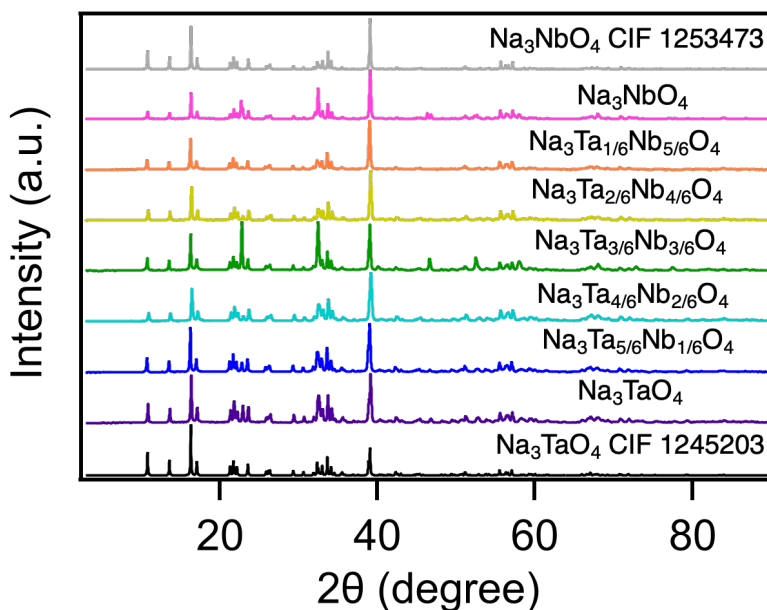


Figure 3-6. XRD patterns of $\text{Na}_3\text{Ta}_x\text{Nb}_{(6-x)/6}\text{O}_4$ along with the references (CIF numbers 1253473 and 1245203).

3.3.3 Synthesis of $\text{TBA}_6\text{H}_2[\text{Ta}_x\text{Nb}_{6-x}\text{O}_{19}]$ ($\text{TBA-Ta}_x\text{Nb}_{6-x}$)

After obtaining the $\text{Na}_3\text{Ta}_x\text{Nb}_{(6-x)/6}\text{O}_4$ products, they were used to prepare $(\text{Ta}_x\text{Nb}_{6-x})_2\text{O}_5 \cdot n\text{H}_2\text{O}$ for synthesis of $\text{TBA}_6\text{H}_2[\text{Ta}_x\text{Nb}_{6-x}\text{O}_{19}]$ ($\text{TBA-Ta}_x\text{Nb}_{6-x}$) using microwave-assisted hydrothermal reactor. The utilization of microwave-assisted hydrothermal reactor to provide high efficiency of the synthesis. In addition, it was found that deterioration of $\text{TBA-Ta}_x\text{Nb}_{6-x}$ could occur due to exposure to CO_2 and water in air that affected the basicity and catalytic activity, therefore, the preparation steps were carried out under N_2 atmosphere as much as possible. The compositions of the synthesized $\text{TBA-Ta}_x\text{Nb}_{6-x}$ were analyzed by ESI-MS with corresponding desired composition where TBA units ranged from 2–4, as shown in Figure 3-7.

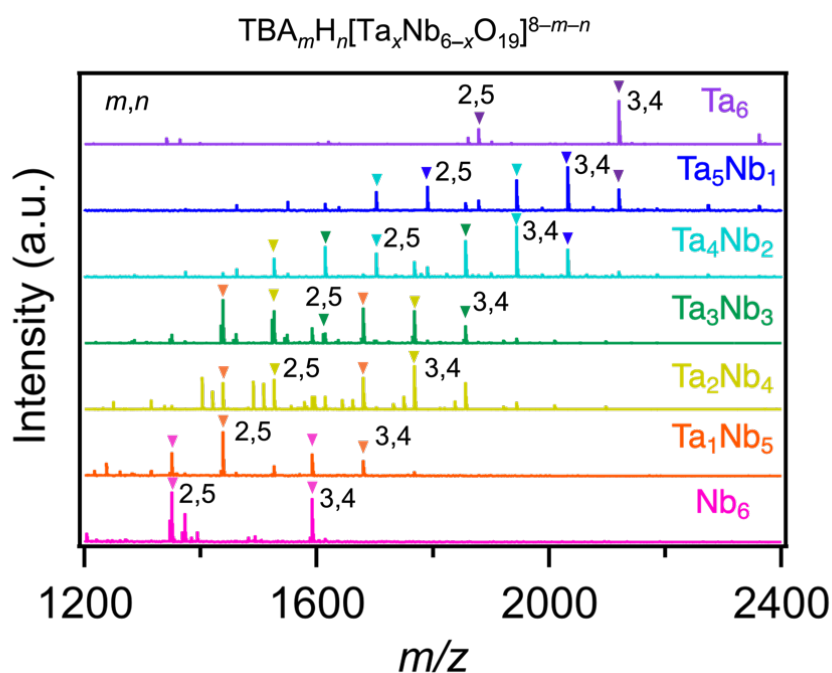


Figure 3-7. ESI-MS spectrum of the aqueous solution of $\text{TBA}_m\text{H}_n[\text{Ta}_x\text{Nb}_{6-x}\text{O}_{19}]^{8-m-n}$ measured in negative ion mode.

The vibration corresponding to terminal $\text{Nb}=\text{O}_t$ bonding and bridging $\text{Nb}-\text{O}_b-\text{Nb}$ were assigned in the shaded region in the FT-IR spectra (Figure 3-8). These vibrations correspond to the Lindqvist-type structure of $[\text{M}_6\text{O}_{19}]$.

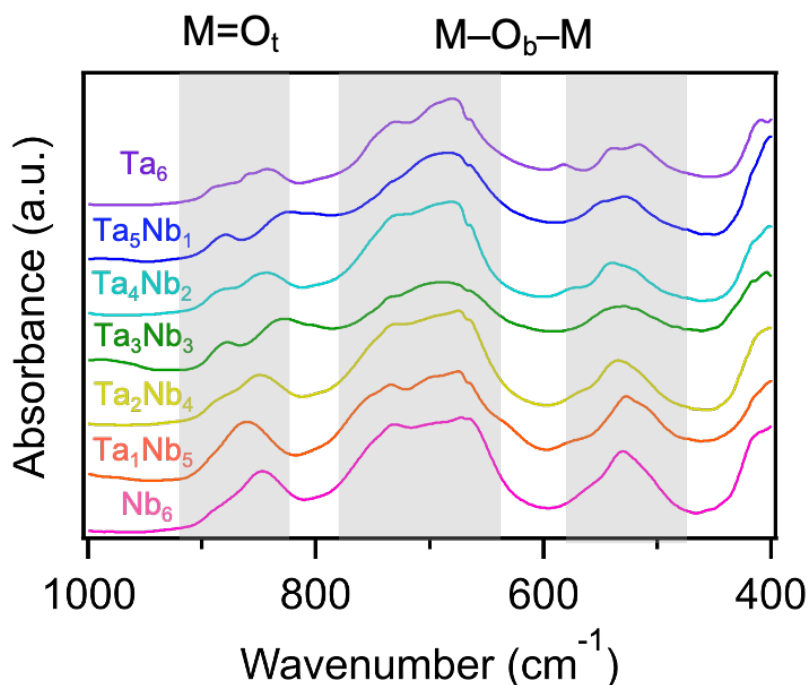


Figure 3-8. The FT-IR spectra of $\text{TBA}-\text{Ta}_x\text{Nb}_{6-x}$ measured in ATR mode.

Elemental analysis was used to analyze the amount of TBA cation and proton of the clusters, which were calculated to be 5–6 TBA units and 2–3 protons as the counter cations.

The amount of Ta and Nb was estimated from X-ray absorption spectroscopy (XAS) confirming the desired composition of the synthesized TBA-Ta_xNb_{6-x} (Table 3-1).

Table 3-1. Elemental analysis data of TBA-Ta_xNb_{6-x}.

	C ^a (%)	H ^a (%)	N ^a (%)	TBA amount	H amount	Ta ^b (%)	Nb ^b (%)	Ta/Nb ratio
TBA-Nb ₆	45.29	9.42	3.43	6.0	2.0	–	27	–
TBA-Ta ₁ Nb ₅	39.19	8.62	2.98	5.0	3.0	9.4	24	1.0/5.0
TBA-Ta ₂ Nb ₄	39.86	8.9	3.01	5.3	2.7	17	17	2.0/4.0
TBA-Ta ₃ Nb ₃	44.38	9.1	3.44	6.1	1.9	20	11	2.9/3.1
TBA-Ta ₄ Nb ₂	37.24	8.5	2.83	5.3	2.7	31	7.9	4.0/2.0
TBA-Ta ₅ Nb ₁	38.81	8.26	2.91	5.7	2.3	35	3.2	5.1/0.9
TBA-Ta ₆	37.05	7.75	2.7	5.7	2.3	41	–	–

^aDetermined by elemental analysis.

^bEstimated by X-ray absorption.

Fourier-transformed extended X-ray absorption fine structure (FT-EXAFS) of TBA-Ta_xNb_{6-x} revealed peaks of Ta–M (M = Ta, Nb) shifted toward longer bond length with higher Ta content (Figure 3-9). The similar trend was also observed in Nb K-edge with longer Nb–M bonds. These results indicated the effect of substitution of Ta to Nb sites of [Nb₆O₁₉]⁸⁻.

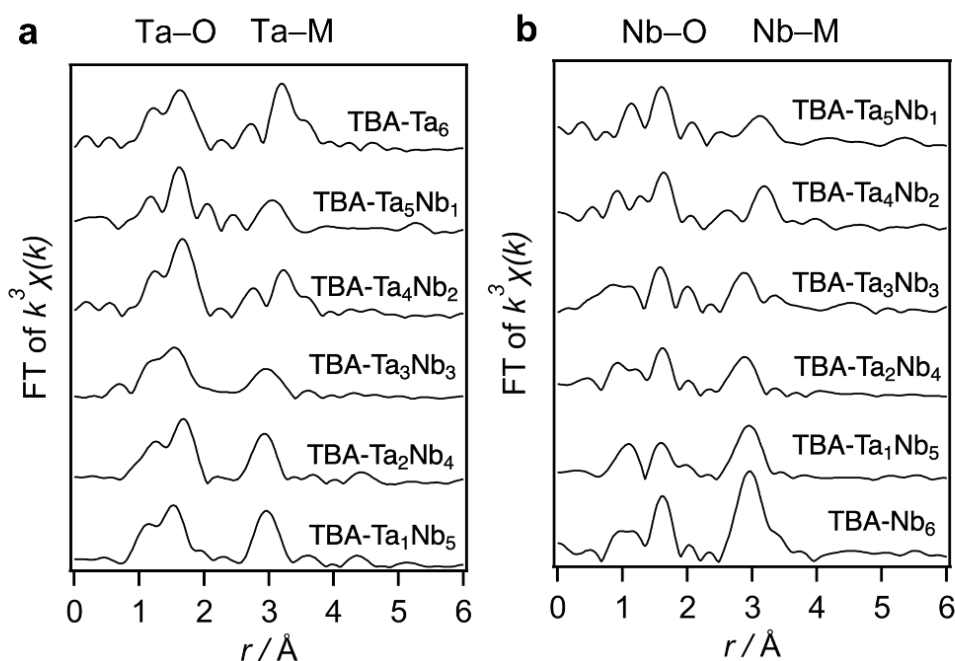


Figure 3-9. FT-EXAFS of (a) Ta L₃-edge and (b) Nb K-edge of TBA-Ta_xNb_{6-x}. Measurement conditions: crystal Si(311), mirror: 1.5 mrad, gas composition: I₀; N₂ = 50% Ar 50%, I₁; Ar = 75% Kr 25%. The k³-weighted EXAFS oscillation in the range of 3–16 Å⁻¹ was Fourier transformed. The data reduction was performed using xTunes software.²⁸

After confirming the purity of the synthesized TBA-Ta_xNb_{6-x}, they were employed as the catalysts for the CO₂ fixation reaction to **SO** to form **SC**. First, the catalytic reaction results were compared between TBA-Nb₆ and TBA-Ta₆ as shown in Figure 3-10. When conducting the reaction using TBA-Nb₆, the conversion of **SO** was low, however the selectivity to **SC** was high. On the other hand, TBA-Ta₆ provided high conversion, while the selectivity to **SC** was limited. These results indicated the characteristic functions of the two pristine catalysts. These data led to a further investigation using TBA-Ta_xNb_{6-x} as the catalysts.

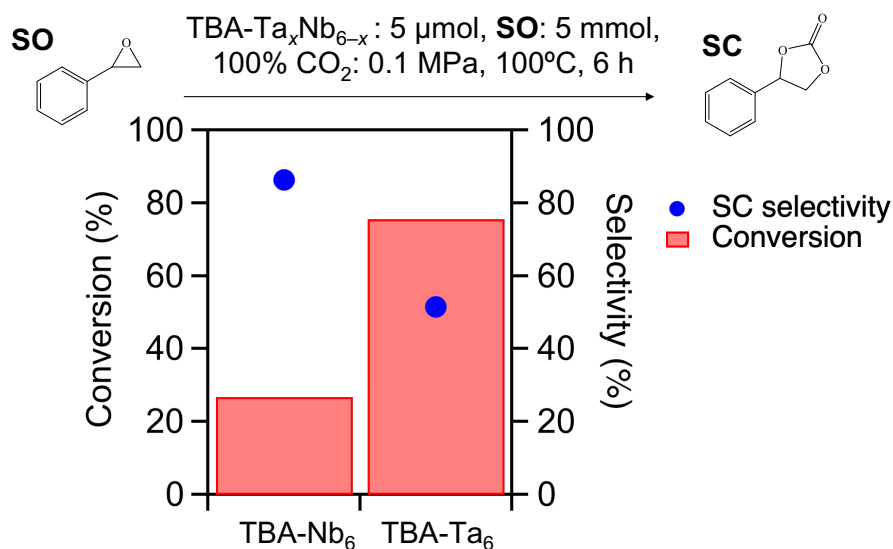


Figure 3-10. The result of CO₂ fixation to **SO** using TBA-Nb₆ and TBA-Ta₆ as the catalysts. Reaction condition: substrate, **SO** (5 mmol); catalyst loading, 5 μmol; atmosphere, 100% CO₂ (0.1 MPa); reaction temperature, 100°C; reaction time: 6 h.

In the reactions promoted by TBA-Ta_xNb_{6-x}, the results showed a trend of increasing **SO** conversion with higher Ta content, which corresponded to the higher overall basicity of the clusters (Figure 3-11). However, the highest **SC** selectivity was achieved when using TBA-Ta₁Nb₅ as the catalyst. When prolonging the reaction from 6 h to 24 h, high **SO** conversion could be obtained while maintaining high **SC** selectivity.

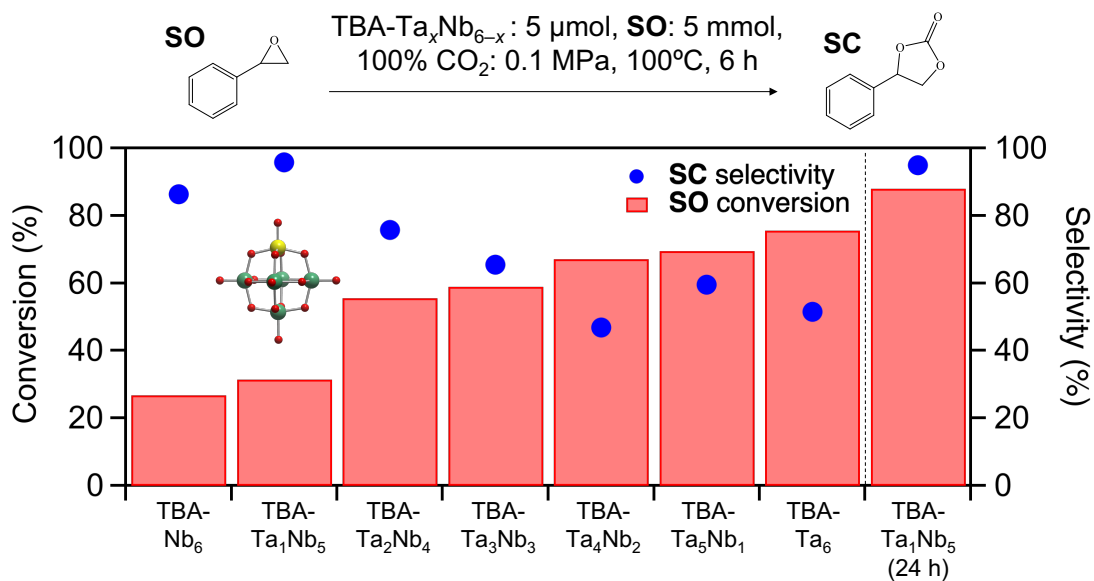


Figure 3-11. Catalytic activity of CO₂ fixation to **SO** using TBA-Ta_xNb_{6-x} as catalysts. Reaction condition: substrate: **SO**, 5 mmol; catalyst loading, 5 μmol; atmosphere, 100% CO₂ (0.1 MPa); reaction temperature, 100°C; reaction time, 6 h.

After prolonged the reaction to 24 h, all TBA-Ta_xNb_{6-x} clusters showed conversion of **SO** over 80% (Figure 3-12). In the case of reactions promoted by TBA-Ta_xNb_{6-x} ($x = 1-5$), over 90% of **SC** selectivity could be achieved. TBA-Ta₆ resulted in significantly lower selectivity than other catalysts (62%).

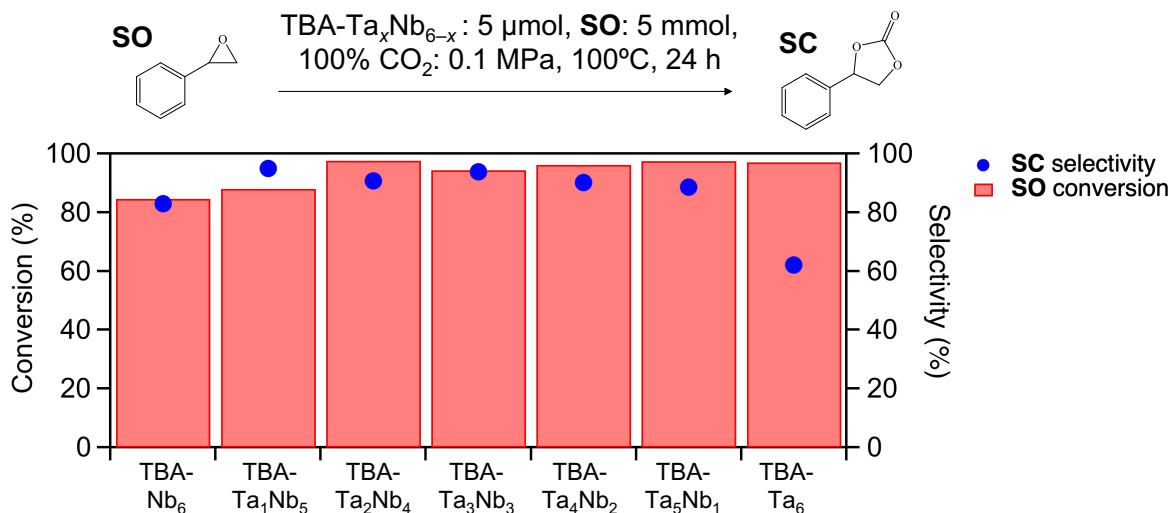


Figure 3-12. Catalytic activity of CO₂ fixation to **SO** using TBA-Ta_xNb_{6-x} as catalysts. Reaction condition: substrate: **SO**, 0.5 mmol; catalyst loading, 5 μmol; atmosphere: 100% CO₂ (0.1 MPa); reaction temperature, 100°C; reaction time, 24 h.

In order to understand the reaction mechanism and benefits of Ta-substitution in the clusters, several control reactions were taken place. In a reaction conducted under N₂ atmosphere comparing between TBA-Nb₆, TBA-Ta₁Nb₅, and TBA-Ta₆, a significant **SO** consumption was observed in the case of TBA-Ta₆ along with increased viscosity of the

product solution (Figure 3-13). The reaction using these three catalysts under N_2 did not result in a formation of SC and therefore the byproduct could be a polymerization of SO promoted by TBA-Ta₆.

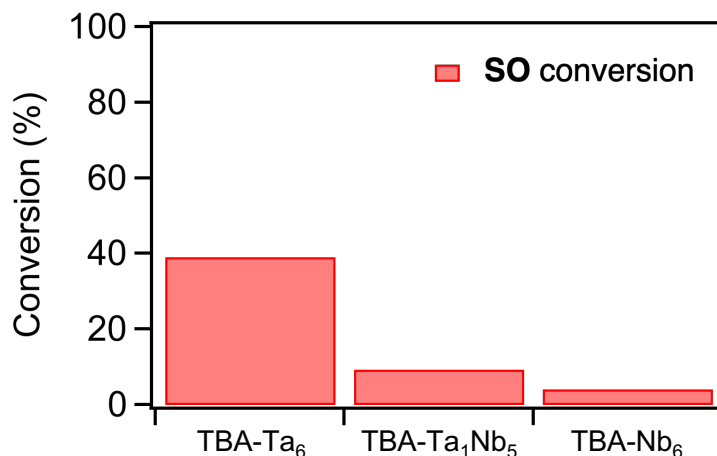


Figure 3-13. The SO consumption in the control reaction increased with Ta content. Reaction condition: substrate: SO, 5 mmol; catalyst loading, 5 μ mol; atmosphere, N_2 (0.1 MPa); reaction temperature, 100°C; reaction time: 6 h. Yield of SC was <1% in all cases.

The product solutions were analyzed to identify byproduct that was formed in the reaction promoted by TBA-Ta₆. From 1H nuclear magnetic resonance (NMR), the spectrum of the product solution promoted by TBA-Ta₆ was broader than the product solution of the TBA-Ta₁Nb₅-promoted reaction, suggesting a formation of polymer as a byproduct (Figure 3-14).

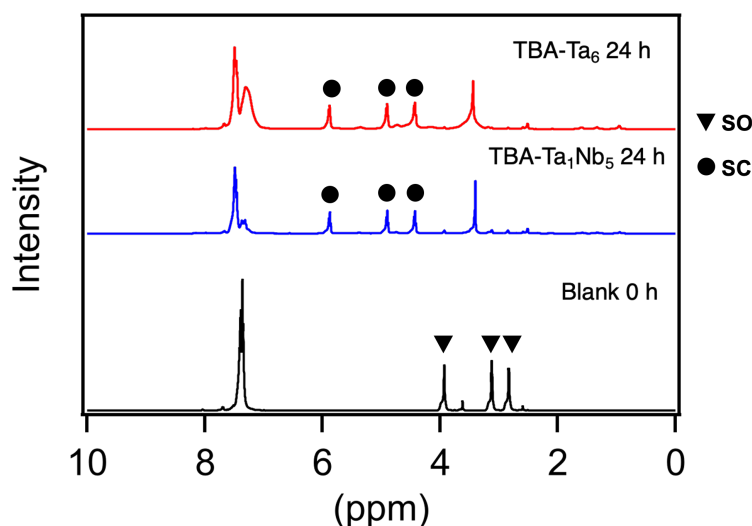


Figure 3-14. 1H NMR spectra of the product solutions promoted by TBA-Ta₆ and TBA-Ta₁Nb₅ in comparison with solution of SO and biphenyl (Blank). All solutions were diluted with DMSO-d₆.

One of the evaluating methods of basicity of the clusters was to perform density functional theory (DFT) calculation for natural bonding orbital (NBO) charge where the higher negative value indicates higher basicity. From the calculation results, the trend of the average

NBO charge was increased with higher Ta content (Figure 3-15). The highest basicity could be observed at the terminal O coordinated to Nb (terminal O_{Nb}) for TBA-Nb₆ or terminal O coordinated to Ta (terminal O_{Ta}) for Ta-incorporated clusters. It was noted that a slight increase in basicity was observed for the terminal O_{Ta} when the amount of substituted Ta decreased, but this increase applied for O_{Ta} and did not significantly affect the overall basicity of the clusters.

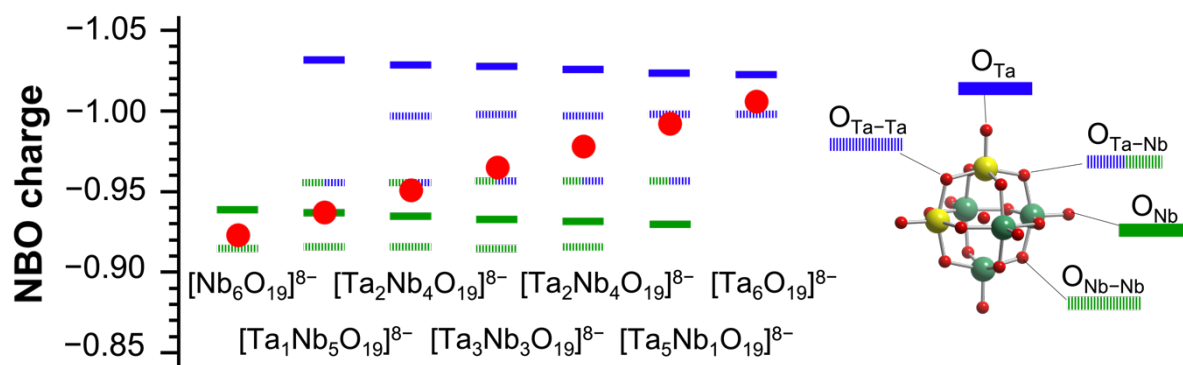


Figure 3-15. NBO charges on O atoms of the free $[\text{Ta}_x\text{Nb}_{6-x}\text{O}_{19}]^{8-}$. Solid line corresponds to terminal O and dashed line corresponds to bridging O between metals. Blue lines correspond to O coordinated to Ta while green lines correspond to O coordinated to Nb. Red dots indicate average NBO charges of the clusters.

The effect of CO₂ and SO adsorption on TBA-Ta_xNb_{6-x} was studied by XAFS. Pre-edge region of X-ray absorption near edge structure (XANES) spectra was used to identify the adsorption of the substrates. The pre-edge intensity came from the forbidden electronic transition from the 1s orbital to 4d(5p) hybridized orbital in the case of Nb K-edge and 2s orbital to 5d(6p) hybridized orbital for Ta L₁-edge.^{29,30} The forbidden electronic transition is caused by the distortion to the octahedral (*Oh*) symmetry of the MO₆ unit. After an adsorption of a substrate on the terminal O, the *Oh* symmetry would be improved, thus reducing the distortion and pre-edge absorption intensity. Therefore, the pre-edge intensity of XANES spectra could be used as a tool to identify the adsorption and activation of a substrate by the different basic sites of the clusters.

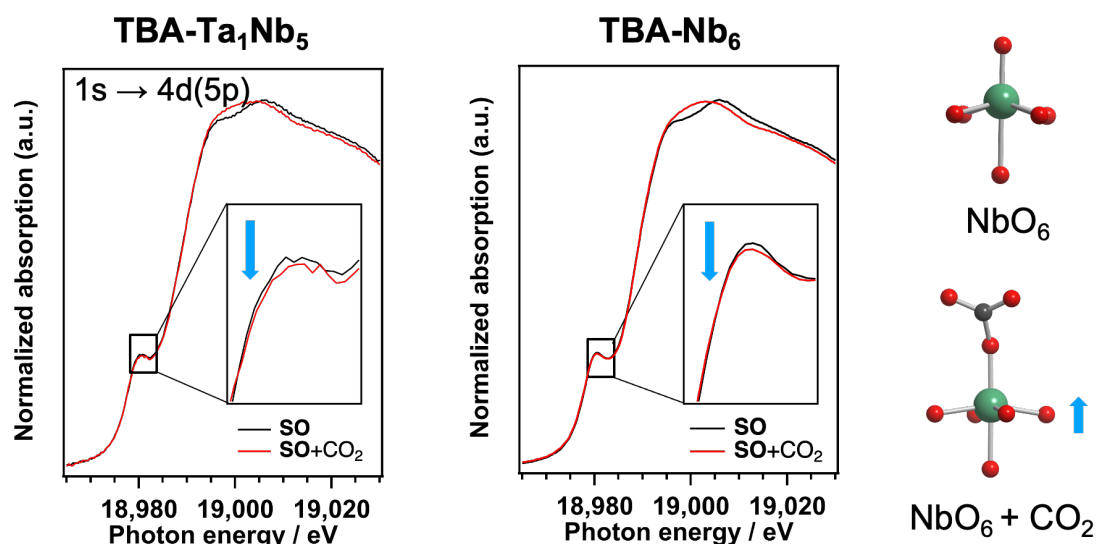


Figure 3-16. XANES spectra measuring Nb-K edge of TBA-Ta₁Nb₅ and TBA-Nb₆ dissolved in SO before and after CO₂ adsorption.

First, the effect of CO₂ adsorption was studied by XAFS. The XANES spectra of TBA-Nb₆, TBA-Ta₁Nb₅, and TBA-Ta₆ were measured after dissolving in SO in an absence and the presence of CO₂. The results demonstrated that CO₂ adsorption on all the clusters showed a decrease in pre-edge absorption intensity for both Nb K- (Figure 3-16) and Ta L₁-edges (Figure 3-17). As a result, CO₂ adsorption and activation could occur on any basic site of the catalyst, whether terminal O_{Nb} or terminal O_{Ta}. However, the greater difference was observed in Ta-L₁ edge, which implied that the basic site of Ta (terminal O_{Ta}) exhibited higher basicity than terminal O_{Nb}, as suggested by NBO charges, could activate CO₂ more effectively.

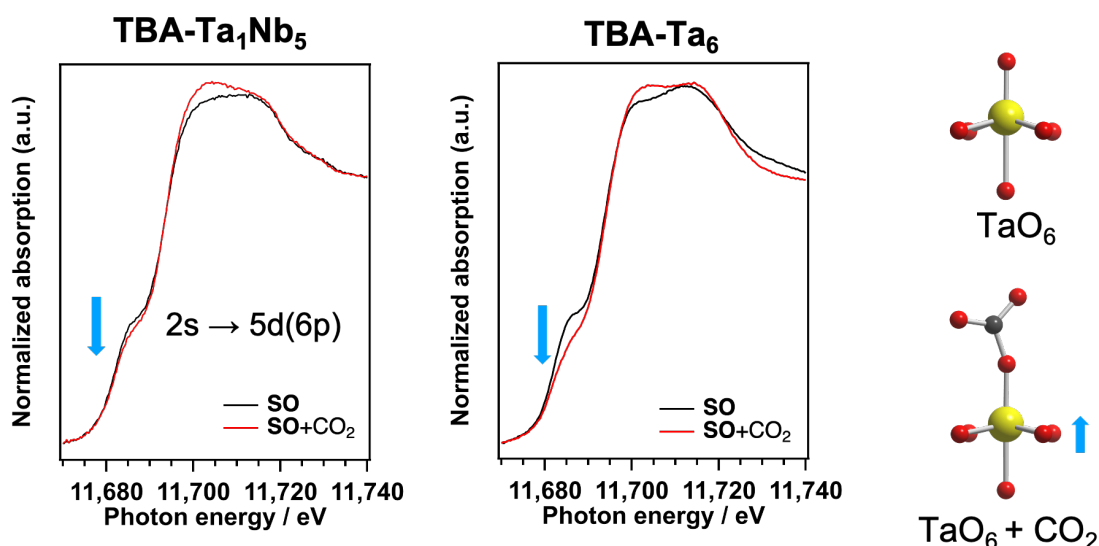


Figure 3-17. XANES spectra measuring Ta L₁-edge of TBA-Ta₁Nb₅ and TBA-Ta₆ dissolved in SO before and after CO₂ adsorption.

Our group's members investigated the effect of **SO** adsorption to the local structure of the clusters by observing the pre-edge absorption intensity of XANES spectra. TBA-Ta₄Nb₂ was dissolved in dimethyl formamide (DMF) as control sample in the measurement comparing to the spectra obtained after exposure to **SO** (Figure 3-18). The results revealed that the changes of the pre-edge intensity in Ta L₁-edge, while the results from the Nb K-edge measurement did not show a significant different, suggesting that adsorption and activation of **SO** occurred mainly on terminal O_{Ta} and hardly observed on the terminal O_{Nb}. The same results were also observed for pristine TBA-Ta₆ and TBA-Nb₆.

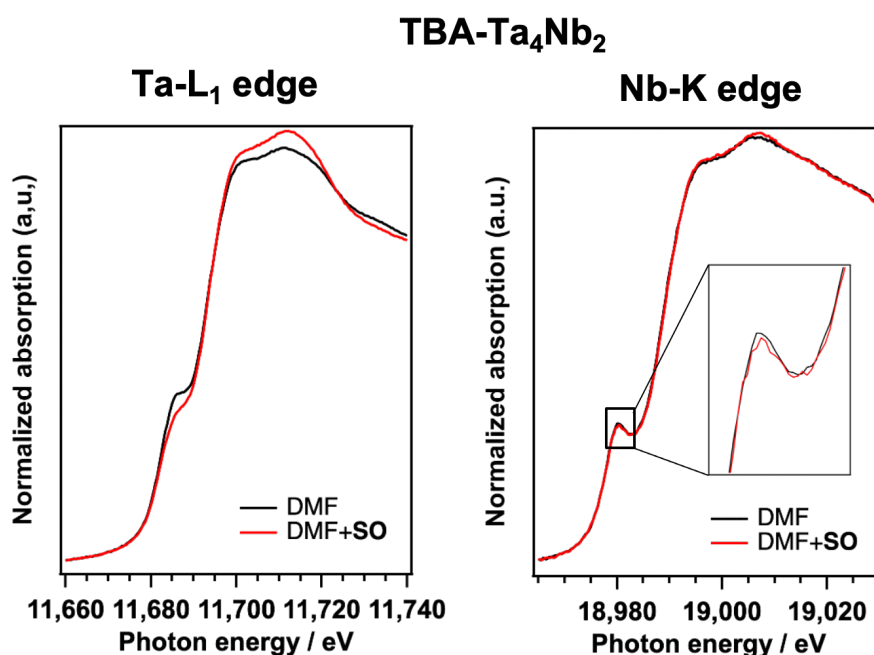


Figure 3-18. XANES spectra of Ta L₁-edge and Nb K-edge of TBA-Ta₄Nb₂ dissolved in DMF before and after exposure to **SO**.

As a result, the activation of **SO** by the basic site of Ta was understood to be the key factor that resulted in the formation of byproduct. From this hypothesis, if the activation of **SO** was the case for the formation of byproduct, TBA-Ta₁Nb₅ would not provide the highest **SC** selectivity among TBA-Ta_xNb_{6-x}. Therefore, further DFT calculation was conducted to understand the stability of the catalysts in different conditions. The calculation of the adsorption energy comparing between TBA-Ta₁Nb₅ with CO₂ and **SO** showed that the activation of CO₂ was preferred over **SO** (Figure 3-19). In addition, the activation would occur on the basic site of Ta than Nb.

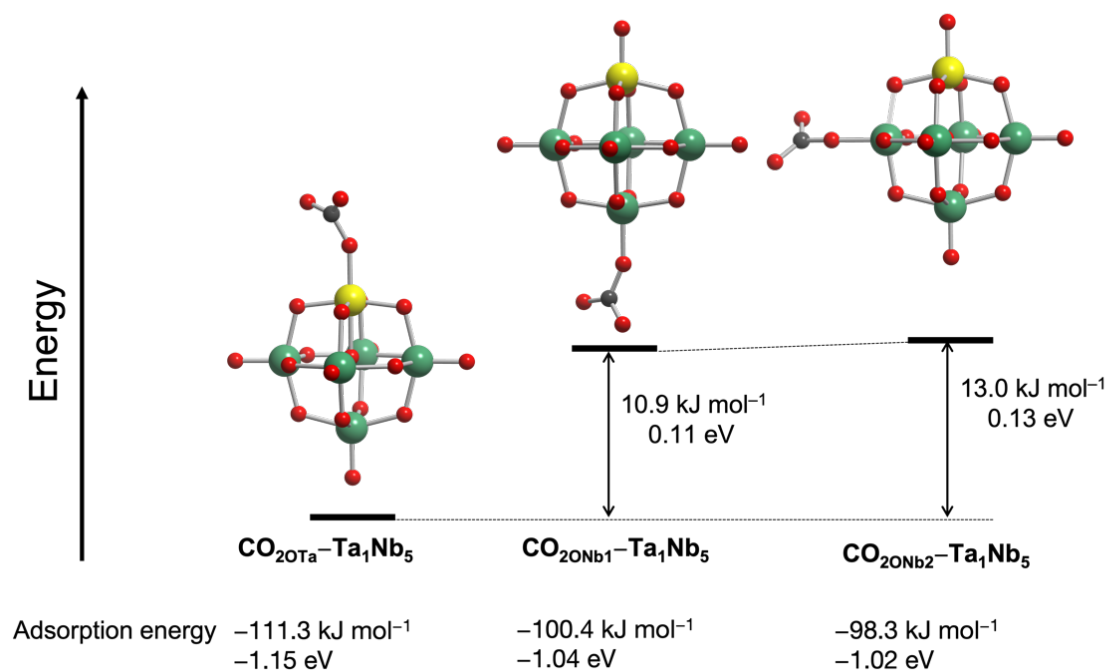


Figure 3-19. DFT calculation results of CO₂ activation on terminal O_{Ta} and on terminal O_{Nb} at two different locations.

To confirm the adsorption of CO₂ on the terminal O sites, FT-IR was used to determine the vibration corresponding to the terminal M=O bonding. The study was conducted using TBA-Ta₁Nb₅ as the sample dissolving in DMSO under N₂ atmosphere and after CO₂ exposure. The results indicated a spectral shift to longer wavenumber after CO₂ exposure, corresponding to the theoretical calculation where the bond length of Ta=O_t would be elongated from 1.83 Å to 2.00 Å after CO₂ adsorption (Figure 3-20). Thus, these data confirmed that the terminal O acted as the primary basic site for CO₂ adsorption and activation.

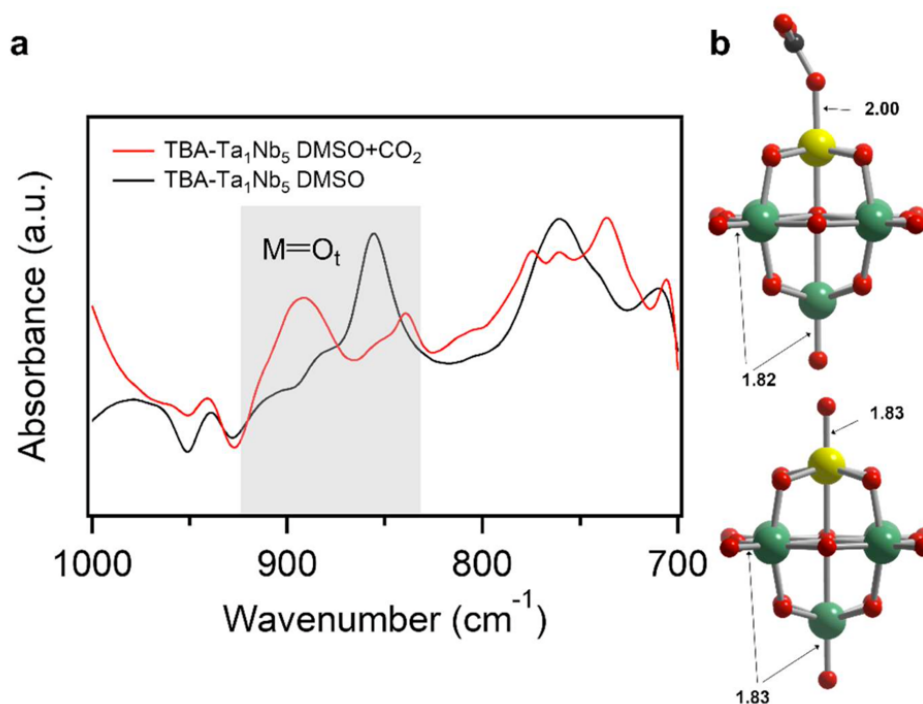


Figure 3-20. (a) FT-IR spectra of TBA-Ta₁Nb₅ dissolved in DMSO before and after CO₂ exposure and (b) structure of [Ta₁Nb₅O₁₉]⁸⁻ with CO₂ adsorption (top) and without CO₂ adsorption (bottom).

DFT calculation for **SO** activation was also carried out to analyze the possibility and compare to the experimental data based on [Ta₁Nb₅O₁₉]⁸⁻. From the calculation, the activation of **SO** by terminal O_{Ta} would require significantly lower energy comparing to activation of **SO** by terminal O_{Nb} (Figure 3-21). This theoretical evidence supported the XANES spectra where pre-edge intensity of Ta L₁-edge changed more significantly than Nb K-edge. In addition, the required energy to activate **SO** was significantly higher than the activation of CO₂, thus the terminal O_{Ta} has the preferential activation of CO₂ over **SO**. Since TBA-Ta₁Nb₅ contains only single Ta basic site (O_{Ta}), the preferential activation of CO₂ therefore resulted in highly selective conversion of **SO** to **SC** comparing to clusters with Ta content of 2 units or more. The higher basicity of O_{Ta} than O_{Nb} also resulted in higher catalytic performance of TBA-Ta₁Nb₅ than TBA-Nb₆.

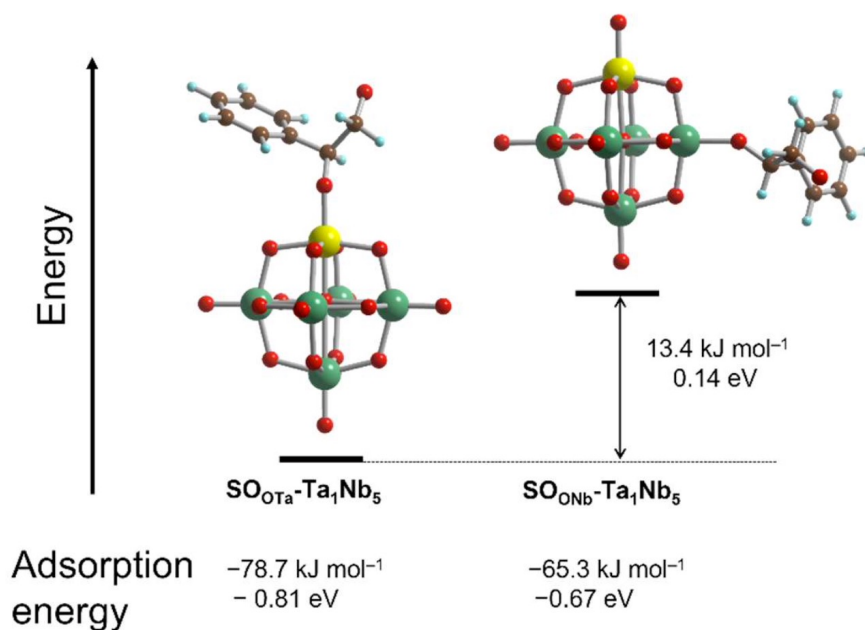


Figure 3-21. Adsorption energy of **SO** on terminal O_{Ta} and terminal O_{Nb}.

Then, the overall catalytic performance profile was analyzed by conducting time-course reaction (Figure 3-22). The **SO** conversion rate followed the order of TBA-Ta₆ > TBA-Ta₁Nb₅ > TBA-Nb₆ with initial turn over frequency (TOF) values of 175, 84, and 43 h⁻¹, respectively. The turn over number (TON) values after 24 h of reaction were 988, 922, and 724 for TBA-Ta₆, TBA-Ta₁Nb₅, and TBA-Nb₆, respectively, which surprisingly revealed a significant improvement in catalytic performance of TBA-Ta₁Nb₅ over TBA-Nb₆ with just only one Ta-substitution. Such improvement could be owed to the high basicity of O_{Ta} of [Ta₁Nb₅]⁸⁻ comparing to basicity of O_{Nb} of [Nb₆O₁₉]⁸⁻ indicated by NBO charge in Figure 3-15 that responsible for CO₂ activation.

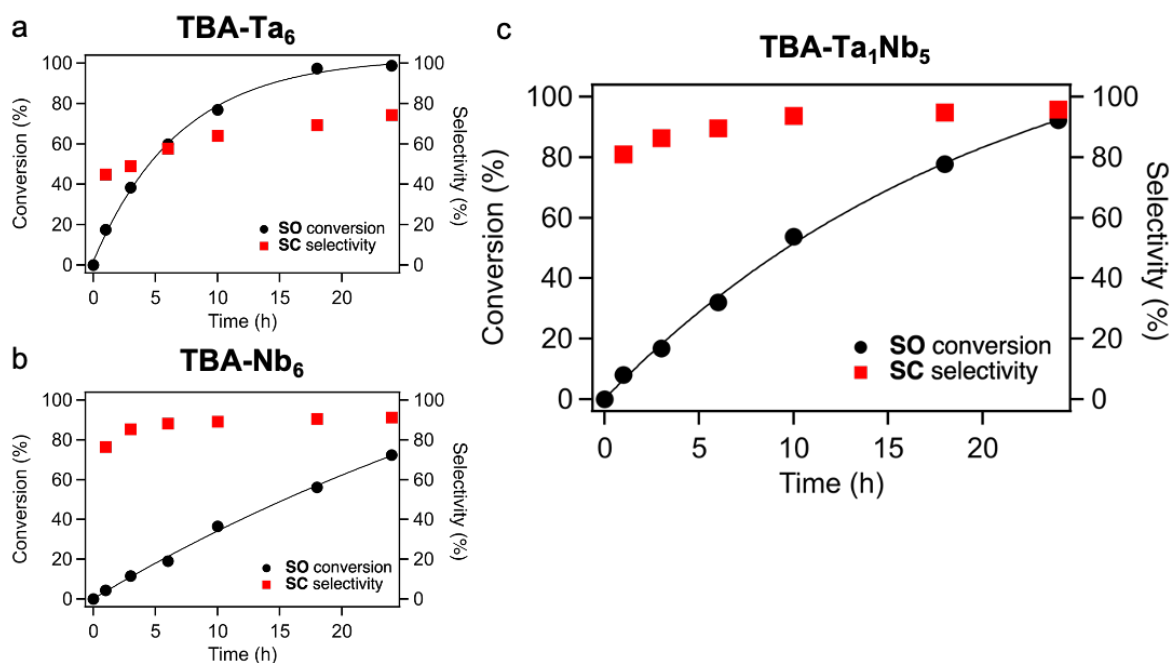


Figure 3-22. Time-course results of CO₂ fixation to SO (a) TBA-Ta₆, (b) TBA-Nb₆, and (c) TBA-Ta₁Nb₅ as catalysts. Reaction condition: substrates: SO, 1.0 mmol; catalyst loading, 10 μmol; atmosphere: 100% CO₂ (0.1 MPa); temperature: 100°C; reaction time: 24 h.

Furthermore, the relationship of the SO concentration and the partial pressure of CO₂ to the reaction rate was determined. The concentration of SO was carried out by diluting in DMSO ranging from 1 M to 5 M condition. The rate law determined showed no significant effect of SO concentration to the reaction rate, with the order of -0.07 (Figure 3-23a). On the other hand, the effect of partial pressure of CO₂ to reaction rate was determined using N₂ as balance gas with CO₂ concentration of 10%, 20%, 50%, and 100%. The order was calculated to be 1.04 thus suggesting that the rate determination step was nucleophilic attack of activated CO₂ to SO (Figure 3-23b).

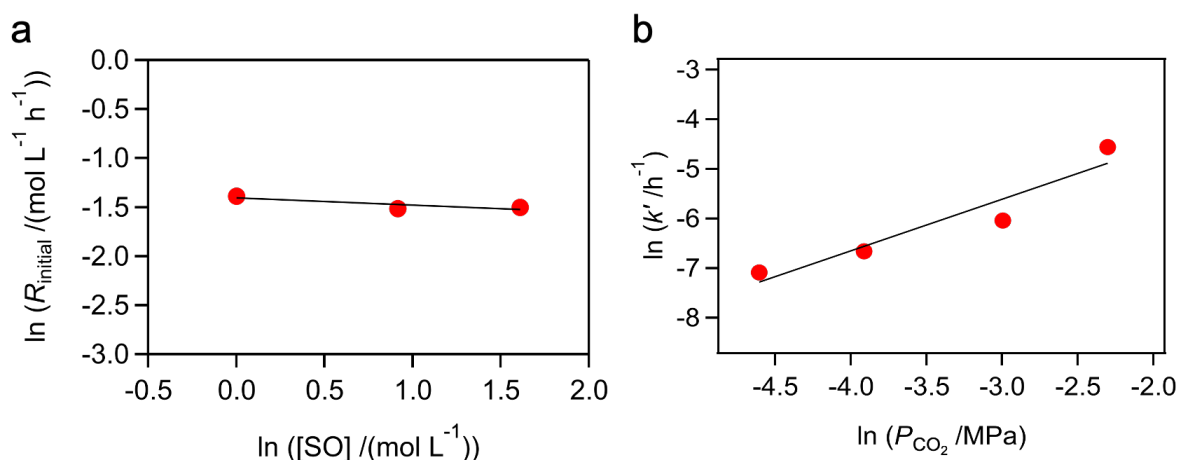


Figure 3-23. The effect of (a) SO concentration and (b) partial pressure of CO₂ to the reaction rate. Reaction condition: substrates: SO, 0.5 mmol; catalyst loading, 5 μmol; atmosphere: 100% CO₂ (0.1 MPa); temperature: 100°C; reaction time: 6 h.

To confirm the relationship between reaction order of CO₂ partial pressure to the catalytic performance, Figure 3-24 summarized the result using TBA-Nb₆ and TBA-Ta₆ as catalysts for 6 h conducted at different CO₂ partial pressure. It was clear that the conversion of **SO** promoted by TBA-Ta₆ was significantly higher than TBA-Nb₆. In both types of catalysts, the conversion of **SO** was not significantly different, however, the selectivity of **SC** was improved with higher CO₂ partial pressure in the reactions promoted by TBA-Nb₆, which correspond to the high order calculated. Meanwhile, the trend of increasing **SC** selectivity with higher CO₂ partial pressure was not observed in the reactions promoted by TBA-Ta₆.

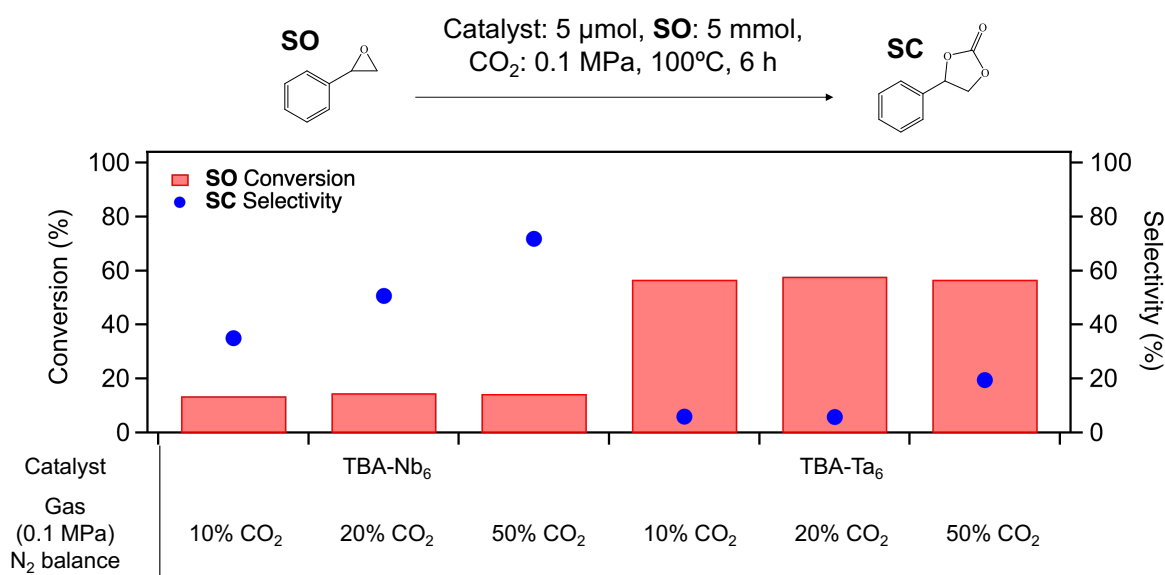
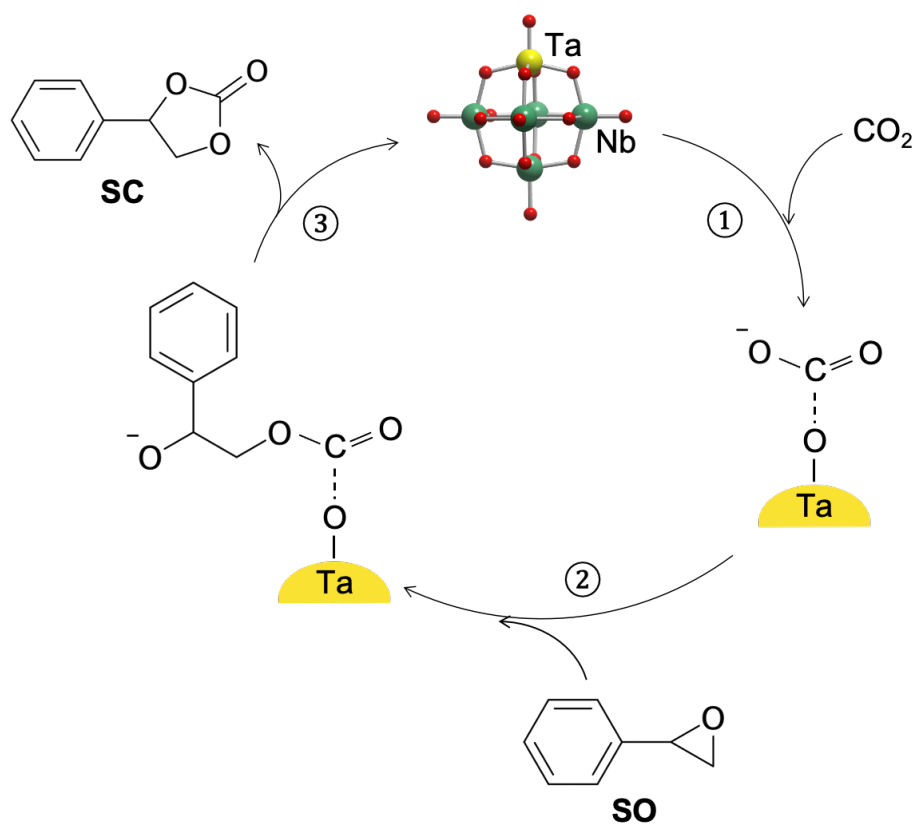


Figure 3-24. Catalytic activity of CO₂ fixation to **SO** using TBA-Ta_xNb_{6-x} as catalysts. Reaction condition: substrate, **SO** (0.5 mmol); atmosphere, CO₂/N₂ (0.1 MPa); reaction temperature, 100°C; reaction time, 6 h.

From experimental and theoretical data, the following reaction mechanism was proposed (Scheme 3-1). The reaction began with CO₂ activation on the most basic site of the cluster, which was the terminal O_{Ta} to form nucleophilic species (Scheme 3-1, step 1). The nucleophilic attack of the activated CO₂ to **SO** would occur that is the rate determining step of the reaction to form phenolate species (Scheme 3-1, step 2). Then, the nucleophilic attack to the carbonyl carbon resulted in formation of **SC** as the product and the catalyst was regenerated (Scheme 3-1, step 3).



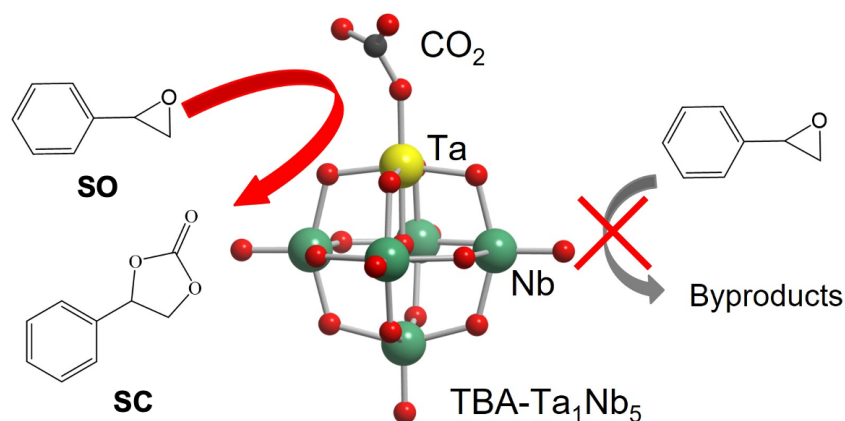
Scheme 3-1. Proposed mechanism of CO₂ fixation promoted by TBA-Ta₁Nb₅, where CO₂ would be activated to nucleophilic species (step 1), which reacted with SO to form phenolate species (step 2), and nucleophilic attack to carbonyl carbon to form SC and catalyst regeneration (step 3).

3.4 Conclusions

The catalytic CO₂ fixation to **SO** by TBA-Ta₆ posted a problem of limited selectivity to **SC** due to the formation of byproducts. On the other hand, when conducting the reaction with TBA-Nb₆ as the catalyst, **SO** conversion was low while the selectivity to **SC** was high. Since the selective formation of **SC** is desired, therefore the development of a suitable catalyst was explored in this chapter. It was hypothesized that mixed Ta-Nb oxide cluster would improve **SC** selectivity.

From experimental results, TBA-Ta₁Nb₅ exhibited the highest **SC** selectivity with an improved **SO** conversion comparing to TBA-Nb₆. The TON over 24 h of reaction provided by TBA-Ta₁Nb₅ (922) was almost comparable to TBA-Ta₆ (988), which are significantly higher than that of TBA-Nb₆ (724). The high **SC** selectivity could be maintained even after prolonging the reaction time from 6 to 24 h where high **SO** conversion was also obtained.

XAFS studies revealed the function of the basic site of Nb and Ta that affect substrate activation. The activation of **SO** by the basic site of Ta led to formation of byproduct, while the activation of CO₂ would result in high formation of **SC**. Thus, in order to achieve high **SC** selectivity, it is necessary to activate CO₂ while suppressing the activation of **SO**. The single Ta-substitution therefore resulted in the desired results because the presence of one Ta basic site provided high basicity for CO₂ activation and the other Nb basic site helped suppressing the activation of **SO** as illustrated in Scheme 3-2. DFT calculation revealed a preferential activation of CO₂ over **SO** by Ta basic site suggested by lower adsorption energy.



Scheme 3-2. Illustration on mechanism of CO₂ fixation to **SO** and suppression of **SO** activation using TBA-Ta₁Nb₅ as the catalyst.

3.5 References

- (1) Osman, A. I.; Hefny, M.; Abdel Maksoud, M. I. A.; Elgarahy, A. M.; Rooney, D. W. *Environ. Chem. Lett.* **2021**, *19* (2), 797–849.
- (2) Yoro, K. O.; Daramola, M. O.; Sekoai, P. T.; Armah, E. K.; Wilson, U. N. *Renew. Sustain. Energy Rev.* **2021**, *147*, 111241.
- (3) Liu, Q.; Wu, L.; Jackstell, R.; Beller, M. *Nat. Commun.* **2015**, *6* (1), 5933.
- (4) Coates, G. W.; Moore, D. R. *Angew. Chem. Int. Ed.* **2004**, *43* (48), 6618–6639.
- (5) Sakakura, T.; Kohno, K. *Chem. Commun.* **2009**, No. 11, 1312.
- (6) Clements, J. H. *Ind. Eng. Chem. Res.* **2003**, *42* (4), 663–674.
- (7) North, M.; Omedes-Pujol, M. *Tetrahedron Lett.* **2009**, *50* (31), 4452–4454.
- (8) Clegg, W.; Harrington, R. W.; North, M.; Pizzato, F.; Villuendas, P. *Tetrahedron Asymmetry* **2010**, *21* (9–10), 1262–1271.
- (9) Jessop, P. G. *Green Chem.* **2011**, *13* (6), 1391.
- (10) S. Bello Forero, J.; A. Hernández Muñoz, J.; Jones Junior, J.; M. da Silva, F. *Curr. Org. Synth.* **2016**, *13* (6), 834–846.
- (11) Pescarmona, P. P. *Curr. Opin. Green Sustain. Chem.* **2021**, *29*, 100457.
- (12) Fukuoka, S.; Fukawa, I.; Tojo, M.; Oonishi, K.; Hachiya, H.; Aminaka, M.; Hasegawa, K.; Komiya, K. *Catal. Surv. Asia* **2010**, *14* (3–4), 146–163.
- (13) Fleischer, M.; Blattmann, H.; Mülhaupt, R. *Green Chem.* **2013**, *15* (4), 934.
- (14) Rokicki, G. *Prog. Polym. Sci.* **2000**, *25* (2), 259–342.
- (15) Yu, W.; Maynard, E.; Chiaradia, V.; Arno, M. C.; Dove, A. P. *Chem. Rev.* **2021**, *121* (18), 10865–10907.
- (16) Zhang, S. S. *J. Power Sources* **2006**, *162* (2), 1379–1394.
- (17) Xu, K. *Chem. Rev.* **2004**, *104* (10), 4303–4418.
- (18) Tillmann, S. D.; Isken, P.; Lex-Balducci, A. *J. Power Sources* **2014**, *271*, 239–244.
- (19) Yun, J.; Zhang, L.; Qu, Q.; Liu, H.; Zhang, X.; Shen, M.; Zheng, H. *Electrochimica Acta* **2015**, *167*, 151–159.
- (20) Kawai, H.; Sakamoto, F.; Taguchi, M.; Kitamura, M.; Sotomura, M.; Tsukamoto, G. *Chem. Pharm. Bull. (Tokyo)* **1991**, *39* (6), 1422–1425.
- (21) Cascio, G.; Manghisi, E.; Porta, R.; Fregnan, G. *J. Med. Chem.* **1985**, *28* (6), 815–818.
- (22) Hayashi, S.; Sasaki, N.; Yamazoe, S.; Tsukuda, T. *J. Phys. Chem. C* **2018**, *122* (51), 29398–29404.
- (23) Kamata, K.; Sugahara, K. *Catalysts* **2017**, *7* (11), 345.
- (24) Fukada, M.; Shibata, K.; Imai, T.; Yamazoe, S.; Hosokawa, S.; Wada, T. *J. Ceram. Soc. Jpn.* **2013**, *121* (1409), 116–119.
- (25) Kikkawa, S.; Tsukada, M.; Shibata, K.; Fujiki, Y.; Shibusawa, K.; Hirayama, J.; Nakatani, N.; Yamamoto, T.; Yamazoe, S. *Symmetry* **2021**, *13* (7), 1267.
- (26) Rambaran, M. A.; Pascual-Borràs, M.; Ohlin, C. A. *Eur. J. Inorg. Chem.* **2019**, *2019* (35), 3913–3918.
- (27) Momma, K.; Izumi, F. *J. Appl. Crystallogr.* **2011**, *44* (6), 1272–1276.
- (28) Asakura, H.; Yamazoe, S.; Misumi, T.; Fujita, A.; Tsukuda, T.; Tanaka, T. *Radiat. Phys. Chem.* **2020**, *175*, 108270.
- (29) Asakura, H.; Shishido, T.; Yamazoe, S.; Teramura, K.; Tanaka, T. *J. Phys. Chem. C* **2011**, *115* (48), 23653–23663.
- (30) Yamazoe, S.; Hitomi, Y.; Shishido, T.; Tanaka, T. *J. Phys. Chem. C* **2008**, *112* (17), 6869–6879.

3.6 Appendix

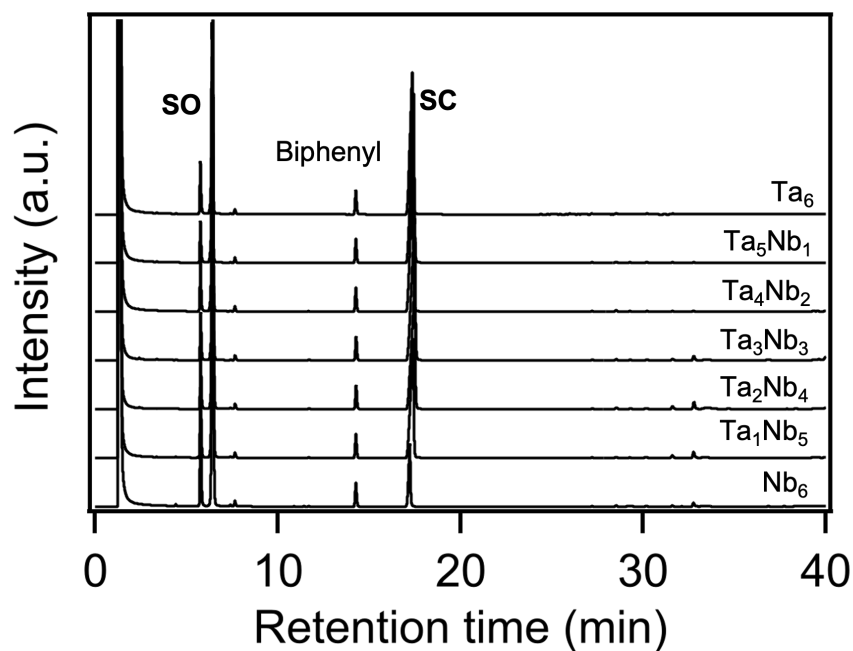


Figure S3-1. GC-FID spectra of CO₂ fixation to SO. Reaction condition: substrates: SO, 0.5 mmol; atmosphere: 100% CO₂ (0.1 MPa); temperature: 100°C; reaction time: 6 h.

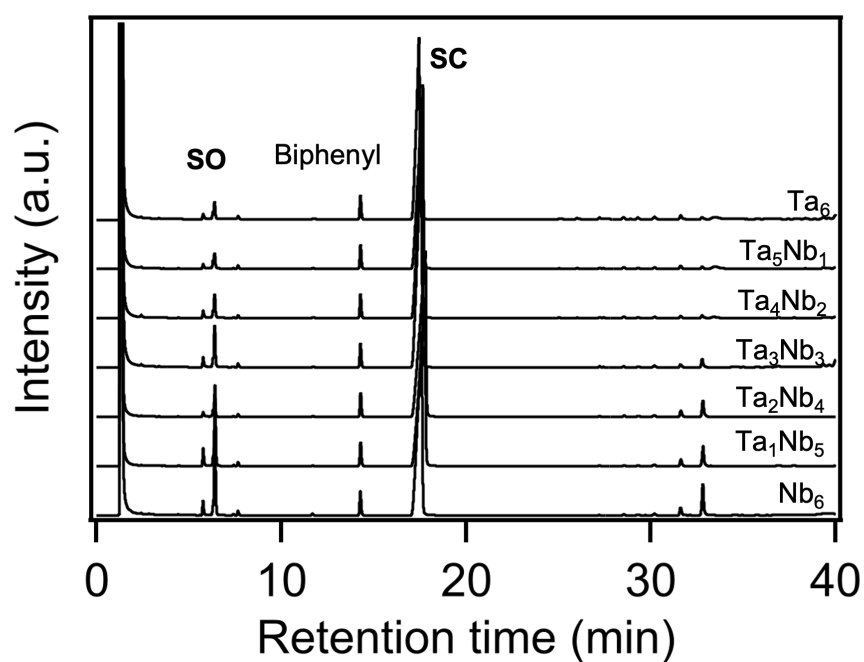


Figure S3-2. GC-FID spectra of CO₂ fixation to SO. Reaction condition: substrates: SO, 0.5 mmol; atmosphere: 100% CO₂ (0.1 MPa); temperature: 100°C; reaction time: 24 h.

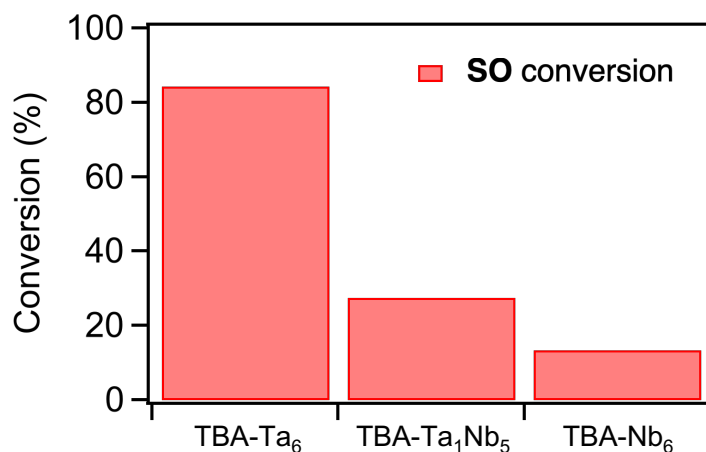


Figure S3-3. The **SO** consumption in the control reaction increased with Ta content. Reaction condition: substrate: **SO** (5 mmol); catalyst loading, 5 μ mol; atmosphere, N₂ (0.1 MPa); reaction temperature: 100°C; reaction time: 24 h. Yield of **SC** was <1% in all cases.

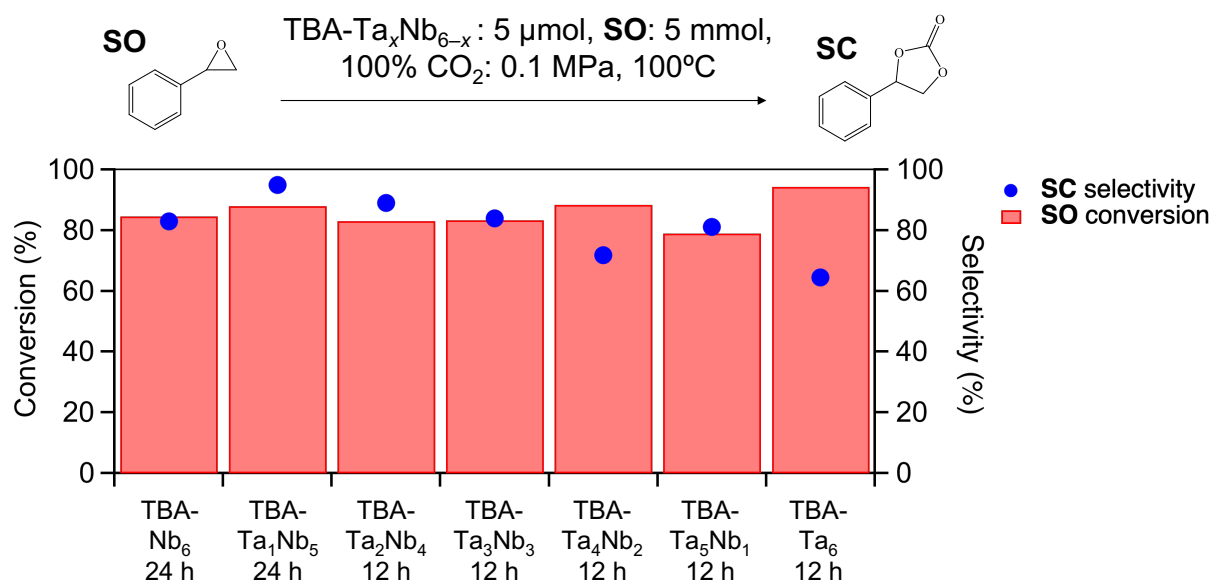


Figure S3-4. CO₂ fixation to **SO** results at optimized condition to obtain **SO** conversion over 80%. Reaction condition: substrate: **SO**, (5 mmol); catalyst loading, 5 μ mol; atmosphere, 100% CO₂ (0.1 MPa); reaction temperature: 100°C.

Chapter 4. Bifunctional catalysis of composite clusters

4.1. Introduction

Composite catalysts have recently gained significant attention because of the combination of different functionalities that promote the reaction. Our group developed $[\text{Nb}_6\text{O}_{19}]^{8-}$ -modified Au nanoparticles on Al_2O_3 support as a composite catalyst.¹ The electron donation from $[\text{Nb}_6\text{O}_{19}]^{8-}$ allowed a self-assembly process for $[\text{Nb}_6\text{O}_{19}]^{8-}$ to attach on the surface of Au nanoparticles (Figure 4-1).¹⁻⁶ The resultant composite catalyst exhibited significant improvement in the reduction of *p*-nitrophenol to *p*-aminophenol with high efficiency. The H_2 cleavage occurred at the interface between Au nanoparticles and $[\text{Nb}_6\text{O}_{19}]^{8-}$ in a heterolytic manner that resulted in polar hydrogen species to selectively reduce nitro group which is a polar functional group.^{1,7}

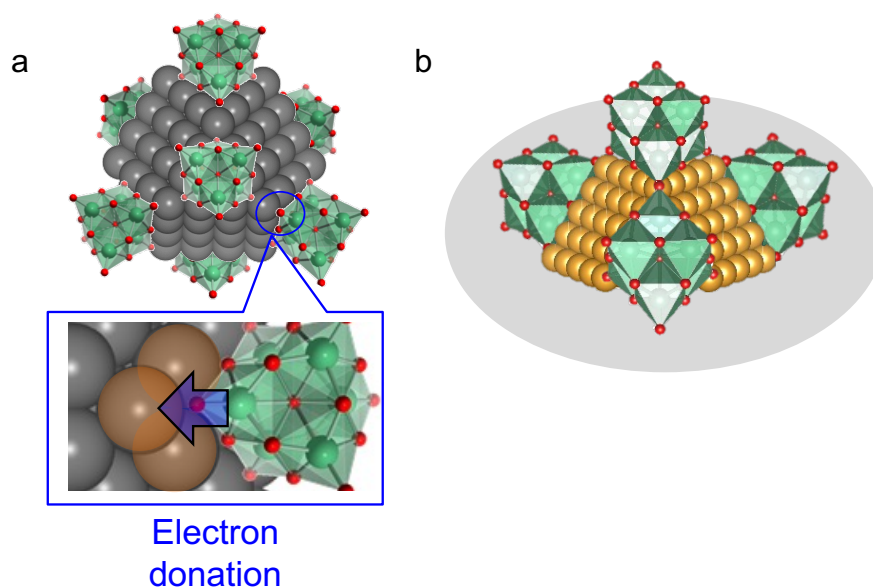


Figure 4-1. Illustration of (a) $[\text{Nb}_6\text{O}_{19}]^{8-}$ -modified metal nanoparticles with an enlargement to show the interaction on the surface and (b) composite $[\text{Nb}_6\text{O}_{19}]^{8-}$ -modified Au/ Al_2O_3 .¹

Incorporation of metal ion to polyoxometalates, such as Palladium(II) containing γ -Keggin silicodecatungstate, $[\gamma\text{-H}_2\text{SiW}_{10}\text{O}_{36}\text{Pd}_2(\text{OAc})_2]^{4-}$ for hydration of nitriles (Figure 4-2).⁸ The reaction was proceeded by the elimination of acetate ligand as a result of reaction between catalyst and water, followed by a reversible coordination of nitriles to the Pd center to form a complex. Subsequently, the nucleophilic attack of hydroxide or water on nitrile carbon atom resulted in amide formation and the catalyst was regenerated.⁸

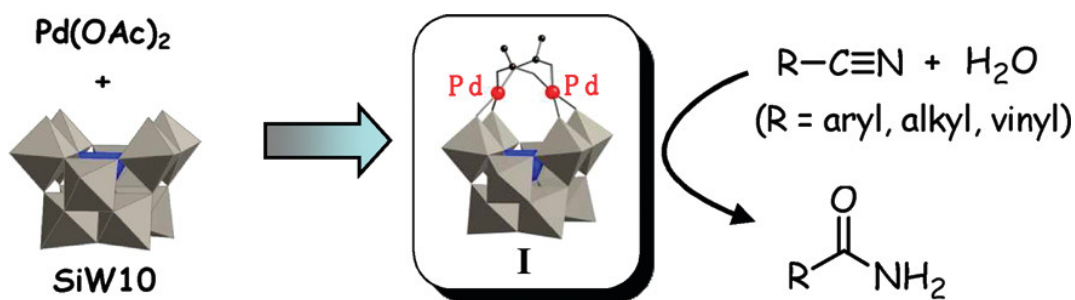


Figure 4-2. Schematic illustration of the formation of the $[\gamma\text{-H}_2\text{SiW}_{10}\text{O}_{36}\text{Pd}_2(\text{OAc})_2]^{4-}$ that promote hydration of nitriles.⁸

N-formylation of amine has been conducted using CO or phosgene as carbonyl sources in the industrial scale of formamide production, Formamides are important intermediates in the production of pharmaceuticals and fine chemicals.^{9–15} Since those carbonyl sources pose toxicity, the alternative pathway of utilizing CO₂ as a C1 source. In addition, H₂ would be used as a reducing agent due to high abundance and provide higher atom efficiency over organic silicones.^{16–18} Thus, the combination of CO₂ and H₂ is appealing for *N*-formylation of amine, where water would be generated as a byproduct.^{19–21} One of the barriers to utilize CO₂ is its high activation energy because it is the most oxidative form of carbon and is highly stable. Strong base catalyst is therefore required to activate CO₂ to react with substrate and yield carbonylated products.

Bimetallic Pd–Au alloy nanoparticles on polyaniline-functionalized carbon nanotubes have shown activity for *N*-formylation of amine.^{13–15,22} Since Pd and Au are active for CO₂ reduction, bimetallic Pd–Au therefore has gained attention to be utilized as catalyst for *N*-formylation of pyrrolidine to *N*-formylpyrrolidine. The results indicated the significant improvement in product yield than the reaction promoted by only Pd or Au nanoparticles (Figure 4-3).²²

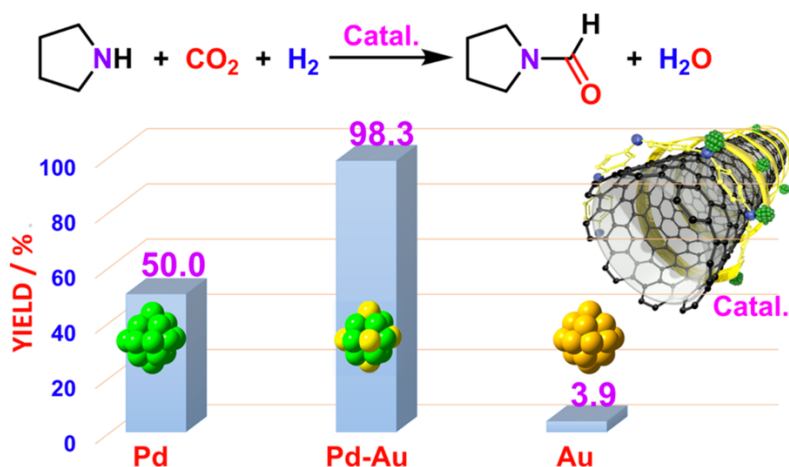
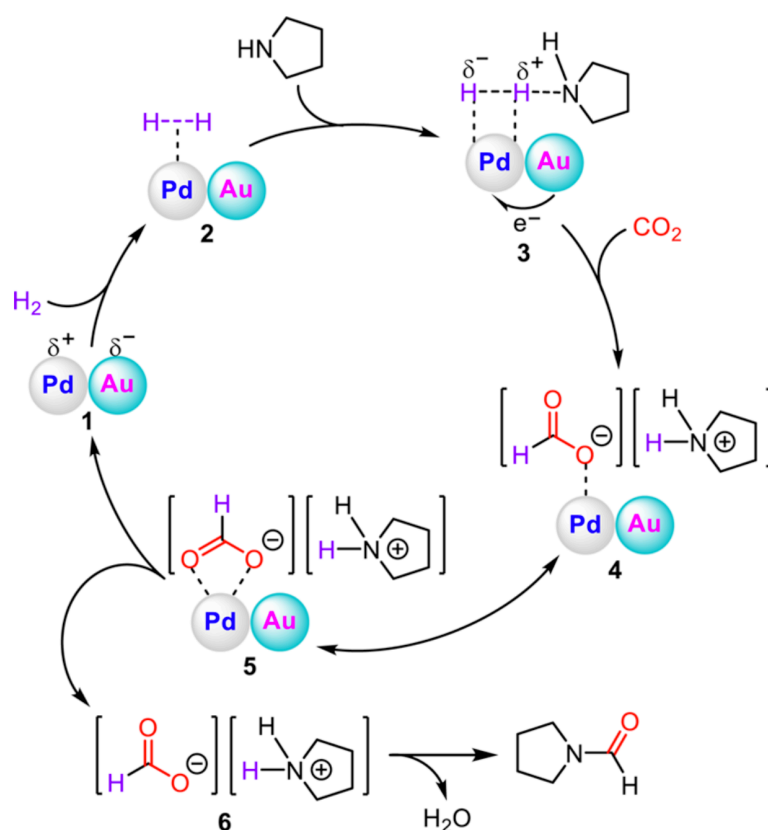


Figure 4-3. Result of *N*-formylation of pyrrolidine using Pd, Pd–Au alloy, and Au nanoparticles supported polyaniline-functionalized carbon nanotubes.²²

The reaction mechanism was proposed to identify the active sites of this alloy Pd–Au nanoparticles and understand the driving force of this reaction (Scheme 4-1).²² Theoretical calculation suggested that the surface Pd atoms possess positive charge while surface of Au atoms hold negative charge. The activation of H₂ occurred after the adsorption on surface of Pd atoms. During the reaction, the basicity of pyrrolidine promoted the partial heterolytically cleavage of H₂ to form adduct species. Then, electron transfer from surface of Au atom to Pd atom increased the electron density of Pd that improved the reactivity of Pd–H metal hydride bond. After that, formate anion was generated as a result of insertion of CO₂ into Pd–H bond which was stabilized by the basicity of the pyrrolidine and the product was obtained after thermal decomposition of pyrrolidine.



Scheme 4-1. Mechanism of *N*-formylation of pyrrolidine promoted by Pd–Au bimetallic catalysts.²²

In the work reported by Zhang and co-workers demonstrated effective *N*-formylation of amine catalyzed by Pd(NH₃)_{*x*}Cl_{*y*}/C in the presence of KOH (Figure 4-4).²³ The formation of active Pd species in-situ occurred which then acted as an activation site of CO₂ and subsequently react with amine to form formamide. The presence of KOH in the system acted as the basic site and facilitated the reaction.

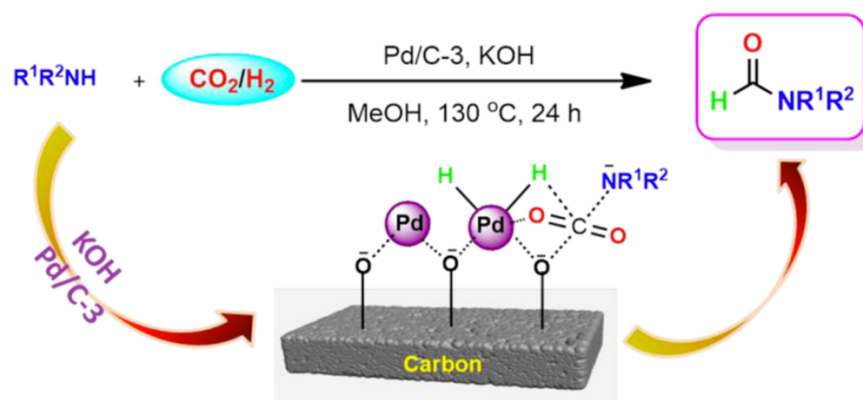


Figure 4-4. *N*-formylation of amine promoted by $\text{Pd}(\text{NH}_3)_x\text{Cl}_y/\text{C}$ with the presence of KOH .²³

This chapter would focus on the utilization of Pt incorporated polyoxoniobates with a sandwich-type structure, $[\text{Pt}(\text{Nb}_6\text{O}_{19})_2]^{12-}$ ($\text{Pt}(\text{Nb}_6)_2$),²⁴ as a catalyst with the hypothesis that Pt would provide redox property while polyoxoniobates act as base catalysts. To the best of knowing, this catalyst has not been applied in catalytic reaction, therefore, it would be interesting to elucidate its bifunctional catalysis. Previously, $(\text{Pt}(\text{Nb}_6)_2)$ was employed as a catalyst in a conversion of cyclic amine to form urea in a presence of CO_2 and H_2 , however, the reaction was not successful. As a result, other potential reactions were then selected evaluate the catalytic applications, which would be *N*-formylation of amine using piperidine as a model substrate. According to the work reported by Zhang *et al.*,²³ the function of $(\text{Pt}(\text{Nb}_6)_2)$ could be applied as a bifunctional catalyst without external base addition required as illustrated in Figure 4-5.

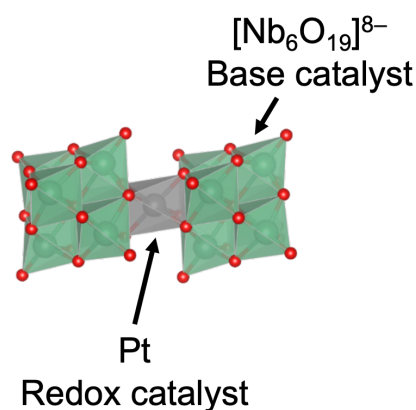


Figure 4-5. Structure of $[\text{Pt}(\text{Nb}_6\text{O}_{19})_2]^{12-}$ ($\text{Pt}(\text{Nb}_6)_2$) with hypothesized functionalities.

4.2 Experimental

$K_8[Nb_6O_{19}] \cdot 14H_2O$ (33.4% Nb) (Mitsuwa Chemicals Co., Ltd.), $CsOH \cdot 6H_2O$ (Alfa Aesar), $H_2Pt(OH)_6$ (Aldrich), tetrabutylammonium hydroxide 40% in aqueous solution (TBAOH, Tokyo Chemical Industry (TCI)), solvents: dimethyl sulfoxide (DMSO, TCI), methanol (MeOH, Kanto Chemical), dimethylacetamide (DMA, TCI) substrates: biphenyl (Kanto Chemical), piperidine, 1-methylpiperazine, piperazine anhydrous, morpholine, 1,2,3,4-tetrahydroisoquinoline, dibutylamine were purchased from TCI and used as received.

4.2.1 Synthesis of $[Pt(Nb_6O_{19})_2]^{12-}$ ($Pt(Nb_6)_2$)

$Pt(Nb_6)_2$ was prepared according to literature with slight modification.²⁴ To the Teflon-lined autoclave, $K_8[Nb_6O_{19}] \cdot 14H_2O$ (200 mg, 841 μmol Nb) was dissolved in 5 mL of Milli-Q H_2O , $H_2Pt(OH)_6$ (21.0 mg, 70.1 μmol) was added to the clear solution to form pale yellow solution after stirring for few minutes. 2 M $CsOH$ solution (50 μL) was added to stabilize pH of the solution to 12. Then, the autoclave containing the solution was heated in an oven to 170°C for 10 h. Upon cooling to room temperature, the solution was filtered to remove any unreacted substrates and evaporated to obtain $Pt(Nb_6)_2$. The obtained product was characterized by electrospray ionization-mass spectrometry (ESI-MS) in negative ion mode with 1 M aqueous solution (micrOTOF-II, Bruker), Fourier-transform infrared spectrometer (JASCO, FT/IR-4600) equipped with attenuated total reflection accessory (JASCO, ATR PRO ONE), X-ray diffraction (XRD), thermal gravimetric-differential thermal analysis (TG-DTA), and X-ray absorption fine structure (XAFS, BL01B1, SPring-8).

4.2.2 General procedure for *N*-formylation reaction

N-formylation reactions were carried out in a stainless-steel autoclave (30 mL). After loading the catalyst, the solution containing substrate, biphenyl, and the solvent was added to the reactor, which was sealed and replaced air with CO_2 three times, then H_2 was purged afterward. The reaction was then carried out at a specified time (6–36 h). The products were analyzed after catalyst removal by GC-FID and GC-MS.

4.2.3 Procedure for time course reaction

Time course reaction result was collected by opening the reaction vessel upon cooling in water bath, after sampling small amount of solution (~50 μL), the vessel was closed and purged with CO_2 and H_2 at the designated pressure prior to continuing the reaction.

4.2.4 Procedure for reusability test

The reusability test was conducted by collecting catalyst from reaction solution through centrifugation. After washing with MeOH and drying, the recovered catalyst was used in the next run keeping other parameters the same.

4.2.5 Calculation of product yield:

$$\text{Conversion} = \frac{(s_0 - s)}{s_0} \times 100\%$$

$$\text{Yield} = \frac{p}{s_0} \times 100\%$$

$$\text{Selectivity} = \frac{\text{Yield}}{\text{Conversion}} \times 100\%$$

where s denotes the amount of substrate and subscripted 0 refers to the initial condition and p denotes the amount of product. The amounts of substrates and products were calculated from the calibration curve using biphenyl as the internal standard.

Calculation of turn over number (TON) and turn over frequency (TOF):

$$\text{TON} = \frac{\text{Moles of product}}{\text{Moles of catalyst}}$$

$$\text{TOF} = \frac{\text{TON}}{\text{Time}}$$

4.2.6 Illustration of catalysts

The obtained crystallographic data were used to visualize the structure of catalysts using VESTA program.²⁵

4.3 Results and discussion

4.3.1 Synthesis of $[\text{Pt}(\text{Nb}_6\text{O}_{19})_2]^{12-}$ ($\text{Pt}(\text{Nb}_6)_2$)

The structural features and composition of the fabricated $\text{Pt}(\text{Nb}_6)_2$ were characterized by XRD, FT-IR, ESI-MS, TG-DTA, and XAS. XRD patterns could be used to distinguish the sandwich-type structure from the Lindqvist-type precursor. The diffraction pattern in the 2θ region between 8–12 degrees was indicative of the counter cations. The pattern of the fabricated $\text{Pt}(\text{Nb}_6)_2$ suggested a combination of Cs^+ and K^+ as counter cations (Figure 4-6).

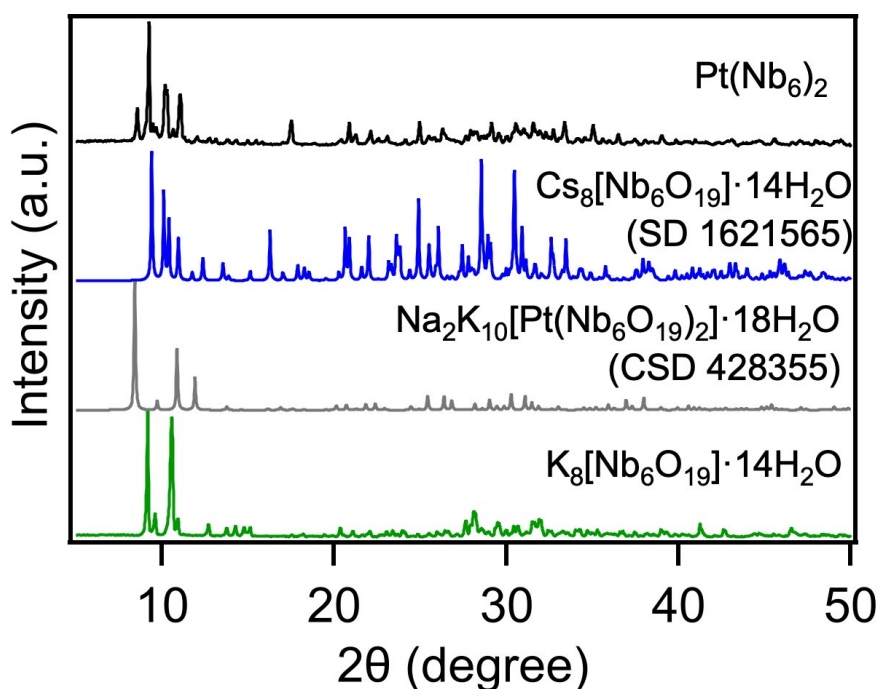


Figure 4-6. XRD patterns of $\text{Pt}(\text{Nb}_6)_2$ compared with references and $\text{K}_8[\text{Nb}_6\text{O}_{19}] \cdot 14\text{H}_2\text{O}$.

IR absorption indicated the vibration corresponding to bridging Nb–O–Nb in the wavenumber regions of $480\text{--}580\text{ cm}^{-1}$ and $620\text{--}790\text{ cm}^{-1}$ and the absorption corresponding to terminal Nb=O_t bonding in wavenumber region of $800\text{--}900\text{ cm}^{-1}$. The formation of sandwich-type structure was observed through the two absorptions in wavenumber region of $620\text{--}790\text{ cm}^{-1}$ indicated by triangle marks (Figure 4-7). The presence of two absorptions instead of one possibly attributed to different bond lengths formed in the sandwich-type structure.

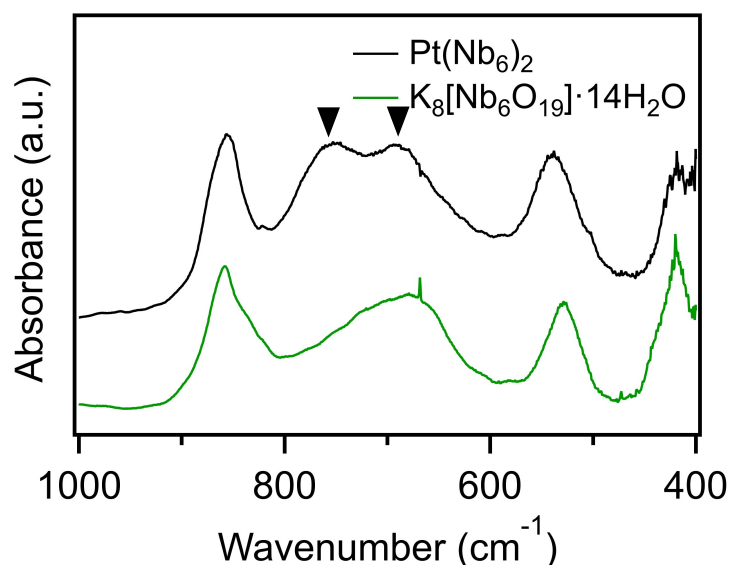


Figure 4-7. FT-IR spectra of $\text{Pt}(\text{Nb}_6)_2$ comparing to $\text{K}_8[\text{Nb}_6\text{O}_{19}] \cdot 14\text{H}_2\text{O}$.

The composition of the cluster was characterized by ESI-MS measured in aqueous solution in negative ion mode. The region of 720–780 Da is enlarged in Figure 4-8b indicating composition of $[\text{Pt}(\text{Nb}_6\text{O}_{19})_2]^{12-}$ with Cs^+ , K^+ , and H^+ as counter cations.

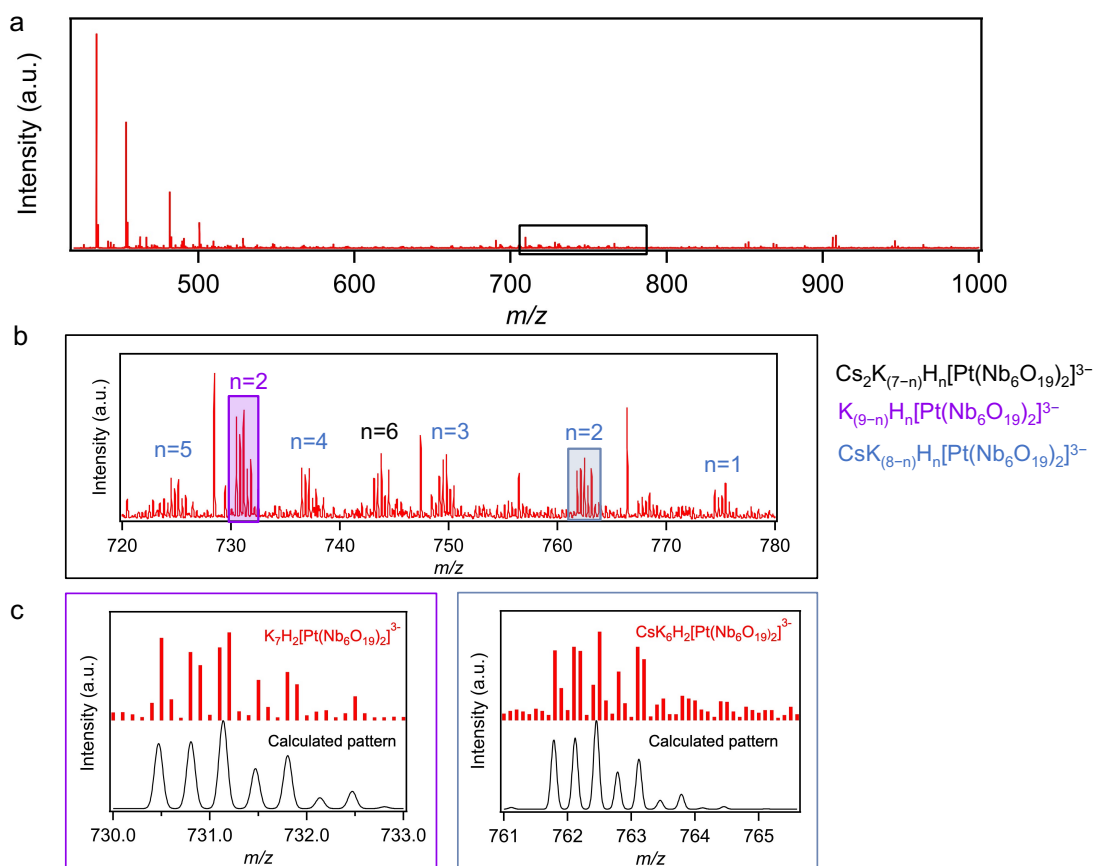


Figure 4-8. ESI-MS spectra of $\text{Pt}(\text{Nb}_6)_2$ measured in negative ion mode in aqueous solution (a) over range of 420–1000 Da with (b) enlarged view in the m/z range of 720–780 Da and (c) the corresponding isotopic patterns measured in negative ion mode in aqueous solution.

The water content and thermal stability of the catalyst were analyzed by TG-DTA under N_2 atmosphere with heating rate of $5^\circ C/min$. The mass loss from $50-70^\circ C$ corresponded to adsorbed water on surface of the catalyst, while the 11.4% mass loss from $70-240^\circ C$ indicated the lattice water content that calculated to be 18 units (Figure 4-9). From this data, $Pt(Nb_6)_2$ could withstand temperature of $200^\circ C$ without significant structural decomposition, which is over the temperature in which the catalytic reaction would be performed.

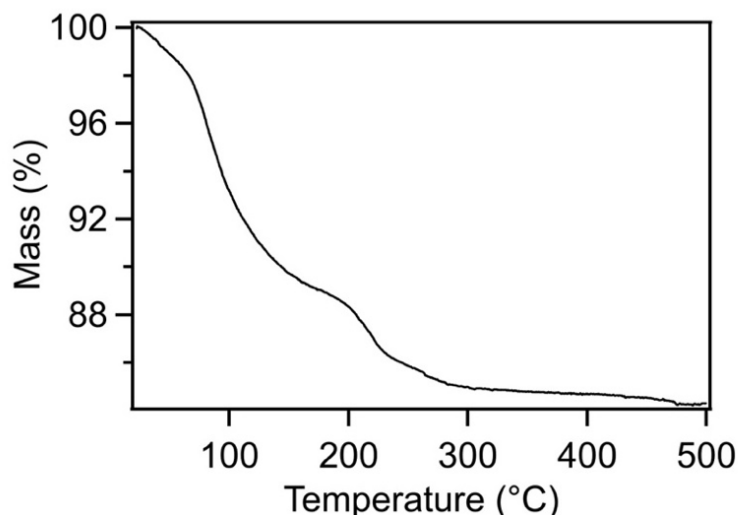


Figure 4-9. TG-DTA of $Pt(Nb_6)_2$ under N_2 atmosphere with heating rate of $5^\circ C/min$.

Further characterization using XAFS were conducted to identify Nb species of the synthesized clusters. The Nb K-edge XAFS results, both pre-edge region of XANES spectra and FT-EXAFS spectra, indicated the similarity between Nb species in the Lindqvist-type precursor, $K_8[Nb_6O_{19}]$, suggesting the Nb species of sandwich-type structure of $Pt(Nb_6)_2$ were based on the Lindqvist-type structure and implying that incorporation of Pt species in the clusters did not deteriorate the Lindqvist-type structure of $[Nb_6O_{19}]^{8-}$ (Figure 4-10).

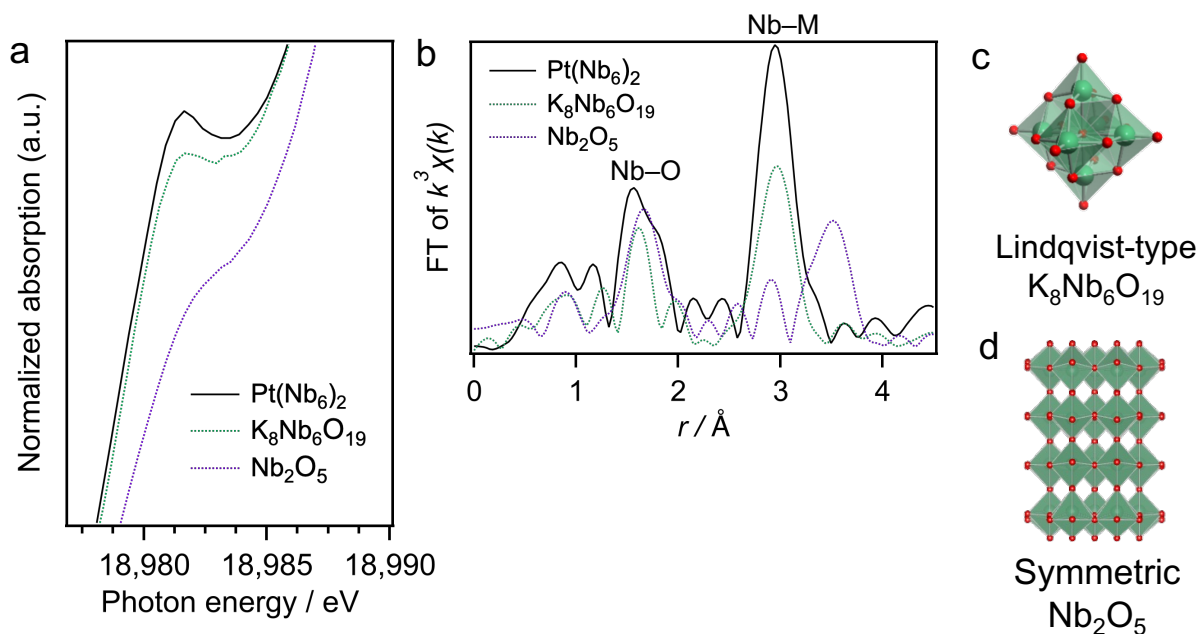


Figure 4-10. Nb K-edge XAS results showing (a) XANES spectra in the pre-edge region, (b) FT-EXAFS spectra, (c) Lindqvist-type K₈Nb₆O₁₉ and (d) symmetric Nb₂O₅. Measurement conditions: crystal Si(311), mirror: 1.5 mrad, gas composition: I₀; N₂ = 50% Ar 50%, I₁; Ar = 75% Kr 25%. The k^3 -weighted EXAFS oscillation in the range of 3–16 Å⁻¹ was Fourier transformed. The data reduction was performed using xTunes software.²⁶

In terms of the Pt species of Pt(Nb₆)₂, Pt L₃-edge XANES spectrum of Pt(Nb₆)₂ was aligned with the Pt precursor, H₂Pt(OH)₆, suggesting ionic state of Pt (Pt⁴⁺) was incorporated into the sandwich-type structure (Figure 4-11a). FT-EXAFS spectra indicated the presence of Pt–M bonding suggesting that a successful bonding of the incorporated Pt species to metal ion rather than free Pt⁴⁺ ion (Figure 4-11b).

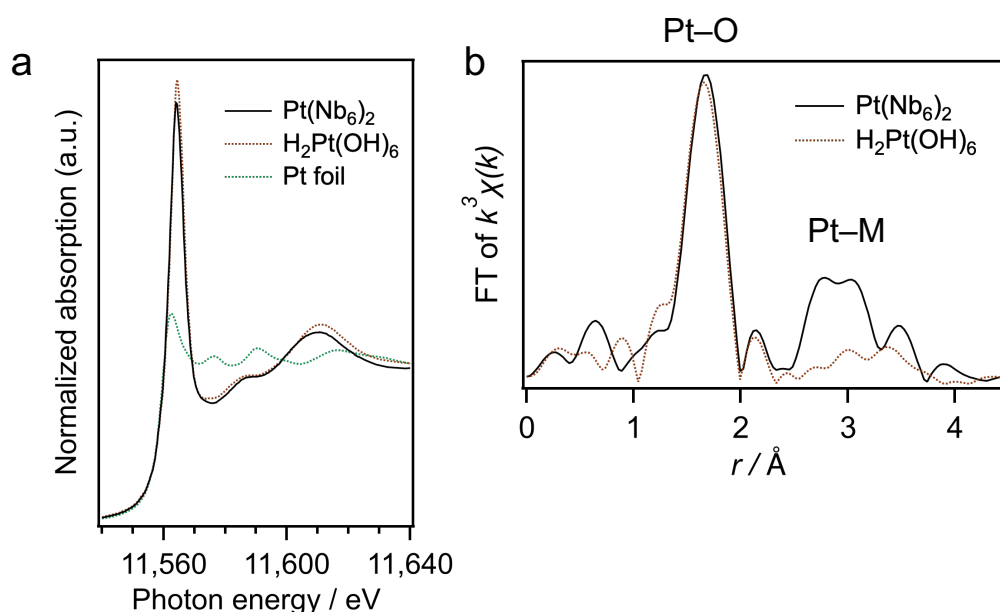


Figure 4-11. Pt L_3 -edge (a) XANES spectra and (b) FT-EXAFS spectra of fresh $\text{Pt}(\text{Nb}_6)_2$ with references. Measurement conditions: crystal Si(111), mirror: 3.0 mrad, ion chamber gas composition I_0 ; $\text{N}_2 = 85\%$, Ar 15% and I_1 ; Ar = 100%. Acronyms: C.N. = coordination number, r = coordination distance, D.W. = Debye-Waller factors. Values in parentheses indicate uncertainties. The k^3 -weighted EXAFS oscillation in the range of 3–14 \AA^{-1} was Fourier transformed. The data reduction was performed using xTunes software.²⁶

After confirmation of the sandwich-type structure and composition of $\text{Pt}(\text{Nb}_6)_2$, it was used as a catalyst for *N*-formylation of amine using CO_2 as a carbonyl source and H_2 as a reducing agent. This reaction was chosen to elucidate the bifunctionality of the $\text{Pt}(\text{Nb}_6)_2$ where Pt would act as a redox catalyst and reacted with H_2 , while CO_2 could be activated by the high basicity of $[\text{Nb}_6\text{O}_{19}]^{8-}$ units. The reaction was conducted over the course of 36 h to observe the changes in the product formation (Figure 4-12). The turn over frequency (TOF) of 1.4 h^{-1} in the first 6 h of reaction suggested that catalytic reaction had been proceeded.

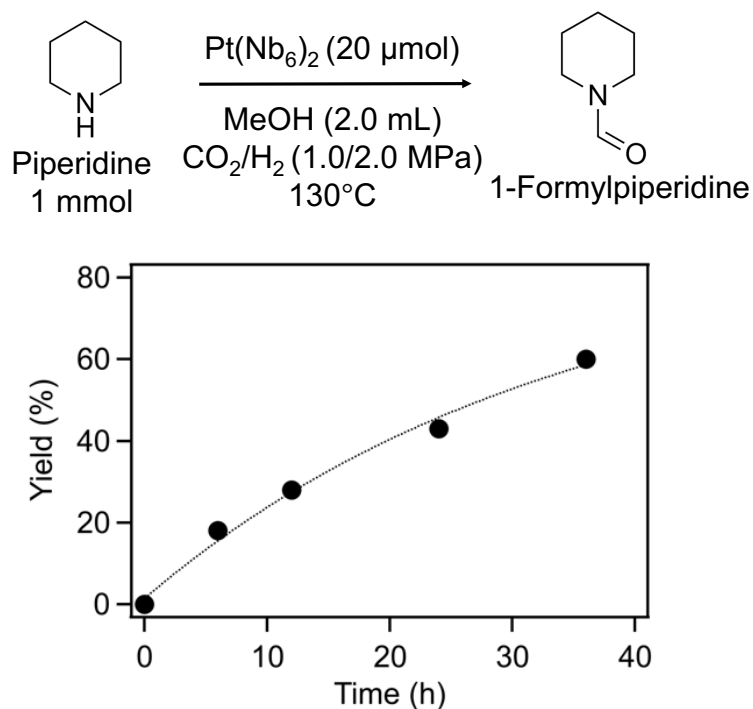


Figure 4-12. Time course result of *N*-formylation of piperidine using $\text{Pt}(\text{Nb}_6)_2$ as the catalyst. Reaction condition: substrate, piperidine (1 mmol); $\text{Pt}(\text{Nb}_6)_2$, 20 μmol ; solvent, MeOH (2 mL); atmosphere: CO_2 (1.0 MPa), H_2 (2.0 MPa); reaction temperature, 130°C.

From the time-course reaction, the reaction time was selected to be 36 h as the optimum reaction time for piperidine as the substrate (Figure 4-13). The result of the *N*-formylation of piperidine promoted by $\text{Pt}(\text{Nb}_6)_2$ at the optimum condition showed 60% yield of 1-formylpiperidine. Other control reactions were conducted to elucidate the function of each component or active site. In the absence of CO_2 , H_2 , Pt species, or $[\text{Nb}_6\text{O}_{19}]^{8-}$ species led to a drastic decrease in the product formation. The reaction promoted by a combination of $\text{K}_8[\text{Nb}_6\text{O}_{19}]$ and $\text{H}_2\text{Pt}(\text{OH})_6$ as the two precursors with the equivalent loading to the sandwich-type $\text{Pt}(\text{Nb}_6)_2$ led to a slightly lower product formation than $\text{Pt}(\text{Nb}_6)_2$ -promoted reaction. This suggested a necessity of a close proximity between Pt species and $[\text{Nb}_6\text{O}_{19}]^{8-}$ species found in the sandwich-type structure rather than physical mixture of the two precursors.

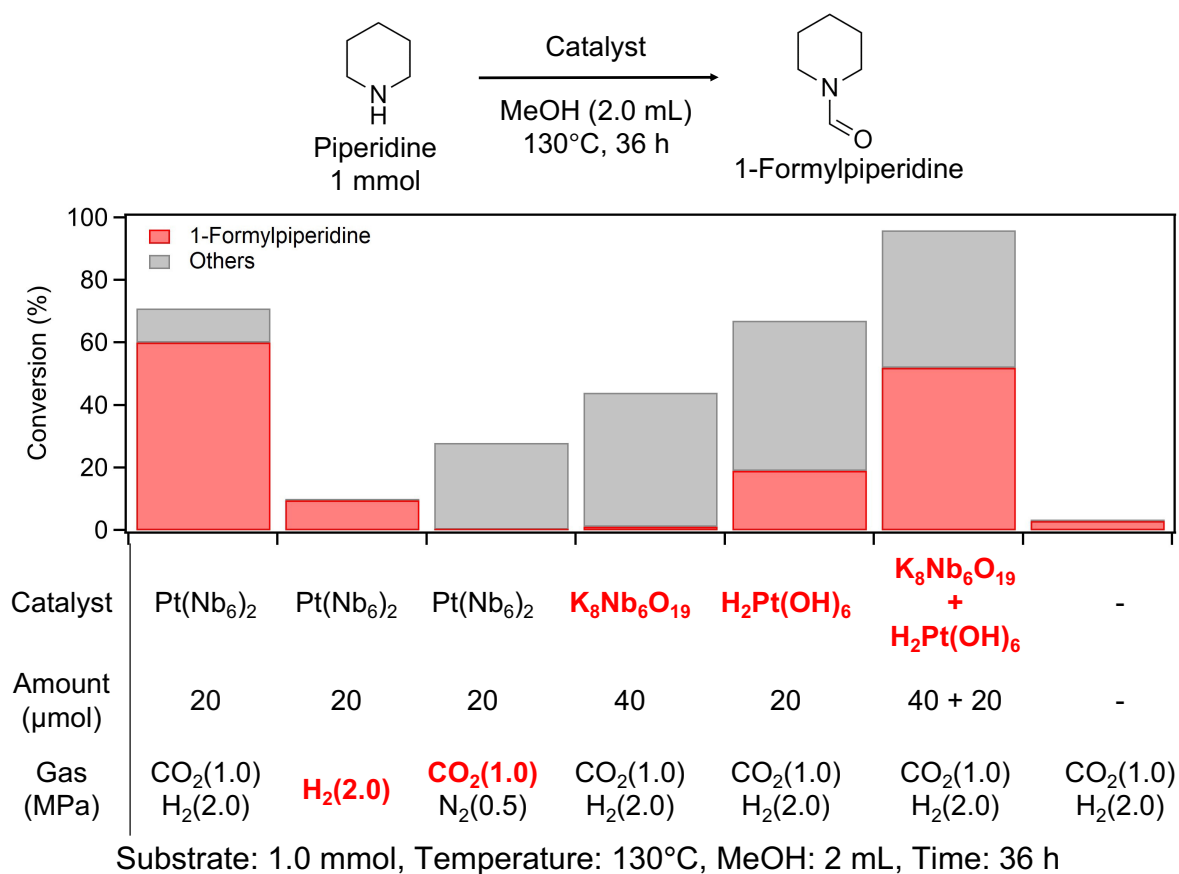


Figure 4-13. The results of *N*-formylation of piperidine at the optimum condition comparing to various conditions. General reaction condition: substrate, piperidine (1 mmol); solvent, MeOH (2 mL); reaction temperature, 130°C; reaction time, 36 h.

The importance of H₂ gas in this system could be related to the activation of Pt species, indicated by the dependency of H₂ partial pressure (Figure 4-14), in which the metallic state of Pt would most likely be the active species responsible for reduction of substrate during the reaction. This finding was consistent to the trace amount of product yield obtained in the reaction promoted Pt(Nb₆)₂ in the presence of CO₂ (1.0 MPa)/N₂ (0.5 MPa) and the reaction promoted by only K₈[Nb₆O₁₉] as the catalyst.

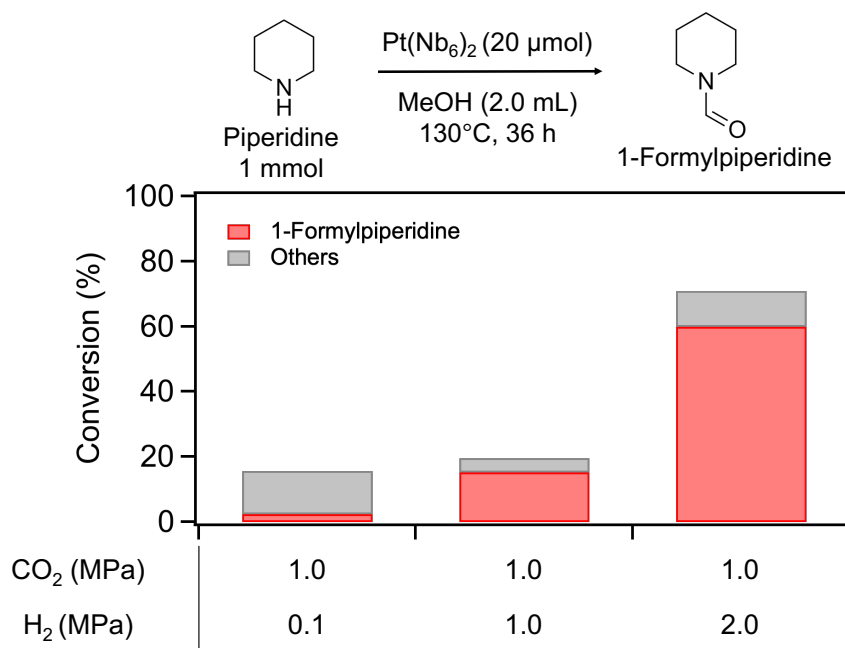


Figure 4-14. Effect of H₂ partial pressure to the catalytic *N*-formylation of piperidine. Reaction condition: substrate, piperidine (1 mmol); Pt(Nb₆)₂ loading, 20 μmol; solvent, MeOH (2 mL); reaction temperature, 130°C; reaction time, 36 h.

When comparing the similar situation for CO₂, the effect of partial pressure of CO₂ to the catalytic activity was lower than that of H₂ (Figure 4-15). For example, when comparing the product yield at low partial pressure (0.1 MPa) of each gas, 0.1 MPa of CO₂ could generated certain amount of product (14%), whereas the condition with 0.1 MPa of H₂ only produced a trace amount of product (2.5%).

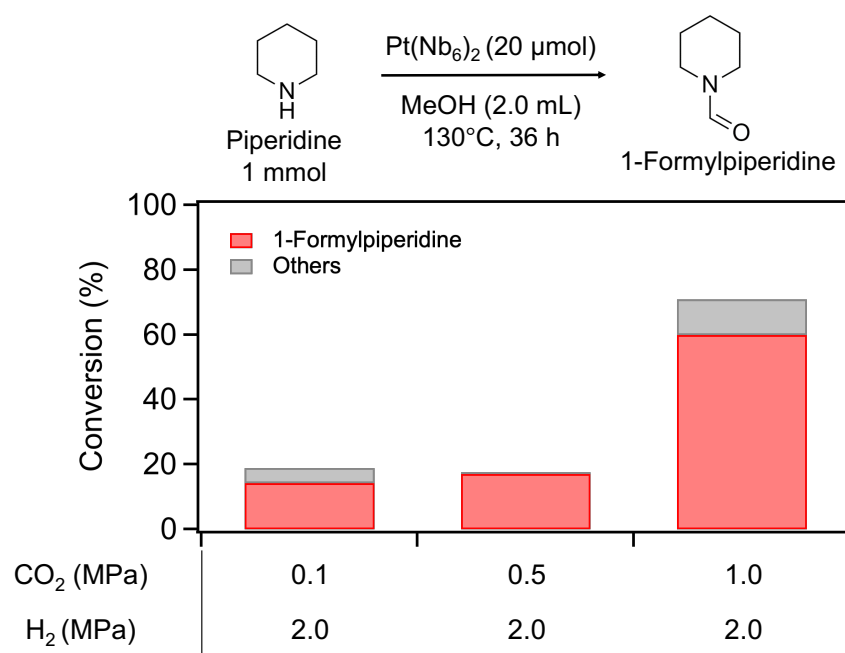


Figure 4-15. Effect of CO₂ partial pressure to the catalytic *N*-formylation of piperidine. Reaction condition: substrate, piperidine (1 mmol); Pt(Nb₆)₂ loading, 20 μmol; solvent, MeOH (2 mL); reaction temperature, 130°C; reaction time, 36 h.

After the reaction, the recovered catalyst exhibited different appearance from the fresh catalyst. Therefore, the characterization of the catalyst after the reaction was conducted to identify the structure as well as electronic states of Pt and Nb. First, XRD pattern of the spent catalyst showed the formation of Pt nanoparticles marked by black triangles in Figure 4-16. The formation of Pt nanoparticles was more obvious with longer reaction time. In addition to formation of Pt nanoparticles, some Nb structure was changed from the fresh catalyst, however, some diffraction patterns at 2θ near 10 degrees could still be observed, suggesting that some Lindqvist-type $[\text{Nb}_6\text{O}_{19}]^{8-}$ clusters could be retained.

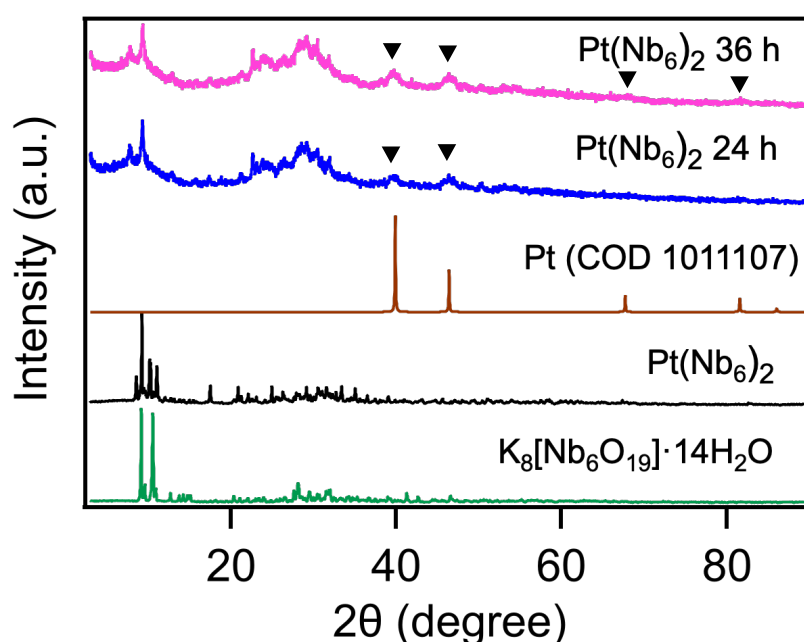


Figure 4-16. XRD of recovered $\text{Pt}(\text{Nb}_6)_2$ catalyst after 36 h and 24 h of reaction comparing to Pt nanoparticle, fresh $\text{Pt}(\text{Nb}_6)_2$, and $\text{K}_8[\text{Nb}_6\text{O}_{19}] \cdot 14\text{H}_2\text{O}$.

To confirm the Lindqvist-type structure of $[\text{Nb}_6\text{O}_{19}]^{8-}$ unit, FT-IR of the spent catalyst was also measured. The characteristic absorptions due to bridging Nb–O–Nb ($480\text{--}580\text{ cm}^{-1}$ and $620\text{--}790\text{ cm}^{-1}$) and terminal Nb=O_t ($800\text{--}900\text{ cm}^{-1}$) could still be observed, indicating the retention of $[\text{Nb}_6\text{O}_{19}]^{8-}$ clusters. However, the new absorption appeared in the wavenumber range of $620\text{--}720\text{ cm}^{-1}$ corresponding to the absorption of $\text{Nb}_2\text{O}_5 \cdot n\text{H}_2\text{O}$ as shown in Figure 4-17, suggesting a formation of other Nb species occurred.

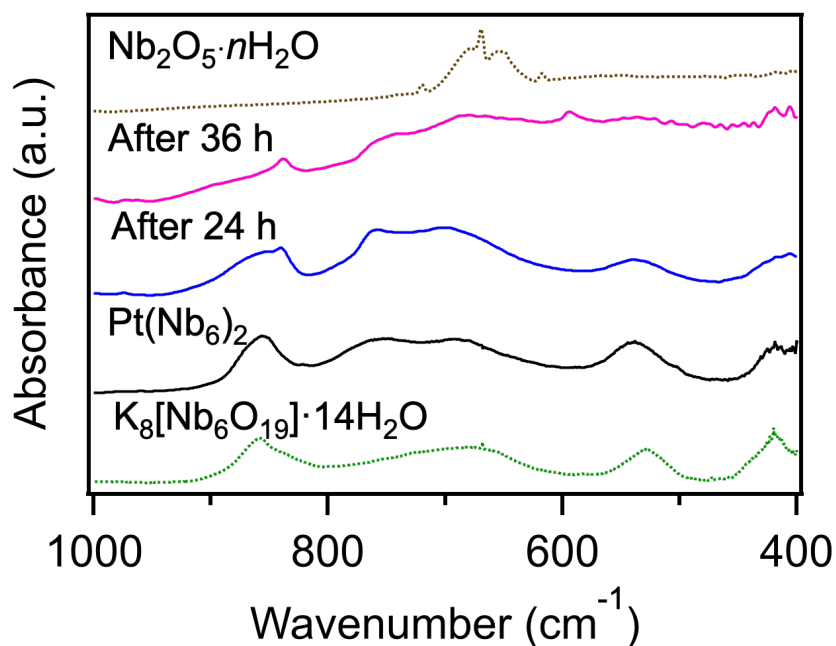


Figure 4-17. FT-IR spectra of $\text{Nb}_2\text{O}_5 \cdot n\text{H}_2\text{O}$ comparing to the spectra of spent $\text{Pt}(\text{Nb}_6)_2$ after 36 and 24 h of reaction, fresh $\text{Pt}(\text{Nb}_6)_2$, and $\text{K}_8[\text{Nb}_6\text{O}_{19}] \cdot 14\text{H}_2\text{O}$.

From XRD results that suggested a formation of Pt nanoparticles, high-resolution TEM images were then taken to confirm and analyze the particle size. The TEM images demonstrated the formation of Pt nanoparticles as observed in black dots. The nanoparticles were enlarged with longer reaction time, with an average size of 2.0 ± 0.7 nm for the catalyst after 24 h of reaction, and 3.4 ± 1.4 nm for the catalyst after 36 h of reaction (Figure 4-18). Moreover, a support material was observed in both cases, which understood to be NbO_x that formed during the reaction condition that also supported by the absorption in FT-IR spectra.

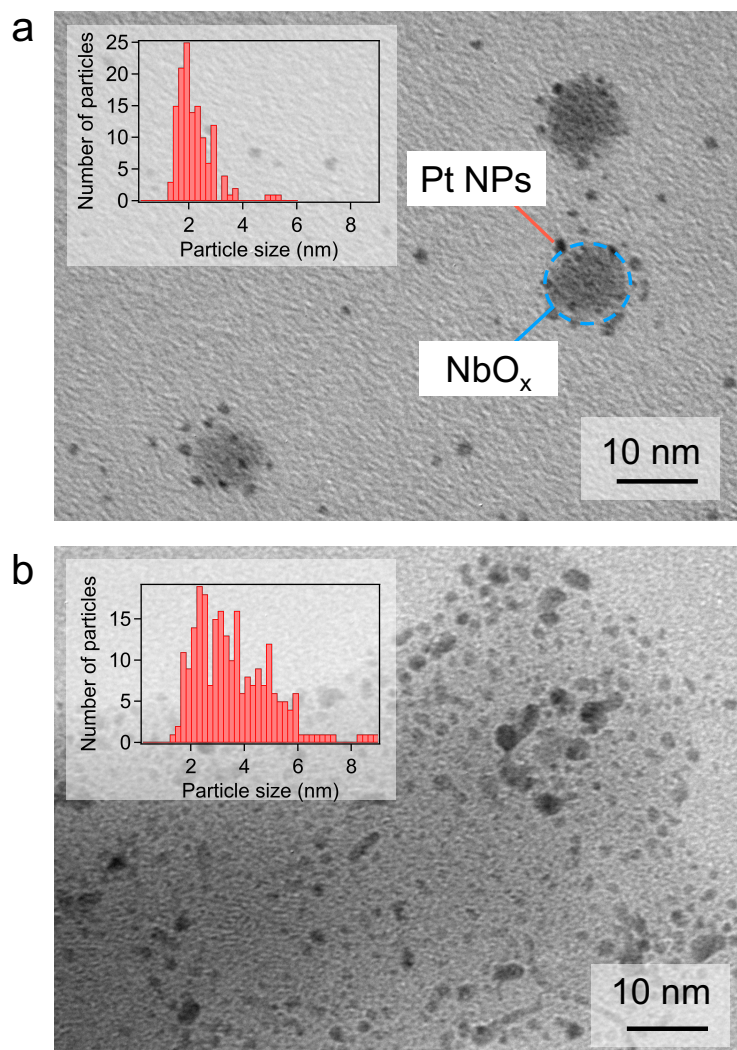


Figure 4-18. TEM images of catalyst after (a) 24 h and (b) 36 h of reaction.

The electronic properties of Nb and Pt species were elucidated by XAFS. In the case of Nb species, pre-edge region of XANES spectra was used to observe the symmetry of the local structure of Nb (Figure 4-19). The high pre-edge absorption intensity is assigned to the distortion of the octahedral (*Oh*) symmetry of MO₆ unit, which is one of the characteristic features of Lindqvist-type [Nb₆O₁₉]⁸⁻. On the other hand, highly symmetric Nb₂O₅ possessed low distortion of the *Oh* symmetry and therefore has low absorption intensity in the pre-edge region. The pre-edge absorption intensity of the catalyst after reaction was lower than fresh catalyst and changed to be similar to that of Nb₂O₅, suggesting the Nb oxide species that generated during the reaction to become the support.

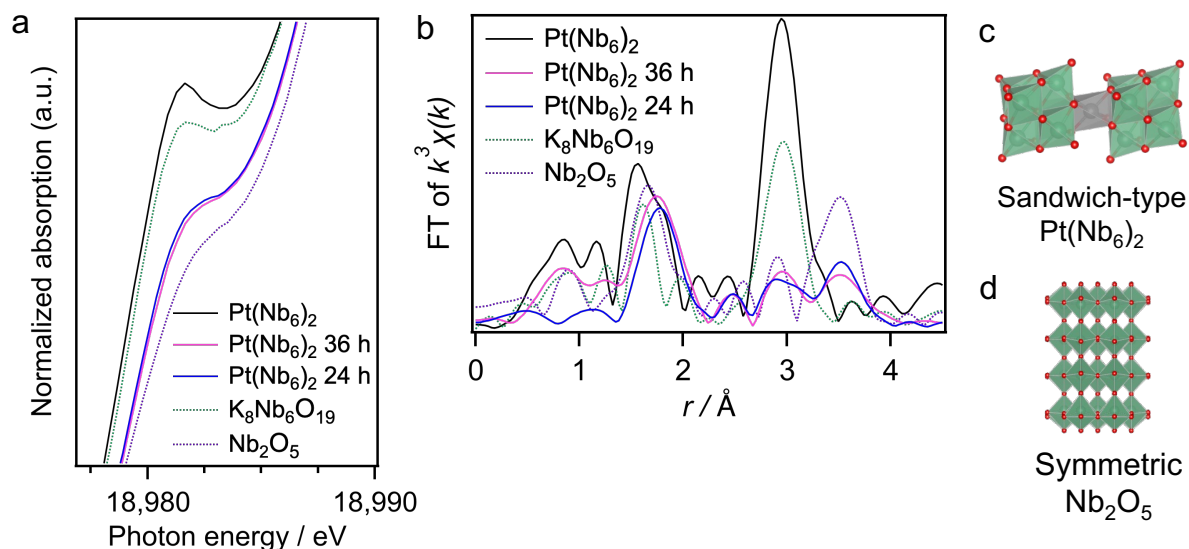


Figure 4-19. Nb K-edge (a) XANES spectra, (b) FT-EXAFS spectra of fresh Pt(Nb₆)₂ comparing to the spent Pt(Nb₆)₂ and references, as well as structures of (c) sandwich-type Pt(Nb₆)₂ and (d) Nb₂O₅. Measurement conditions: crystal Si(311), mirror: 1.5 mrad, gas composition: I₀; N₂ = 50% Ar 50%, I₁; Ar = 75% Kr 25%. The k³-weighted EXAFS oscillation in the range of 3–16 Å⁻¹ was Fourier transformed. The data reduction was performed using xTunes software.²⁶

In the case of Pt species, the results confirmed the formation of Pt nanoparticles suggested by XRD patterns as observed in the white line absorption in XANES spectra (Figure 4-20a) and FT-EXAFS results (Figure 4-20b). In addition, slight increase in the particle size was also estimated by curve fitting analysis indicated by an increase in coordination number (C.N.) of Pt–Pt bonding with longer reaction time (Figure 4-20c).

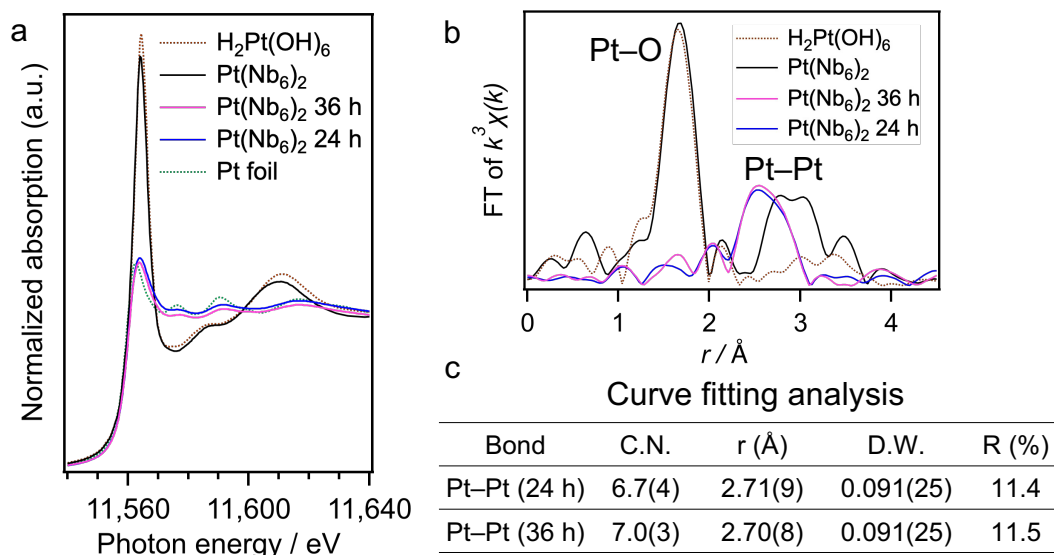


Figure 4-20. Pt L₃-edge (a) XANES spectra and (b) FT-EXAFS spectra of spent catalyst comparing to fresh Pt(Nb₆)₂ and references, as well as (c) curve fitting analysis results of Pt–Pt bonding. Measurement conditions: crystal Si(111), mirror: 3.0 mrad, ion chamber gas composition I₀; N₂ = 85%, Ar 15% and I₁; Ar = 100%. Acronyms: C.N. = coordination number, r = coordination distance, D.W. = Debye-Waller factors. Values in parentheses indicate uncertainties. The k³-weighted EXAFS oscillation in the range of 3–14 Å⁻¹ was Fourier transformed. The data reduction was performed using xTunes software.²⁶ The curve fitting analysis was performed in the range of 2.2–2.9 Å in R space.

From several characterization data, the model of the actual catalyst was proposed. Ionic Pt^{4+} turned into active Pt^0 in the presence of H_2 in the reaction condition, followed by the growth process of nanoparticles to the size of 2–4 nm. The remaining Nb_6 would be aggregated or decorated on the surface of Pt nanoparticles as originally was joint as sandwich-type structure. The idea of attachment on the surface is through the electron donation from the $[\text{Nb}_6\text{O}_{19}]^{8-}$ cluster to the metallic nanoparticles as reported.¹ In addition, some Nb oxide species that formed under reaction condition would result in support material. The resultant catalyst would then be Pt nanoparticles modified by polyoxoniobates supported on Nb oxide (NbPOM-PtNPs/ NbO_x) illustrated in Figure 4-21.

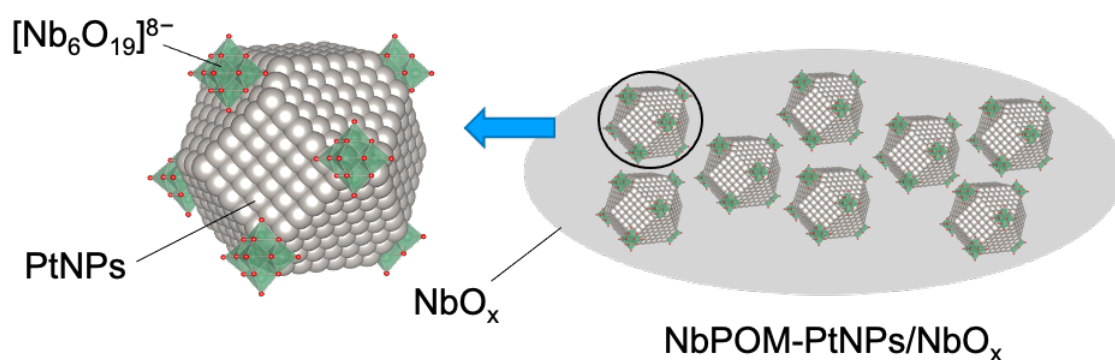


Figure 4-21. Proposed model of NbPOM-PtNPs/ NbO_x generated in-situ that exhibited bifunctional catalysis.

To confirm that the formation of NbPOM-PtNPs/ NbO_x occurred under reaction condition and was not thermal decomposition, the $\text{Pt}(\text{Nb}_6)_2$ was heated under N_2 atmosphere at 130°C and 150°C. After heating, their structures were evaluated by FT-IR comparing to the fresh catalyst (Figure 4-22). The result suggested that the structural change did not occur from thermal decomposition, but rather under the presence of H_2 at high temperature.

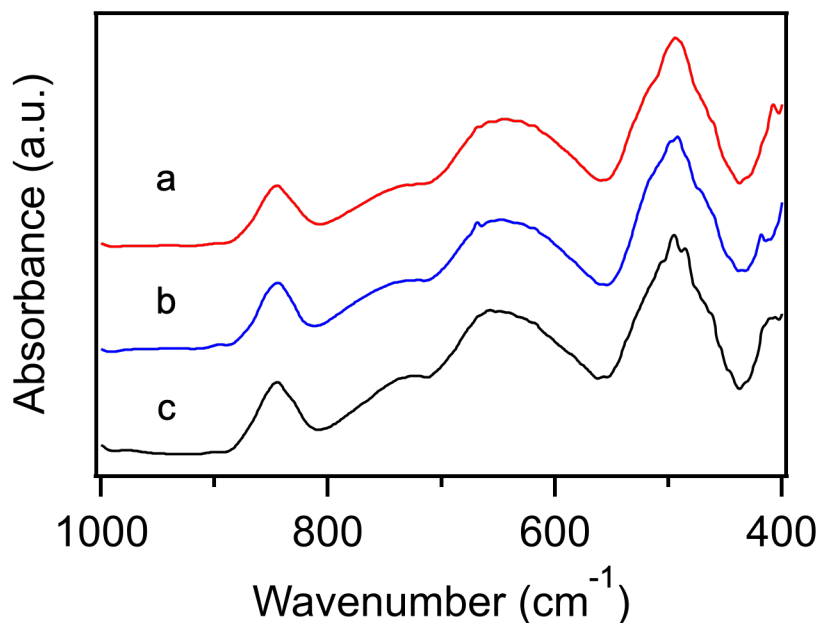
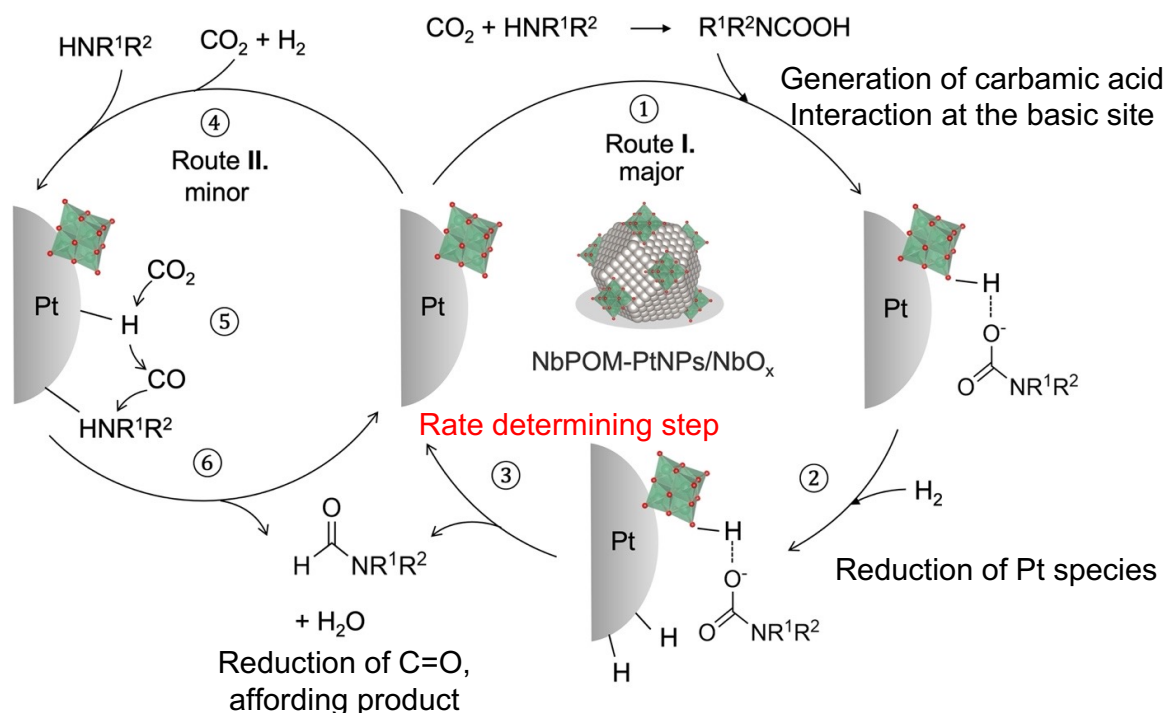


Figure 4-22. FT-IR of the Pt(Nb₆)₂ after heating at (a) 150 °C, (b) 130 °C, and (c) fresh catalyst.

Based on the reaction results and control reactions, the following two plausible pathways were proposed. Route I. in Scheme 4-2 was understood to be the major route that began with a generation of carbamic acid as an intermediate by the interaction of amine with CO₂. The generated carbamic acid was then interacted with [Nb₆O₁₉]⁸⁻ at the basic site, which is the terminal O of the cluster. The second step was the reduction of Pt species to form active metallic species and dissociation of H₂. The third step was the reduction of carbonyl group of the carbamic acid to afford formamide derivative as the product along with water as byproduct. This step was understood to be the rate determining step.



Scheme 4-2. Proposed mechanism of *N*-formylation of amine with two possible pathways. In Route I., carbamic acid would be generated as an intermediate and interacted at the basic site (terminal O atom) of $[\text{Nb}_6\text{O}_{19}]^{8-}$ (step 1), followed by a reduction of Pt species by H_2 (step 2), and the reduction of carbonyl group to afford product (step 3). In Route II., CO_2 , H_2 , and amine would be interacted with the catalyst (step 4), where CO_2 would be reduced to CO by Pt nanoparticles (step 5) and interacted with amine to afford product (step 6).

In Route II., which is the minor pathway where the CO_2 was reduced to CO by Pt nanoparticle followed by direct insertion to amine and resulted in formamide as the product. The formation of CO was detected in the gas phase. Gas phase composition indicated the presence of H_2 , contaminated O_2 , CO_2 and CO after conducting *N*-formylation of piperidine for 24 h (Figure 4-23). The ratio of $\text{H}_2:\text{CO}_2$ was calculated to be 12:1 (1.85 MPa H_2 and 0.15 MPa CO_2). The presence of CO was found to be 0.27% relative to the CO_2 pressure.

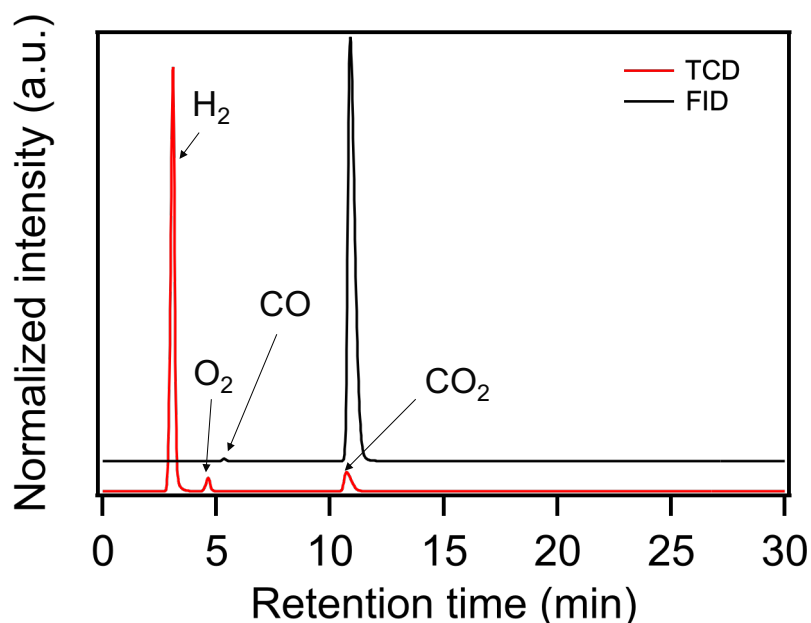
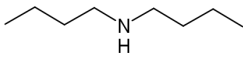
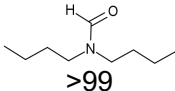
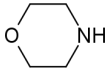
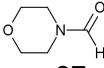
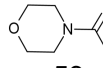
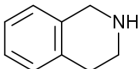
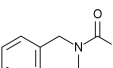
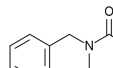
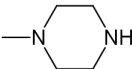
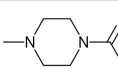
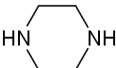
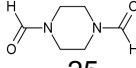
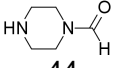


Figure 4-23. Gas phase composition detected after *N*-formylation of piperidine for 24 h.

In order to confirm the proposed mechanism that would be applied to other amines, various secondary amines were used as substrates. Table 4-3 summarized the *N*-formylation reaction results in the presence of Pt(Nb₆)₂ showed significantly higher conversion and product selectivity than the reaction in an absence of the catalyst, thus suggesting the necessity of catalyst to promote the reaction. In the first entry with dibutylamine as the substrate using the same reaction condition with piperidine, decent substrate conversion could be obtained with the desired product obtained as the only product, while in the absence of Pt(Nb₆)₂, the reaction barely proceeded. For entries 2 and 3, dimethylamine (DMA) was used as the solvent instead of MeOH since the reaction using MeOH as the solvent was difficult to proceed. However, the utilization of DMA as the solvent led to a formation of additional products that could be generated from a reaction between substrate and DMA. The reaction between substrate and solvent was also observed when using dimethylformamide (DMF) as the solvent. In that case, the basicity of dimethylformamide promoted the reaction and the difference between the reaction promoted by Pt(Nb₆)₂ and the absence of the catalyst could not be observed. As a result, DMF was not selected as the solvent in this reaction. In the entries 4 and 5, the reaction time was prolonged to 48 h due to improve the catalytic performance, while almost no product formation was detected in the reaction without Pt(Nb₆)₂. The two products were observed in the reaction with piperazine due to the presence of two sites of amino group.

Table 4-3. Substrate scope of *N*-formylation of amines.

Entry	Substrate	Solvent	Reaction time (h)	Conv. (%)	Sel. (%)	
1		MeOH 2 mL	36	62	 >99	
	without Pt(Nb ₆) ₂			4.2	10	
2		DMA 3 mL	48	82	 37	 53
	without Pt(Nb ₆) ₂			51	4.5	39
3		DMA 2 mL	36	50	 66	 34
	without Pt(Nb ₆) ₂			16	7.3	75
4		MeOH 2 mL	48	75	 78	
	without Pt(Nb ₆) ₂			13	<1	
5		MeOH 2 mL	48	86	 25	 44
	without Pt(Nb ₆) ₂			22	n.d.	n.d.

Reaction condition: Substrate, 0.5 mmol; Pt(Nb₆)₂ loading, 20 μmol; reaction temperature, 150 °C; atmosphere: CO₂/H₂ = 1.0/2.0 MPa.

Furthermore, reusability of Pt(Nb₆)₂ was elucidated to observe the catalytic performance after recovery of the catalyst. The results showed the low reusability of the catalyst because of the structural change from sandwich-type Pt(Nb₆)₂ in the first run, while the second and third runs were promoted by the NbPOM-PtNPs/NbO_x that generated during the reaction (Figure 4-24). Nonetheless, the difference of product yield between runs 2 and 3 did not show a drastic change, suggesting that NbPOM-PtNPs/NbO_x exhibited bifunctional catalysis that promoted the reaction in certain extent. From this result, the development of bifunctional catalyst with higher stability could lead to wider application and scalability.

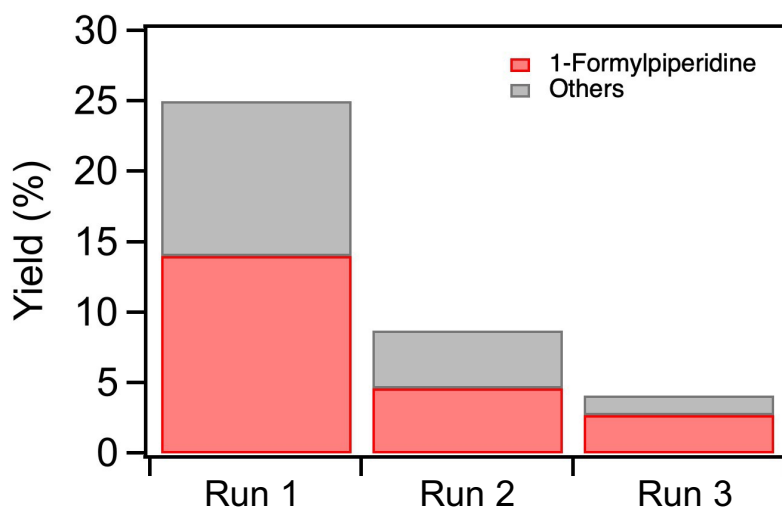
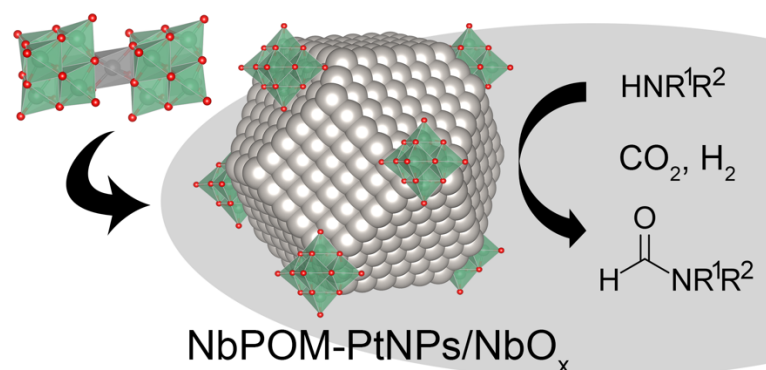


Figure 4-24. Reusability of $\text{Pt}(\text{Nb}_6)_2$ in *N*-formylation of piperidine. Reaction condition: substrate, piperidine (1 mmol); $\text{Pt}(\text{Nb}_6)_2$ loading: 10 μmol solvent, MeOH (2 mL); reaction temperature, 130°C; reaction time, 24 h.

4.4 Conclusions

In this study, sandwich-type Pt-incorporated polyoxoniobates, $\text{Pt}(\text{Nb}_6)_2$ was hypothesized to exhibit bifunctional properties, such as redox and base catalytic properties. The prepared $\text{Pt}(\text{Nb}_6)_2$ was characterized by XRD, FT-IR, ESI-MS, TG-DTA, and XAFS followed by conducting *N*-formylation of piperidine to produce 1-formylpiperidine. The reaction under optimum condition showed that the $\text{Pt}(\text{Nb}_6)_2$ provided superior activity than the precursors, suggesting an importance of the close proximity between Pt species and $[\text{Nb}_6\text{O}_{19}]^{8-}$ species in addition to the presence of CO_2 and H_2 in an appropriate ratio. The characterization of the catalyst after reaction revealed a formation of polyoxoniobate-modified Pt nanoparticles on Nb oxide support ($\text{NbPOM-PtNPs}/\text{NbO}_x$) which exhibit bifunctional catalysis and promoted the *N*-formylation of amine to formamide that cover the secondary amines as the substrate scope. This research provided an insight to the development of bifunctional catalyst as well as the utilization of CO_2 as a carbonyl source to produce value-added chemicals.



Scheme 4-3. Formation of $\text{NbPOM-PtNPs}/\text{NbO}_x$ generated in-situ having bifunctional catalysis in conversion of amine to formamide.

4.5 References

- (1) Kikkawa, S.; Fukuda, S.; Hirayama, J.; Shirai, N.; Takahata, R.; Suzuki, K.; Yamaguchi, K.; Teranishi, T.; Yamazoe, S. *Chem. Commun.* **2022**, 58 (64), 9018–9021.
- (2) Neyman, A.; Meshi, L.; Zeiri, L.; Weinstock, I. A. *J. Am. Chem. Soc.* **2008**, 130 (49), 16480–16481.
- (3) Wang, Y.; Neyman, A.; Arkhangelsky, E.; Gitis, V.; Meshi, L.; Weinstock, I. A. *J. Am. Chem. Soc.* **2009**, 131 (47), 17412–17422.
- (4) Wang, Y.; Weinstock, I. A. *Dalton Trans.* **2010**, 39 (27), 6143.
- (5) Wang, Y.; Zeiri, O.; Sharet, S.; Weinstock, I. A. *Inorg. Chem.* **2012**, 51 (14), 7436–7438.
- (6) Leiser, S. S.; Polin, L.; Gan-Or, G.; Raula, M.; Weinstock, I. A. *Inorg. Chem.* **2019**, 58 (2), 1012–1015.
- (7) Mitsudome, T.; Mikami, Y.; Matoba, M.; Mizugaki, T.; Jitsukawa, K.; Kaneda, K. *Angew. Chem. Int. Ed.* **2012**, 51 (1), 136–139.
- (8) Hirano, T.; Uehara, K.; Kamata, K.; Mizuno, N. *J. Am. Chem. Soc.* **2012**, 134 (14), 6425–6433.
- (9) Kobayashi, K.; Nagato, S.; Kawakita, M.; Morikawa, O.; Konishi, H. *Chem. Lett.* **1995**, 24 (7), 575–576.
- (10) Gall, M.; McCall, J. M.; TenBrink, R. E.; VonVoigtlander, P. F.; Mohrland, J. S. *J. Med. Chem.* **1988**, 31 (9), 1816–1820.
- (11) Pouessel, J.; Jacquet, O.; Cantat, T. *ChemCatChem* **2013**, 5 (12), 3552–3556.
- (12) Ganapati Reddy, P.; Kishore Kumar, G. D.; Baskaran, S. *Tetrahedron Lett.* **2000**, 41 (47), 9149–9151.
- (13) Li, H.; Dong, K.; Neumann, H.; Beller, M. *Angew. Chem. Int. Ed.* **2015**, 54 (35), 10239–10243.
- (14) Liu, H.; Laurency, G.; Yan, N.; Dyson, P. J. *Chem Commun* **2014**, 50 (3), 341–343.
- (15) Schmid, L.; Canonica, A.; Baiker, A. *Appl. Catal. Gen.* **2003**, 255 (1), 23–33.
- (16) Yu, Z.; Li, Z.; Zhang, L.; Zhu, K.; Wu, H.; Li, H.; Yang, S. *Green Chem.* **2021**, 23 (16), 5759–5765.
- (17) Li, W.; Zhu, D.; Li, G.; Chen, J.; Xia, J. *Adv. Synth. Catal.* **2019**, 361 (22), 5098–5104.
- (18) Gopakumar, A.; Lombardo, L.; Fei, Z.; Shyshkanov, S.; Vasilyev, D.; Chidambaram, A.; Stylianou, K.; Züttel, A.; Dyson, P. J. *J. CO₂ Util.* **2020**, 41, 101240.
- (19) Shi, F.; Deng, Y.; SiMa, T.; Peng, J.; Gu, Y.; Qiao, B. *Angew. Chem. Int. Ed.* **2003**, 42 (28), 3257–3260.
- (20) Srivastava, R.; Srinivas, D.; Ratnasamy, P. *J. Catal.* **2005**, 233 (1), 1–15.
- (21) Shang, J.; Guo, X.; Li, Z.; Deng, Y. *Green Chem.* **2016**, 18 (10), 3082–3088.
- (22) Ju, P.; Chen, J.; Chen, A.; Chen, L.; Yu, Y. *ACS Sustain. Chem. Eng.* **2017**, 5 (3), 2516–2528.
- (23) Zhang, Y.; Wang, H.; Yuan, H.; Shi, F. *ACS Sustain. Chem. Eng.* **2017**, 5 (7), 5758–5765.
- (24) Abramov, P. A.; Vicent, C.; Kompankov, N. B.; Gushchin, A. L.; Sokolov, M. N. *Chem. Commun.* **2015**, 51 (19), 4021–4023.
- (25) Momma, K.; Izumi, F. *J. Appl. Crystallogr.* **2011**, 44 (6), 1272–1276.
- (26) Asakura, H.; Yamazoe, S.; Misumi, T.; Fujita, A.; Tsukuda, T.; Tanaka, T. *Radiat. Phys. Chem.* **2020**, 175, 108270.

4.6 Appendix

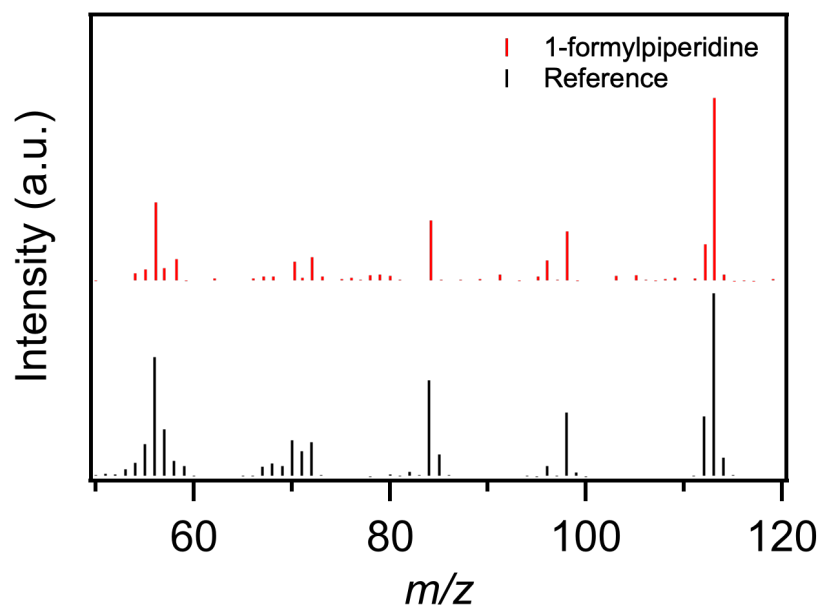


Figure S4-1. GC-MS pattern of 1-formylpiperidine as a result of *N*-formylation of piperidine and reference.

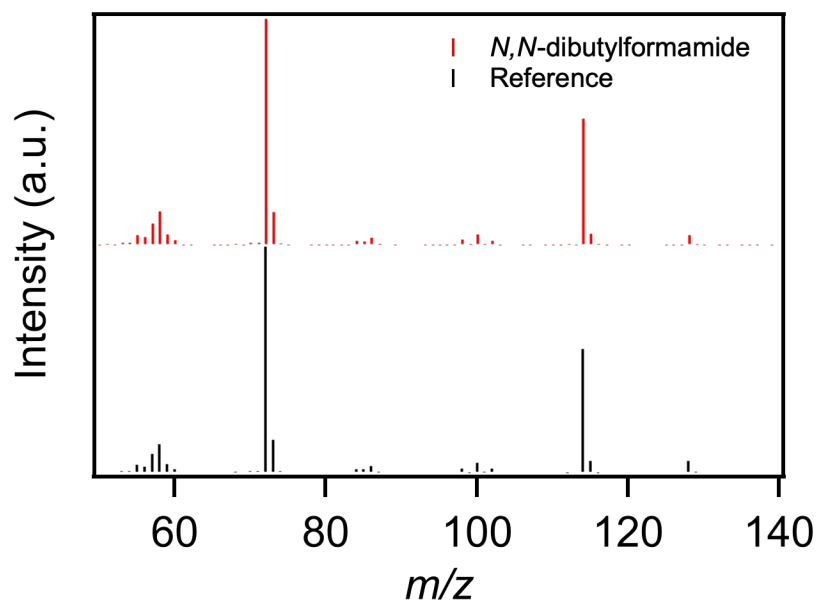


Figure S4-2. GC-MS pattern of *N,N*-dibutylformamide as a result of *N*-formylation of dibutylamine and reference.

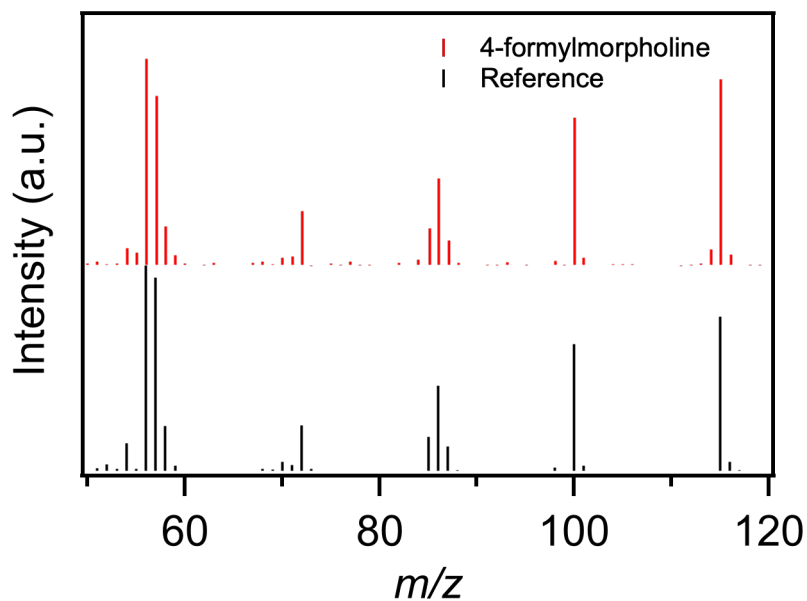


Figure S4-3. GC-MS pattern of 4-formylmorpholine as a result of *N*-formylation of morpholine and reference.

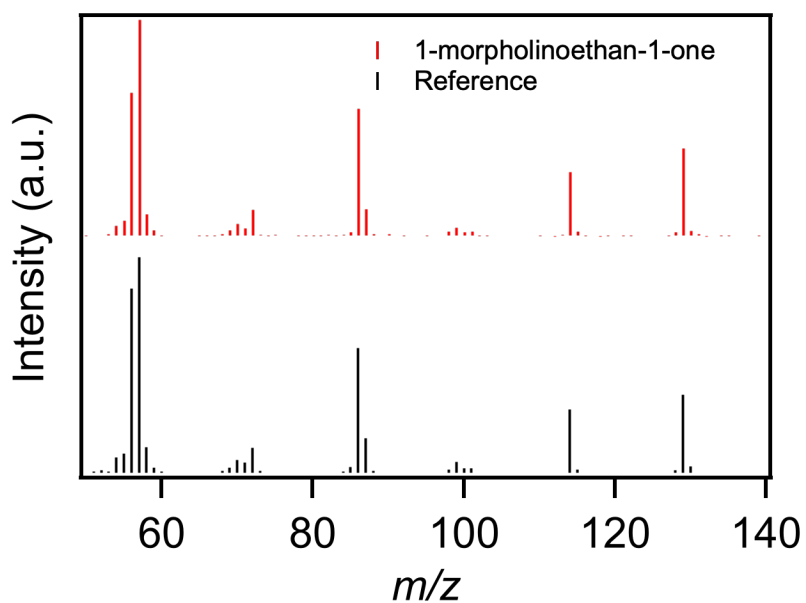


Figure S4-4. GC-MS pattern of 1-morpholinoethan-1-one as a result of *N*-formylation of morpholine and reference.

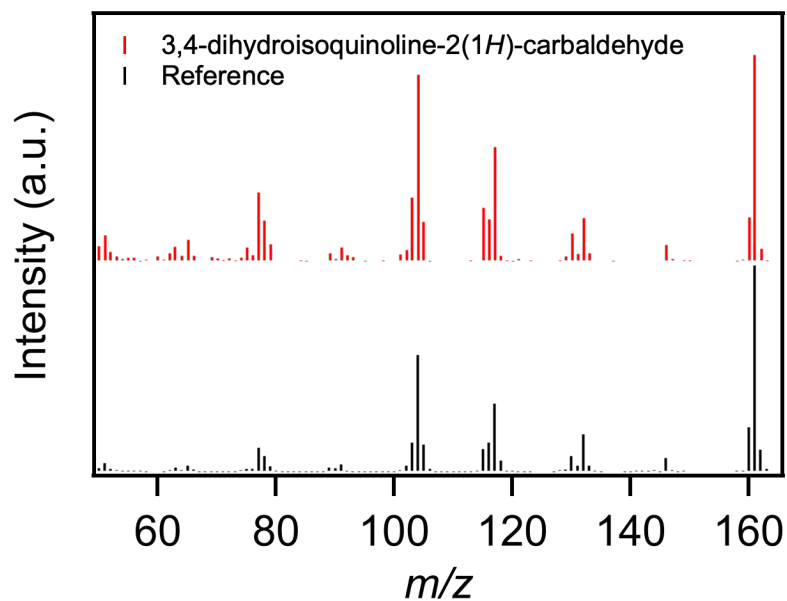


Figure S4-5. GC-MS pattern of 3,4-dihydroisoquinoline-2(1H)-carbaldehyde as a result of *N*-formylation of 1,2,3,4-tetrahydroisoquinoline and reference.

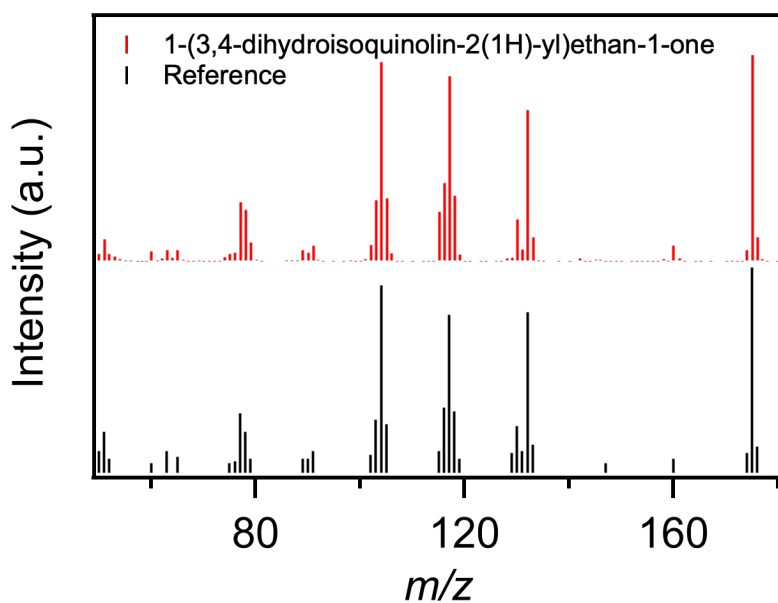


Figure S4-6. GC-MS pattern of 1-(3,4-dihydroisoquinolin-2(1H)-yl)ethan-1-one as a result of *N*-formylation of 1,2,3,4-tetrahydroisoquinoline and reference.

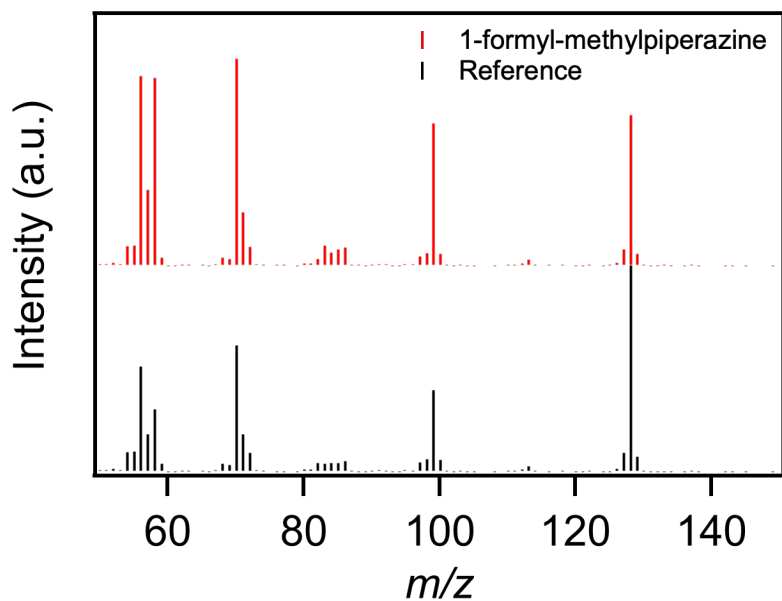


Figure S4-7. GC-MS pattern of 1-formyl-methylpiperazine as a result of *N*-formylation of 1-methylpiperazine and reference.

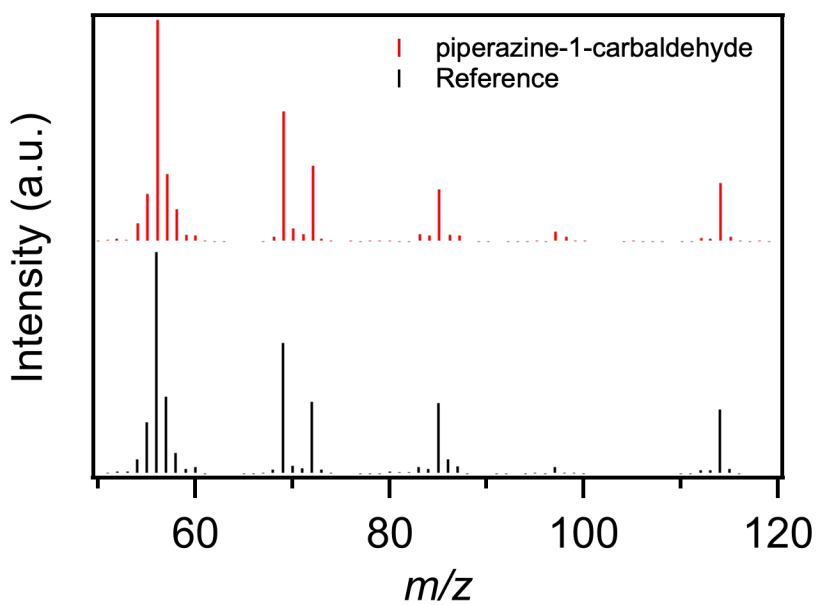


Figure S4-8. GC-MS pattern of piperazine-1-carbaldehyde as a result of *N*-formylation of piperazine and reference.

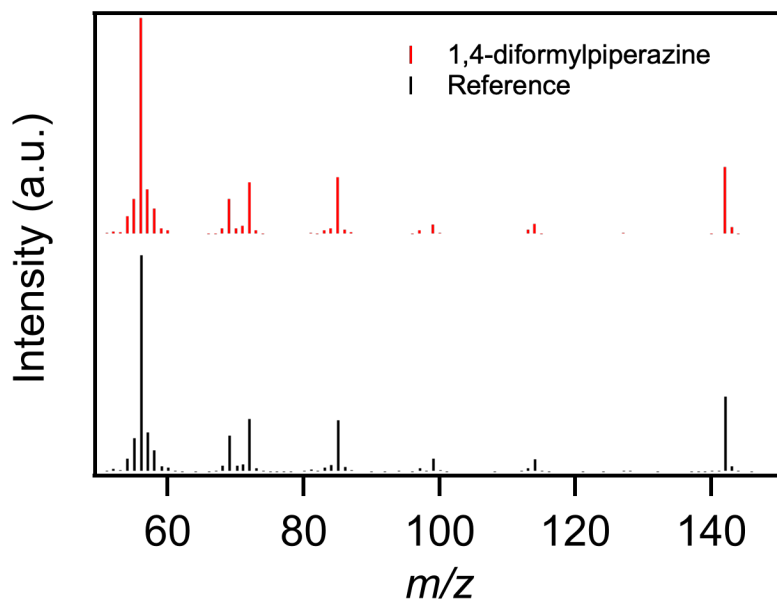


Figure S4-9. GC-MS pattern of 1,4-diformylpiperazine as a result of *N*-formylation of piperazine and reference.

Chapter 5: Concluding remarks

This dissertation covered the key developments of metal oxide clusters, especially involving Nb and Ta as metals in Lindqvist-type and its derivative, since the study on these materials is still in an early stage. Nb- and Ta-containing clusters exhibit high basicity due to the highly negative charge of the clusters, the application of metal oxide clusters as base catalysts were thus promising.

One of the well-known catalytic reactions that is employed to elucidate Brønsted basicity of catalyst is Knoevenagel condensation. In this study, Knoevenagel condensation reactions between benzaldehyde and nitriles with high pK_a values were conducted. Since pK_a value of nitriles tested was up to 23.8, it would be interesting to find the potential of the basicity by using higher pK_a value of the substrate, therefore, aldol condensation between benzaldehyde and ketones were chosen. These two reactions involve the ability of the basic sites of the catalyst, which are surface O atoms, to abstract β -proton of a substrate. Several ketones were employed as substrates and the result indicated that tetrabutylammonium (TBA) salt of $[\text{Nb}_6\text{O}_{19}]^{8-}$ ($\text{TBA}_6\text{H}_2[\text{Nb}_6\text{O}_{19}]$ or TBA-Nb₆) exhibited pK_a value of 29.0 that could be classified as superbase catalyst. This report was the first finding of superbase property in the field of metal oxide clusters or polyoxometalates (Figure 5-1). Another important finding from this study was the effect of synthetic method to the resultant catalyst, where microwave-assisted hydrothermal reaction provided higher efficiency and contain higher TBA cation units which could be decomposed during long reaction time in conventional hydrothermal reaction. The catalytic performance was also improved with the TBA-Nb₆ synthesized by microwave-assisted method comparing to reported pK_a value of 23.8 for TBA-Nb₆ synthesized by conventional method.

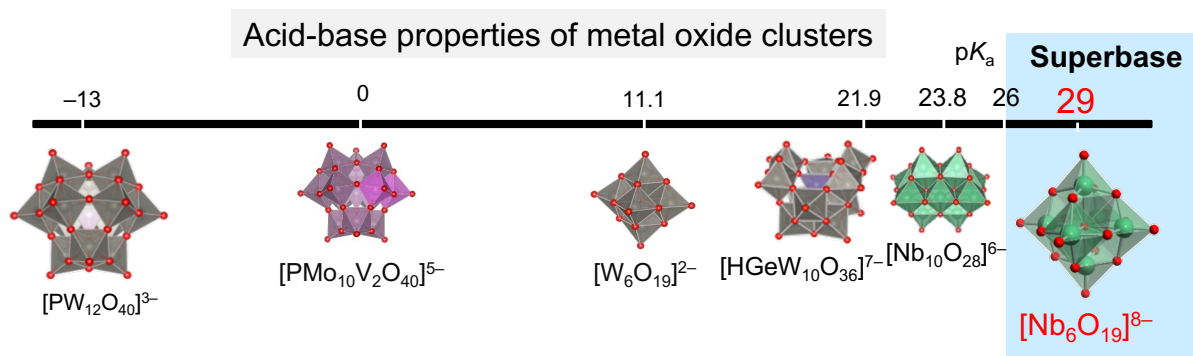


Figure 5-1. The superbase property of $[\text{Nb}_6\text{O}_{19}]^{8-}$ was reported in this study.

In addition to superbase catalytic property, water tolerance was also another feature that makes metal oxide clusters stand out from the solid base catalysts. Thus far, the base catalyst that could tolerate the presence of water would be layered double hydroxides, however, their base strength is not in the range of superbase ($pK_a > 26$). This study, additional water was added to the reaction to observe the effect to the catalytic performance. It was found that the catalytic performance could be retained for condensation reaction of benzaldehyde and nitriles with pK_a value up to 23.8. Although a slight decrease in conversion of the substrate occurred with substrate with pK_a value over 26.5, the changes were not so significant comparing to the results using MgO, which is a well-known solid base, as the catalyst. These findings reported in Chapter 2 could benefit the further study of superbase catalytic properties of other metal oxide clusters as well as potential utilization as catalysts in biomass conversion which require high water tolerance of the catalyst.

Not only Brønsted basicity that metal oxide clusters possess, but their Lewis basicity was also resulted in catalytic application such as CO₂ fixation reaction by utilizing CO₂ as a carbonyl source to react with substrate to form value-added chemicals. Strong base catalyst is required to activate stable CO₂ in order to form nucleophilic species for further reaction. This study focused on using Lindqvist-type metal oxide clusters (metal = Nb, Ta) as catalysts. The model reaction chosen to study was CO₂ fixation to styrene oxide (**SO**) to form styrene carbonate (**SC**). From the catalytic performance comparing between TBA-Ta₆ and TBA-Nb₆ showed different strength and weakness of each type of cluster. TBA-Ta₆ contained high basicity and provided high conversion of **SO**, while providing low selectivity of **SC**. On the other hand, TBA-Nb₆-promoted reaction showed high selectivity of **SC** but due to its lower base strength than TBA-Ta₆, the conversion of **SO** was low. To combine the advantages of the two pristine clusters, using mixed Ta-Nb clusters was proposed to be one of the solutions. Previously reported on using sodium salts of mixed Ta-Nb clusters as heterogeneous catalysts indicated different conversion of substrate in Knoevenagel condensation according to the base strength of each cluster. Therefore, in this study, TBA salts of mixed Ta-Nb clusters were prepared to be used as catalysts in CO₂ fixation to **SO** as homogeneous catalysts. The reaction results over 6 h demonstrated increasing conversion of substrate with higher Ta content, hence higher base strength. However, the highest selectivity to **SC** was achieved by using TBA-Ta₁Nb₅ as the catalyst. The reaction was prolonged to 24 h where the high conversion comparable to TBA-Ta₆, while the high selectivity could be maintained. As a result, TBA-Ta₁Nb₅ was the most promising candidate to achieve high **SC** selectivity as the objective of this study. The reason behind such result was supported by XAFS studies and theoretical

calculations. Pre-edge absorption of Nb-K edge and Ta-L₁ edge were used as tools to identify substrate adsorption and activation. The results indicated that terminal O coordinated to Nb (O_{Nb}), or the basic site of Nb, would activate only CO₂. On the other hand, terminal O coordinated to Ta (O_{Ta}), or the basic site of Ta, would activate both CO₂ and SO. In order to achieve high SC selectivity, activation of CO₂ while suppressing activation of SO is required. Therefore, TBA-Ta₁Nb₅ with only one Ta basic site, which has the preferential activation of CO₂ than SO, while the presence of other Nb basic sites suppressed the activation of SO and resulted in high SC selectivity. Thus, the work reported in Chapter 3 signified the importance of Ta substitution into TBA-Nb₆ cluster to improve the basicity for CO₂ activation while avoiding the activation of substrate by limiting the number of Ta units in the clusters that resulted in high SC selectivity (Figure 5-2).

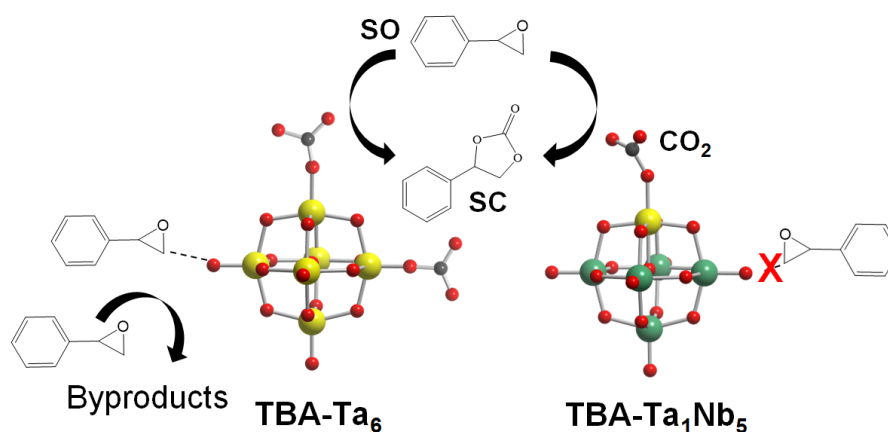


Figure 5-2. The illustration comparing the catalytic activity involved for TBA-Ta₆ and TBA-Ta₁Nb₅ in CO₂ fixation to SO.¹

In Chapter 4, the bifunctional catalysis obtained as a result of Pt incorporation to polyoxoniobates, Pt(Nb₆O₁₉)₂¹²⁻, as a sandwich-type structure was elucidated. From the design of the catalyst that was reported, its potential application suggested was electrochemical application due to the several redox states of the catalyst.² However, its application as bifunctional catalyst was not reported. To evaluate the hypothesis of bifunctional catalysis provided by Pt as a redox catalyst and [Nb₆O₁₉]⁸⁻ units as base catalyst, a reaction which require an activation of two different substrates was selected as a model study. Initially, an attempt to elucidate bifunctional catalysis of Pt(Nb₆)₂ was conducted through simultaneous hydrogenation and CO₂ conversion reaction to obtain urea from cyclic amine. However, the simultaneous reaction was not successful, where only hydrogenation of nitro compounds to obtain amines was conducted. After reviewing potential reaction, *N*-formylation of amine has been successfully promoted by noble metals such as Au and Pd under CO₂ and H₂ atmosphere,

which would be more ideal than using phosgene or CO as carbonyl source and organic silicone as reducing agents. The reaction was thus selected using piperidine as a model substrate. The reaction was proceeded by using $\text{Pt}(\text{Nb}_6)_2$ as the catalyst without addition of external base, suggesting that this catalyst exhibited bifunctional catalysis including redox and base catalysis. After the reaction, the recovered catalyst has different physical appearance from the fresh catalyst. Therefore, a detailed characterization of the catalyst after undergoing reaction condition was performed. The results from several characterization methods were analyzed and the model of the actual catalyst was proposed to be Pt nanoparticles decorated by polyoxoniobates on niobium oxide support ($\text{NbPOM-PtNPs}/\text{NbO}_x$). This finding indicated a formation of active species during the reaction or in-situ generation that is common for metal ions to be reduced by H_2 to form metallic species that could function as a redox catalyst. The in-situ formation of this catalyst thus showed the higher activity than the physical mixture of the two precursors used to fabricate the $\text{Pt}(\text{Nb}_6)_2$, which could be attributed to the proximity between redox and basic sites. In order to understand the mechanism of this catalytic system, several blank tests were conducted to identify the role of each active species and intermediate that formed and drove the reaction. From the hypothesis that $[\text{Nb}_6\text{O}_{19}]^{8-}$ possessing high basicity for CO_2 activation as shown in the reaction results in Chapter 3, the role of base catalysis proposed in Chapter 4 was different due to a plausible route of carbamic acid generation that easily formed by reaction between amine and CO_2 . The basicity of $[\text{Nb}_6\text{O}_{19}]^{8-}$ clusters therefore assisted the interaction with carbamic acid generated. Finally, the substrate scope of this catalyst was investigated by conducting the reaction using several secondary amines. The study in Chapter 4 provided an insight in development of bifunctional catalyst and expanded the utilization of CO_2 as carbonyl source in preparation of value-added chemicals (Figure 5-3).

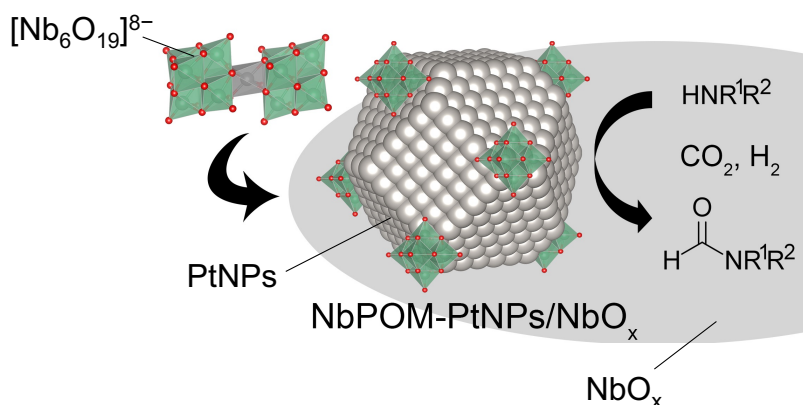


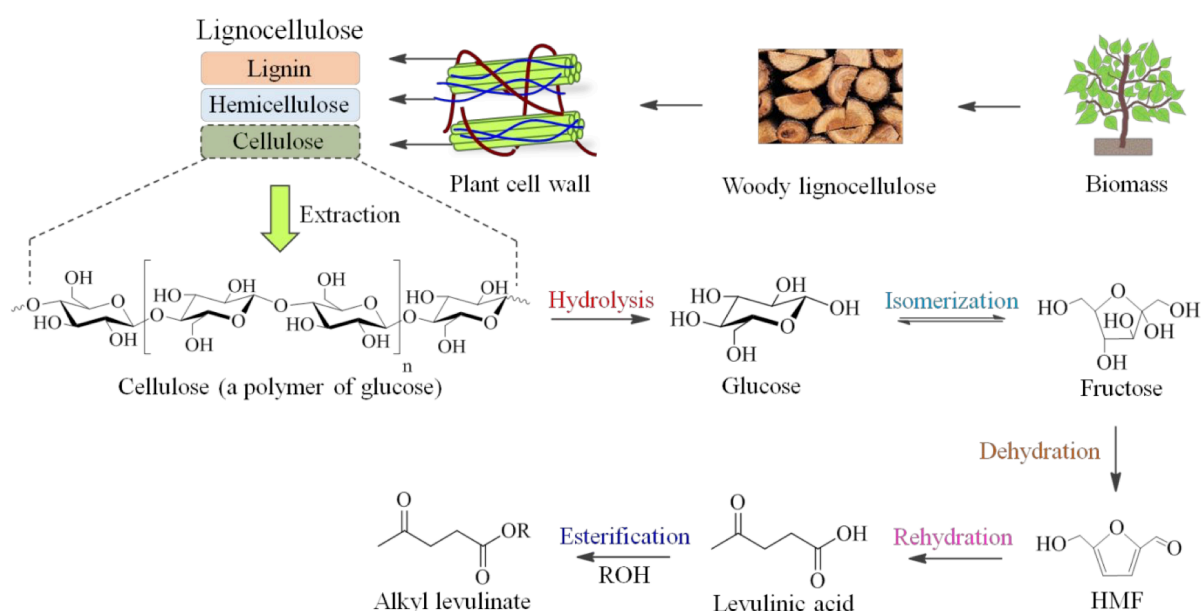
Figure 5-3. The proposed model of the Pt nanoparticles modified by polyoxoniobates on niobium oxide support ($\text{NbPOM-PtNPs}/\text{NbO}_x$) responsible for *N*-formylation of amine to formamide under CO_2 and H_2 atmosphere.³

References

- (1) Chudatemiya, V.; Tsukada, M.; Nagakari, H.; Kikkawa, S.; Hirayama, J.; Nakatani, N.; Yamamoto, T.; Yamazoe, S. *Catalysts* **2023**, *13* (2), 442.
- (2) Abramov, P. A.; Vicent, C.; Kompankov, N. B.; Gushchin, A. L.; Sokolov, M. N. *Chem. Commun.* **2015**, *51* (19), 4021–4023.
- (3) Chudatemiya, V.; Kikkawa, S.; Hirayama, J.; Takahata, R.; Teranishi, T.; Tamura, M.; Yamazoe, S. *Asian J. Org. Chem.* **2022**.

Chapter 6: Future prospects

From the studies reported in this dissertation, $\text{TBA}_6\text{H}_2[\text{Nb}_6\text{O}_{19}]$ (TBA-Nb₆) has shown superb catalytic property where it could abstract proton from ketone with $\text{p}K_{\text{a}}$ value of 29.0. Moreover, TBA-Nb₆ also exhibits water tolerance where the catalytic performance could be maintained in the presence of water in the system. Therefore, the high and controllable basicity provided by the cluster accompanied with high water tolerance led to a potential application for biomass conversion reactions. In biomass conversions, water or aqueous solutions of ketones and aldehydes would be presented in the system that could poison the active sites of the catalysts without water tolerance.^{1,2} Generally, acid-base catalysts would be used to promote the conversion of biomass to carbohydrate derivatives presented in Scheme 6-1.³



Scheme 6-1. General reaction scheme to convert biomass to carbohydrates by TiO_2 as acid catalyst where water is presence in the system.³

According to higher negative NBO charges of $[\text{Ta}_6\text{O}_{19}]^{8-}$ than those of $[\text{Nb}_6\text{O}_{19}]^{8-}$, suggesting that $[\text{Ta}_6\text{O}_{19}]^{8-}$ possesses higher basicity than $[\text{Nb}_6\text{O}_{19}]^{8-}$ and was proven by higher substrate conversion in the CO_2 fixation to styrene oxide. Therefore, $\text{TBA}_6\text{H}_2[\text{Ta}_6\text{O}_{19}]$ (TBA-Ta₆) is expected to hold higher base strength than TBA-Nb₆ and could also be considered as superbases. During this study, TBA-Ta₆ was employed as the catalyst to promote aldol condensation between benzaldehyde and cyclohexanone, whose $\text{p}K_{\text{a}}$ value is 26.4 in dimethyl sulfoxide (DMSO). The result demonstrated higher product yield than TBA-Nb₆, indicating high potential of TBA-Ta₆ to be utilized as superbases catalyst (Figure 6-1). Nonetheless,

systematic and further study of superbase property of TBA-Ta₆ is still required to confirm and identify the highest possible pK_a value.

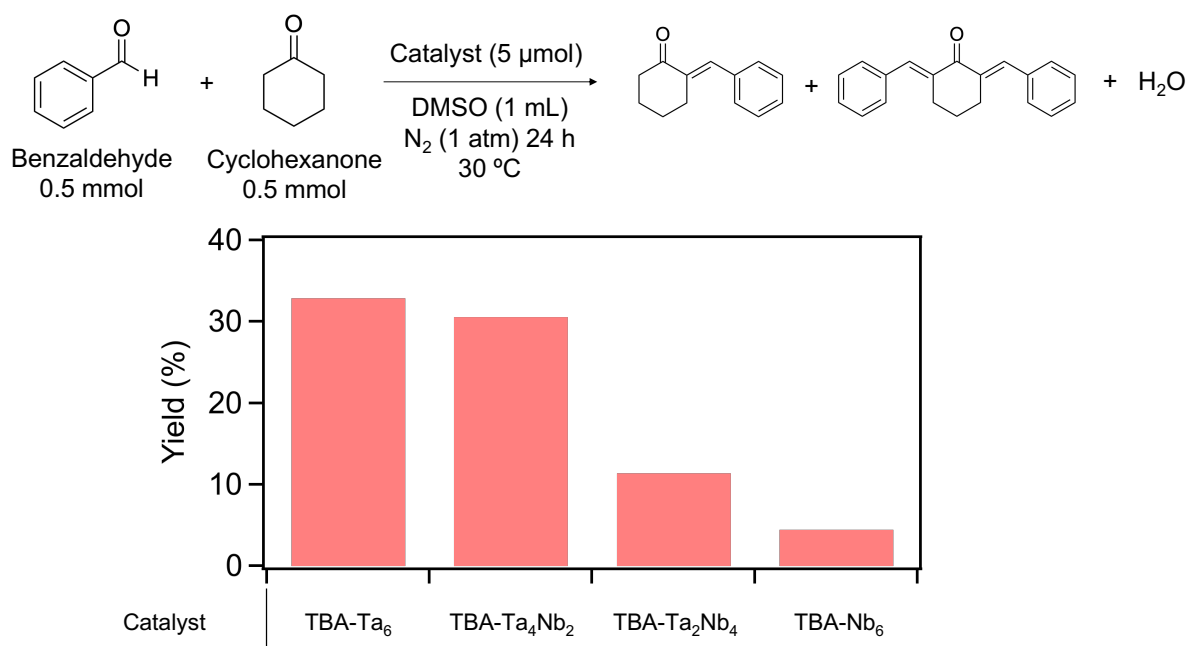


Figure 6-1. Total yield of products from aldol condensation between benzaldehyde and cyclohexanone promoted by TBA-Ta_xNb_{6-x}O₁₉ (TBA-Ta_xNb_{6-x}). Reaction condition: substrates: benzaldehyde, 0.5 mmol; ketone, 0.5 mmol; solvent: DMSO, 1 mL (super dehydrated); atmosphere: N₂ (1 atm); temperature: 30°C; reaction time: 24 h.

The development of multifunctional catalyst has become attractive since the resultant catalyst would provide additional functionality and higher catalytic performance comparing to the pristine materials. The reason could be attributed to the synergistic effect of different active sites when combining into one material. Some of the potential candidates include a series of Ti-incorporated metal oxide clusters where the structures have been reported including [Ti₂Nb₈O₂₈]⁸⁻, [TiNb₉O₂₈]⁷⁻, [Ti₁₂Nb₆O₄₄]¹⁰⁻, [Ti₂Ta₈O₂₈]⁸⁻ and [Ti₁₂Ta₆O₄₄]¹⁰⁻.⁴ The negative charge of the clusters are related to the basicity of surface O atoms.^{5,6} Therefore, it would be interesting to compare the effect of negative charge to basicity of the clusters while keeping the same structure, for instance comparison of catalytic performance between [Ti₂Nb₈O₂₈]⁸⁻ and [TiNb₉O₂₈]⁷⁻ to [Nb₁₀O₂₈]⁶⁻ because all of them have the same decametalate ([M₁₀O₂₈]) structure while Ti-substitution caused the total charge to become difference.

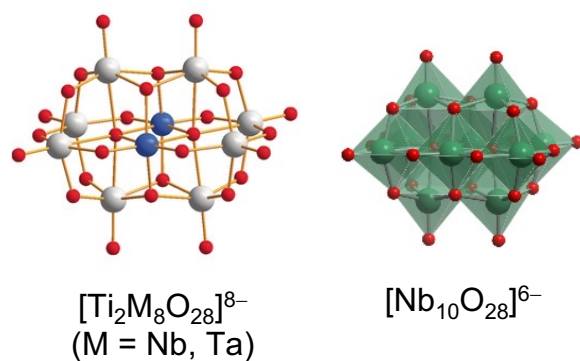


Figure 6-2. $[\text{Ti}_2\text{M}_8\text{O}_{28}]^{8-}$ and $[\text{Nb}_{10}\text{O}_{28}]^{6-}$ exhibit the same decametalate structure with different charges.

Metal oxide clusters could be easily modified by using counter cations. One of the intriguing examples would be N-Benzylcinchoninium chloride (Nni(S)) and N-benzylcinchonidinium chloride (Ndi(R)) as counter cations since these two are enantiomers as depicted in Figure 6-3. The importance of having enantiomeric selectivity in substance produced is because one enantiomer could be beneficial while the other could be harmful.

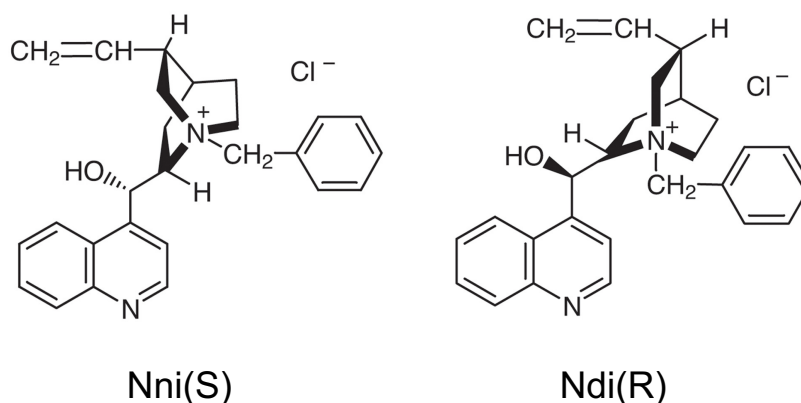
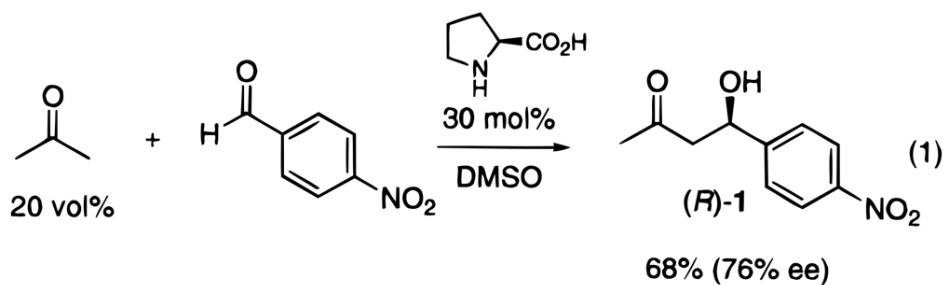


Figure 6-3. Structures of N-benzylcinchoninium chloride (Nni(S)) and N-benzylcinchonidinium chloride (Ndi(R)).

Chiral substance was also found to be useful in catalytic reaction, such as proline which is a proteinogenic amino acid, promoted aldol condensation between benzaldehyde and acetone that resulted in chiral-selective product shown in Scheme 6-2.⁷ This finding suggested stereospecificity of the catalyst could affect the product and potentially control the isomer of the product.



Scheme 6-2. Reaction scheme of proline-promoted aldol condensation reaction.⁷

Currently, chiral compounds are obtained using several organocatalysts to promote the reaction. Slight modification of proline by incorporation of silyl group improved the activity and highly enantiomeric selective products could be obtained. From these results, cation exchange reaction from $\text{TBA}_6\text{H}_2[\text{M}_6\text{O}_{19}]$ to obtain $(\text{Nni})_x\text{H}_{8-x}[\text{M}_6\text{O}_{19}]$ or $(\text{Ndi})_x\text{H}_{8-x}[\text{M}_6\text{O}_{19}]$ ($\text{M} = \text{Nb}$ or Ta) could possibly result in a new type of functional catalyst that exhibit base catalysis and enantiomeric selectivity.

References

- (1) He, J.; Qiang, Q.; Liu, S.; Song, K.; Zhou, X.; Guo, J.; Zhang, B.; Li, C. *Fuel* **2021**, *306*, 121765.
- (2) Zang, H.; Wang, K.; Zhang, M.; Xie, R.; Wang, L.; Chen, E. Y.-X. *Catal. Sci. Technol.* **2018**, *8* (7), 1777–1798.
- (3) Sudarsanam, P.; Li, H.; Sagar, T. V. *ACS Catal.* **2020**, *10* (16), 9555–9584.
- (4) Nyman, M. *Dalton Trans.* **2011**, *40* (32), 8049.
- (5) Sugahara, K.; Kimura, T.; Kamata, K.; Yamaguchi, K.; Mizuno, N. *Chem. Commun.* **2012**, *48* (67), 8422.
- (6) Sugahara, K.; Satake, N.; Kamata, K.; Nakajima, T.; Mizuno, N. *Angew. Chem. Int. Ed.* **2014**, *53* (48), 13248–13252.
- (7) List, B.; Lerner, R. A.; Barbas, C. F. *J. Am. Chem. Soc.* **2000**, *122* (10), 2395–2396.

List of achievements

Publications:

- 1) V. Chudatemiya, S. Kikkawa, J. Hirayama, R. Takahata, T. Teranishi, M. Tamura, S. Yamazoe, *Asian J. Org. Chem.* **2022**, e202200521.
- 2) V. Chudatemiya, M. Tsukada, H. Nagakari, S. Kikkawa, J. Hirayama, N. Nakatani, T. Yamamoto, S. Yamazoe, *Catalysts* **2023**, *13*, 442.
- 3) S. Kikkawa, Y. Fujiki, V. Chudatemiya, H. Nagakari, K. Shibusawa, J. Hirayama, N. Nakatani, S. Yamazoe, *Angewandte Chemie* (Under revision)

Conference presentations:

- 1) “CO₂ fixation using metal oxide cluster catalysts”
V. Chudatemiya, J. Hirayama, S. Kikkawa, S. Yamazoe
 The 127th Catalysis Society of Japan Meeting
 (Online, March, 2021). Poster
- 2) “CO₂ fixation into piperidine using metal oxide cluster catalysts”
V. Chudatemiya, J. Hirayama, S. Kikkawa, S. Yamazoe
 The 19th Annual Meeting of Society of Nano Science and Technology
 (Online, May, 2021). Poster
- 3) “Bifunctional catalysis of metal oxide clusters for N-formylation of amines”
V. Chudatemiya
 The 18th Catalytic Chemistry Workshop
 (Online, September, 2021). Oral
- 4) “N-formylation of amines using metal oxide cluster catalysts”
V. Chudatemiya, S. Kikkawa, J. Hirayama, S. Yamazoe
 The 128th Catalysis Society of Japan Meeting
 (Online, September, 2021). Oral
- 5) “N-formylation of amines using bifunctional metal oxide clusters”
V. Chudatemiya, S. Kikkawa, J. Hirayama, S. Yamazoe
 The 18th Japan-Korea Symposium on Catalysis (18JKSC)
 (Online, November, 2021). Poster (Poster award)
- 6) “N-formylation of amines using metal oxide cluster catalysts”
V. Chudatemiya, S. Kikkawa, J. Hirayama, S. Yamazoe
 Materials Research Meeting 2021 (MRM 2021)

List of achievements

(Yokohama, December, 2021). Poster

- 7) “Hybrid metal oxide clusters and their bifunctional catalysis”

V. Chudatemiya, J. Hirayama, S. Kikkawa, S. Yamazoe

The 2021 International Chemical Congress of Pacific Basin Societies

(Pacifichem 2021)

(Online, December, 2021). Oral

- 8) “Bifunctional catalytic *N*-formylation of amine using CO₂ over metal-oxide-cluster-derived catalyst”

V. Chudatemiya, S. Kikkawa, J. Hirayama, R. Takahata, T. Teranishi, S. Yamazoe

The 9th Tokyo Conference on Advanced Catalytic Science and Technology (TOCAT9)

(Fukuoka, July, 2022). Poster

- 9) “Bifunctional catalytic *N*-formylation of amine of metal-oxide-cluster-derived catalyst using CO₂”

V. Chudatemiya, S. Kikkawa, J. Hirayama, R. Takahata, T. Teranishi, S. Yamazoe

The American Chemical Society Meeting Fall 2022 (ACS Fall 2022)

(Chicago, August, 2022). Oral

- 10) “Tuning product selectivity for base catalytic reactions over Ta-Nb mixed oxide clusters”

V. Chudatemiya, M. Tsukada, S. Kikkawa, S. Yamazoe

The 131st Catalysis Society of Japan Meeting

(Yokohama, March, 2023). Oral

- 11) “Improvement of selectivity in CO₂ fixation reaction to styrene oxide by Ta-substitution for [Nb₆O₁₉]⁸⁻ catalysts”

V. Chudatemiya, M. Tsukada, H. Nagakari, S. Kikkawa, J. Hirayama, N. Nakatani,

T. Yamamoto, S. Yamazoe

The 21st Annual Meeting of the Society of Nano Science and Technology

(Nano 2023)

(Hakodate, May, 2023). Poster

Acknowledgment

During the course of research, I would like to extend my deepest gratitude to Professor Seiji Yamazoe, Dr. Soichi Kikkawa, and Inorganic Chemistry Laboratory members of Graduate School of Science, Tokyo Metropolitan University. Without their constructive comments and kind support, I would not be able to achieve such wonderful results in my study. Their support urged me to keep learning and obtain new findings that keep pushing the limit of my ability.

In addition to laboratory members, I would like to also acknowledge the support from Dr. Ryo Takahata and Professor Toshiharu Teranishi from Kyoto Institute for Chemical Research, Kyoto University for TEM measurement and collaboration in the publication as co-authors. I would like to sincerely thank Professor Masazumi Tamura from Research Center for Artificial Photosynthesis, Osaka Metropolitan University for providing information and fruitful discussion on the reaction mechanism and for collaboration as co-author in the publication.

Moreover, I would not have an opportunity to study in Japan without the financial support from Tokyo Human Resources Fund for City Diplomacy. I also greatly appreciate Professor Boonyarach Kitiyanan from The Petroleum and Petrochemical College, Chulalongkorn University for the information regarding the scholarship opportunity as well as Professor Kotohiro Nomura who provided details of the program and conducted the interviews and provided me an opportunity to study in graduate school in Tokyo Metropolitan University. In addition, I would not have today with the support from my family that could make me feel home away from home.